The effects of water content on mantle circulation, geochemical cycles and surface observables

Kiran Rashmikant Chotalia

A thesis submitted in partial fulfillment

of the requirements for the degree of

Doctor of Philosophy

of

University College London

Department of Earth Sciences

UCL

2020

I, Kiran Rashmikant Chotalia, confirm that the work presented in this thesis is my own. Where information has been derived from other sources, I confirm that this has been indicated in the thesis.

Abstract

Water is one of the key components for life and yet its role in Earth evolution is not well understood and its interaction with the mantle even less so. There is evidence of mantle water from mid-ocean ridge basalts, ocean island basalts and diamond inclusions that indicate local hydration. However, how much water resides in the mantle today is completely unknown. I use a parametrised mantle convection model to understand the interaction of the surface ocean and mantle reservoir by tracking degassing of water to the surface and regassing of the mantle at subduction zones. This thesis aims to examine the effects of viscosity laws and mixing on thermal evolution and the water cycle. I also use present and past surface exposure of topography to constrain the behaviour of the water cycle and assess how much water the mantle resides in the mantle today.

I show that a temperature-dependent viscosity law best matches present day average mantle temperature compared to water-dependent laws that promote excessive cooling. With this viscosity law, I take into account a mixing time in the water cycle where it takes a finite amount of time for subducted water to be degassed at a mid-ocean ridge. Results show that mixing effectively traps water at depth forming a more hydrous mantle and a smaller surface ocean. This delay also induces a period of net degassing and the associate fluctuations in the water cycle translate to changes in sea level $>10\,\mathrm{m}$. Finally, I calculate the relationship between surface ocean mass and sea level, using the Earth's hypsometry. I use present and past surface exposure and present day estimates for the degassing flux to show that no more than 1 ocean of water can reside in the mantle today.

Impact Statement

Water is fundamental to habitability and life. Life could not have begun or been sustained without this precious resource. Understanding its role in planetary evolution is key and hence this thesis I have investigated the deep water cycle, the outcomes of which are of direct interest to Earth and planetary science communities and the general public.

The importance of water and other volatiles have already been realised with the support of the Deep Volatiles consortium (NERC) and the results presented here will propel further research into this area. Geodynamic models such as those presented here are an ideal tool to foster collaboration within Earth sciences and can be extended to planetary sciences. Multi-disciplinary studies, particularly those involving geochemistry and studies of geochemical heterogeneity in the interior, are an ideal extension and avenue for further development. Collaborations with geologists and palaeobiologists are a natural area of further research particularly concerning changes in sea level over Earth history. Further collaborations with planetary scientists could also help in understanding the differences in how planets evolve.

Public engagement and interaction is essential in order to spark interest in the Earth and sustaining and developing work presented here. The scientific discussions of this thesis have been communicated through outreach events within UCL and as part of the GeoBus initiative that brings Earth sciences learning directly to schools, inspiring children to take up STEM subjects in their futures.

Finally, as one of our most precious resources, an understanding of the deep water cycle is imperative as our sights are set to travel within the solar system and beyond.

Contents

List of Figures

List of Tables

Glossary of Terms

D	Degassing: removal of water from the mantle via melting Net Degassing: net transport of water to the surface reservoir where $D > R$
H	Radiogenic Heating: heat produced by the decay of radioactive elements U^{238}, U^{235}, Th and K Heating: net thermal state of the mantle where $H > Q_s$
Q_s	Surface Heat Flow: heat removed from the mantle at MORs Cooling: net thermal state of the mantle where $H < Q_s$
R	Regassing: introduction of water to the mantle at subduction zones Net Regassing: net transport of water to the mantle where $D < R$
MOR	Mid-ocean ridge
τ	Constant Mixing Time: transport of water from a subduction zone to a MOR occurs over a fixed length of time. For a variable mixing time, τ refers to the mixing time prior to scaling with the Rayleigh number, Ra
τ_{Ra}	Variable Mixing Time: transport of water from a subduction zone to a MOR occurs over a variable length of time determined by the Rayleigh number

Acknowledgments

Firstly, a massive thank you to my supervisors Carolina and John whose enthusiasm, encouragement and support throughout both my masters and this thesis have been unwavering. Your drive to find truly new and innovative things are utterly contagious and will be something I never forget.

Neil, Keely and Fabio - thank you for listening and helping since the start of my research. Your willingness to answer mountains of questions showed me what a great research group can and should be. In particular, thank you Neil - your patience and advice in finding the best way to communicate science have been invaluable.

I was lucky enough to make two amazing friends during all this, and sharing the experience has been essential. Isra - resident answerer of all things rock related, post-conference holiday buddy and all round superhero. I am so glad you became my desk mate to distract on a daily basis. Antoniette - my geodynamics touchstone, conference companion and tea guru. We made our litany of meetings and five months in the US into such adventures. Thank you both for chatting science, avoiding science and everything in between.

Rosie and Anna - I'm so glad I managed to drag you both to the Big Smoke! Catching up over dinner and impromptu theatre trips helped to keep me sane in this crazy process.

Mum, Dad and Meera - this body of work is the product of all your love and support throughout school, college and eight years at university. You've instilled in me a love of science and a work ethic without which, none of this would have been possible. Masi and Kaka - thank you for always lifting my mood, if not in person always at the other end of the phone.

Finally, to my grandparents, Baa and Dada, Baa and Bapuji. This is for you.

1 Introduction

1.1 The Deep Water Cycle

On geological time scales, the Earth's mantle convects transporting heat from the interior to space. Convection of the mantle interior manifests at the surface as plate tectonics where rigid lithospheric 'plates' move across the Earth surface, on the order of centimetres per year. Divergence of these plates form mid-ocean ridges (MORs), where decompressing mantle material melts forming a chemically heterogenous lithosphere of basaltic crust and harzburgitic mantle residuum. This package cools, becoming dense until it meets another plate in a convergent setting. Due to its negative buoyancy, the denser of the plates is subducted returning this slab back into the mantle. This transport between the surface and interior acts to cool the mantle and also transport volatiles such as water between the two reservoirs. Water is partitioned and released to the surface during melting at MORs whilst water is returned to the mantle due to the subduction of sediments, serpentinised oceanic crust and lithospheric mantle. These transports together with the surface and mantle interior reservoirs form the deep water cycle (Figure 1.1).

The deep water cycle is of particular interest as not only does it expand understanding for one of the key components of life, but also for its potential feedback to thermal and hence planetary evolution. The thermal history of a planet is dictated by the mineral properties throughout its interior. These mineral properties vary less than an order of magnitude over pressure and temperature conditions for the Earth's silicate mantle, with the exception of viscosity. Viscosity defines resistance to flow such that high viscosity limits flow making convection sluggish whereas low viscosity increases convective vigour. This has implications for how the mantle cools where higher viscosity is associated with slower cooling and lower viscosity can induce rapid cooling. Due to the temperature dependence of viscosity, a feedback is created in the thermal evolution where viscosity is a ther-

mostat, regulating mantle temperature (Schubert et al., 1979). Variation in heat transport also affects the transport of water between the surface and interior and an additional feedback is introduced due to the effect of water on viscosity. There is still uncertainty surrounding the sensitivity of water content on mantle mineral viscosity, but the potential for water to reduce viscosity up to three orders of magnitude (Mei and Kohlstedt, 2000a; Fei et al., 2013) would have considerable feedback on the thermal evolution and deep water cycle.

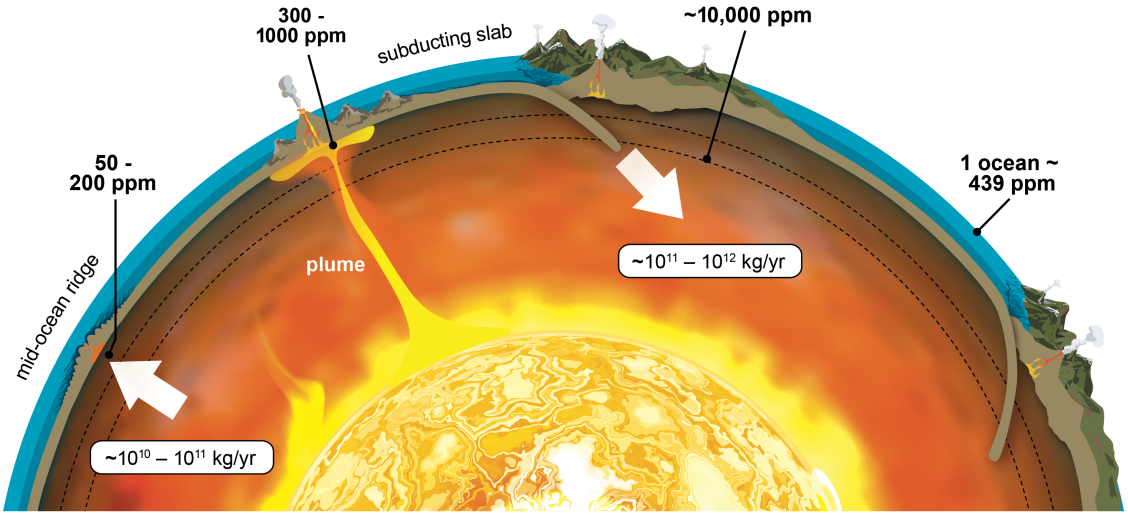

Figure 1.1: Cross-section of Earth showing the deep water cycle at the present day, outlining how much water is transported in and out of the mantle (Section 1.5), the water content of samples and approximate depths they are thought to represent (Section 1.4).

Constraining the amount of water in the mantle is also vital to understanding the extent of this feedback. If there is no water in the mantle, the evolution would be controlled by temperature alone whereas high mantle water contents coupled with a high sensitivity in viscosity may have a considerable effect on evolution. Current estimates from geochemistry range from less than 1 to 15 oceans (Hirschmann, 2006; Marty, 2012a). Samples from MOR basalts (MORBs) and ocean island basalts (OIBs) point toward heterogeneity in mantle water content (Hirschmann and Kohlstedt, 2012). MORBs are thought to represent the portion of the mantle that has undergone repeated stages of melting whereas geochemical data from OIB noble gases such as ${}^{3}He/{}_{4}He$ and ${}^{40}Ar$ points toward reservoirs that have remained isolated (Gonnermann and Mukhopadhyay, 2009; Parai and Mukhopadhyay, 2018). However, the portion of the mantle these samples represent is unclear. The potential for isolated reservoirs also indicate processing of mantle material takes on the order of billions of years. A long residence time

also implies there is a delay in exchanging material from the interior to the surface. This effect would not be isolated to noble gases but also extend to water in the mantle with further consequences for evolution due to the feedback imposed by the water-dependence of viscosity. Variations in water cycle also inevitably have consequences for the Earth's surface. Changes in the ocean volume will cause changes in sea level and these changes in particular are important when considering the impacts on geological record, processes and life.

Examining and understanding these feedbacks in the water cycle and their effect on thermal evolution is key to understanding why differences in planetary evolution and habitability occur. This body of work focuses on the complex, interconnected nature of the water cycle and the thermal evolution on Earth.

1.2 Mantle Composition

Water exists in the mantle in two main ways: as hydrous mineral phases or incorporated into the crystal lattice of nominally anhydrous minerals (NAMs). Hydrous mineral phases easily accommodate water in their mineral structure whilst NAMs incorporate water as H^+ defects accommodated in the mineral structure as the hydroxyl, OH^-. How much water is in the mantle depends on mantle composition, the resulting water capacity of this phase assemblage and how much water is transported between the mantle and surface ocean.

The phase assemblage of the upper mantle is well-known; direct samples from mantle xenoliths and obducted oceanic crust in collision zones exhibit a basaltic crust and harzburgite residue due to the partial, decompression melting at MORs. This leads to the theoretical composition of the upper mantle, pyrolite (Ringwood, 1962), a solid solution containing ∼60 % olivine, ∼20 % pyroxene and ∼20 % garnet. This surface composition can then be used to explore the effects of high pressure and high temperature within the mantle indicating the phases present at these conditions (Figure 1.2). Ideally, direct samples from these regions would confirm the theory but the inaccessible, high pressure-high temperature environment of planetary interiors prevents direct sampling. Samples can be brought to the surface as xenoliths or mineral inclusions but there are few, with the deepest sample as a diamond inclusion from the transition zone (e.g. Pearson et al., 2014), not even reaching mid-mantle depths.

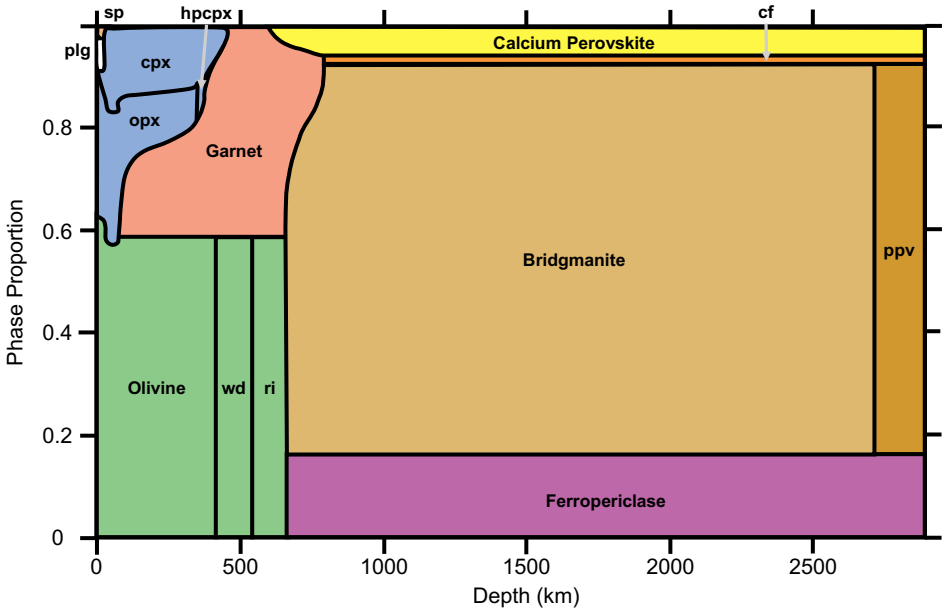

Figure 1.2: Phase diagram of a pyrolitic mantle adapted from Stixrude and Lithgow-Bertelloni (2012) where sp = spinel, plg=plagioclase, cps=clinopyroxene, opx=orthopyroxene, hpcpx=high pressure cpx, wd=wadsleyite, ri=ringwoodite, cf=calcium ferrite structured oxide and ppv=post-perovskite.

1.3 Mantle Water Capacity

The mantle water capacity is dependent on the minerals present. Olivine, pyroxenes and their high pressure polymorphs make up almost all of the silicate Earth with the olivine component most extensively studied. Olivine can contain up to ∼4000 parts per million by weight (here after ppm) near the 440 km-discontinuity (Bell et al., 2003). Pyroxenes may be able to accommodate almost double the olivine capacity and garnet up to 750 ppm (Nestola and Smyth, 2015).

The transition zone is well known for bearing the minerals with the highest capacity for water. Low temperature (∼1273 K) wadsleyite and ringwoodite could contain up to 33 000 ppm at 15 GPa and 22 000 ppm at 20 GPa respectively (Kohlstedt et al., 1996; Ohtani, 2005). Coupled with garnet, this suggests that the transition zone alone may hold up to 10 000 ppm of water (Ohtani, 2005), equivalent to 3 oceans. Higher temperature (∼1873 K) and pressure experiments show a reduced capacity ∼3000 ppm at 18 GPa and ∼5000 ppm at 20 GPa respectively (Litasov and Ohtani, 2003; Ohtani et al., 2000). These experiments are more representative of ambient mantle conditions suggesting that the trans-

ition zone may only hold up to 1.4 oceans. Dense hydrous magnesium silicate (DHMS) phases have also been shown to be stable at conditions associated with subducting slabs, potentially storing up to 180 000 ppm (Ohtani, 2005). Their volumetric contribution to the mantle is relatively small in comparison to the constituent minerals, and are only stable under certain conditions. DHMSs could be considered a transient store due to the changing nature of subduction throughout Earth's history (e.g. van Hunen and Moyen, 2012).

Perovskite forms ∼80 % of the lower mantle and 60 % of the whole mantle, therefore its properties will have a large impact on overall mantle dynamics. Experiments exhibit a large range of values for capacity; a number of studies show evidence for both a low and high capacity lower mantle at ambient conditions. For example, Bolfan-Casanova et al. (2000) show dry perovskite is unable to accommodate hydroxyl ions whilst Litasov and Ohtani (2003) show the capacity of perovskite may reach ∼2000 ppm. Ohtani (2005) present a collection of experimental data that shows pure Mg-perovskite has the lowest capacity <110 ppm (<0.17 oceans in the lower mantle), Mg-Al-perovskite can hold up to 1500 ppm and Mg-Al-Fe-perovskite can hold up to 4000 ppm. While the collection is not comprehensive, it could highlight how possible differences in composition can change the capacity, making a case for locally hydrous regions in the lower mantle. Ferropericlase (Mg,Fe)O and Ca-perovskite make up the majority of the remaining 20 % of the lower mantle and also show discrepancies in capacity with Bolfan-Casanova et al. (2000) reporting a dry periclase whilst Murakami et al. (2002) show a capacity up to 2000 ppm. A similar debate also occurs on the computational side of the argument: Panero et al. (2015) argue for a dry lower mantle from experimental, thermodynamic and first principles calculations suggest an overall lower mantle capacity no greater than 200 ppm. In comparison, first principles calculations by Hernández et al. (2013) propose a lower mantle capacity ∼1000 ppm (∼1.5 oceans in the lower mantle). Perovskite's high pressure polymorph post-perovskite has also been considered a potential sink for primordial and recycled hydrogen (Townsend et al., 2015).

With an upper mantle capacity of 4000 ppm, a transition zone capacity of 3000 ppm and a lower mantle capacity of 1000 ppm the maximum whole mantle capacity is approximately 4 oceans. For a lower mantle capacity of 100 ppm, the whole mantle capacity reduces to ∼3 oceans. However, as shown above, these are rough estimates.

1.4 Mantle Water Content

These high storage capabilities are not reflected in the natural samples from the upper mantle (Figure 1.1): MORBs contain 50 ppm to 200 ppm whilst ocean island basalts (OIBs) contain ∼300 ppm to 1000 ppm, implying heterogeneity throughout the mantle (Hirschmann, 2006).

There is evidence of a hydrous transition zone in a ringwoodite inclusion of a diamond. Using x-ray diffraction, Raman and IR spectroscopy (Pearson et al., 2014) identified ringwoodite with ∼14 000 ppm water from alluvial deposits in Brazil. This sample remains the only direct evidence for terrestrial ringwoodite and a hydrous transition zone, at the very least locally. Tschauner et al. (2018) have more recently identified the existence of ice-VII in diamond inclusions, indicating the existence of water with the transition zone and around the boundary with the lower mantle.

Fei et al. (2017) present the temperature- and water-dependence of dislocation mobility in ringwoodite. By comparing viscosities with anhydrous bridgmanite, they argue for a globally hydrous transition zone in order to match postglacial rebound estimates that required the transition zone viscosity to increase by an order of magnitude at the boundary with the lower mantle. Partition coefficient experiments suggest that water is preferentially partitioned into the transition zone (Bolfan-Casanova et al., 2000), also supporting the case for a hydrous transition zone.

Seismological efforts to understand mantle water content paints a contrasting picture. Wang et al. (2019) argue for a transition zone with hydrous pockets. They examine a high resolution image from receiver functions of the transition zone under the United States with the dataset from the entire USArray. Pervasive negative seismic anomalies less than 100km in the vertical direction are consistent with the signature of olivine-rich harzburgite containing ∼10 000 ppm of water. They suggest that water is brought into the region via super hydrous phases. Similarly, shear wave tomography indicates that the transition zone is only locally hydrated around subduction zones (Houser, 2016). Examination of the elastic moduli of hydrous ringwoodite suggest that combined with temperature effects, the transition zone contains water on the order of ∼1000 ppm (Mao et al., 2012). On the other hand, seismic wave speeds alone have been shown not to detect water contents, as even with almost saturated samples temperature effects easily overprint almost saturated hydrous signatures. Using the impedance contrast in

the future may yield more accurate results (Buchen et al., 2018).

This building evidence is supporting the idea of a heterogeneously hydrated upper mantle. Thus far, partitioning experiments (e.g. Bolfan-Casanova et al., 2000) suggest that the lower mantle is dry, containing a non-detectable amount of water. Evidence for the lower mantle is still restricted due to the complex nature of experiments (laboratory and computational) and the unlikely possibility of recovery of minerals stable at these conditions.

To estimate the total water content of the mantle, we can use these estimates as upper and lower bounds for the whole mantle average water content. From MORBs, a mantle hydrated throughout with 50 ppm would contain 0.1 oceans whilst an 1000 ppm mantle from OIB data would contain 2.3 oceans, approximately half the capacity calculated in the previous section. This suggests that the mantle on the whole, is not at capacity.

These estimates are based on present day conditions. Estimates can also be drawn from the other end of the spectrum. Earth, as the other planets, was built from planetesimals containing water. Chondritic meteorites representative of these building blocks suggest a range of bulk water content for the silicate Earth and surface is ∼5 oceans to 15 oceans (Marty, 2012b). Approximately one of these oceans accounts for the atmosphere, oceans, sediments and crust leaving the bulk mantle with ∼4 oceans to 14 oceans.

1.5 Transport Fluxes

In order to understand how the mantle water content has changed over time, the transport processes between the surface and mantle interior must be understood. Water enters the surface reservoir from the mantle at MORs in a process called degassing and is return to the mantle via subduction zones in regassing (Figure 1.1).

1.5.1 Degassing

Melting at MORs accounts for 90 % of global magmatism today, degassing the mantle reservoir. The melting is partial and produces a basaltic crust underlain by residual harzburgitic mantle. Basalt production is estimated to be between 20 km^3/yr (Cogné and Humler, 2004; Marty, 2012b) and 49 km^3/yr (Smyth and

Jacobsen, 2013). During this, all of the water is partitioned from the solid mantle into the melt (e.g. Asimow et al., 2004). If 12 % partial melt (Marty, 2012b) and 50 ppm to 200 ppm (Hirschmann, 2006) are assumed of the MORB source, mantle degassing is on the order 10^{10} kg/yr to 10^{11} kg/yr.

However, the degassing efficiency is suggested to be anywhere from 0.1 % to 100 % where MORBs can either hold onto all of their water (0.1 %) or lose all their water (100 %). Sub-aerial volcanism removes all the water from the melt, effectively drying the source (Rüpke et al., 2013) but this is suppressed when volcanism is submarine, for water depths >100 m (Dixon and Stolper, 1995). Dixon and Stolper (1995) show that by examining MORB glasses and forward modelling magma ascent in the presence of water and carbon, degassing efficiency is <10 %. In water rich environments such as for arcs, previous parametrised models often assume 100 % degassing efficiency (McGovern and Schubert, 1989; Franck and Bounama, 2001; Crowley et al., 2011) but when it is actively searched for in the parameter space (along with regassing efficiency, see Section 1.5.2) values are from 0.1 % to 1 %.

1.5.2 Regassing

	Sediment	Upper Crust	Lower Crust	Wet Mantle	Dry Mantle
ρ_n (kg/yr)	2200[1]	2800[1]	2800[1]	2900[2]	3300[1]
d_n (m)	300	1000	6000	10000	85000
X_n (ppm)	70000	30000	10000	13000	0

Table 1.1: Representative wet layers in a subducting package ∼100 km based on Faccenda (2014), [1]Schubert et al. (2001) and [2]Hilairet and Reynard (2009).

Slabs are known to penetrate into the deep mantle, evident in seismic tomography (e.g Goes et al., 2017, and references therein). The regassing flux is defined by the subducting package that brings water into the subduction zone in sediments, hydrated basaltic crust and serpentinised mantle (Table 1.1), confined to the top ∼17 km of a ∼100 km subducting lithosphere. Estimates range from 10^{11} kg/yr to 3×10^{12} kg/yr (Faccenda, 2014) but how much water makes it into the mantle and becomes a part of the deep water cycle is unclear. In the top portion of the slab, hydrous phases such as lawsonite and serpentinite become unstable when the slab warms as it comes into contact with hot mantle wedge at depths <200 km. These

dehydration reactions release water into the mantle wedge, feeding arc volcanism on the surface (e.g. Rupke et al., 2004). The regassing efficiency can therefore be defined as the fraction of water that makes it past the arc front dehydration reactions. Estimates of the regassing efficiency from petrological work (van Keken et al., 2011), geodynamic models (Schmidt and Poli, 1998; Rupke et al., 2004; Korenaga, 2011; Magni et al., 2014; Nakao et al., 2016) and seismic studies (e.g. Faccenda, 2014) indicate this fraction can be anywhere from several percent up to 40 %. Rupke et al. (2004) couple a geodynamic model of subduction to slab petrology using PERPLEX and find that up to 40 % of an older slab's water can be retained. Similarly, van Keken et al. (2011) use two-dimensional (2D) subduction models tracking metamorphic facies and water content for a variety of slabs at different temperatures. They conclude that 32 % of water in the subducting package makes it past the dehydration process resulting in a return flux to the mantle at present of 3.2×10^{11} kg/yr.

Of the water in the initial subducting package transported deeper than 250 km, hydrous phases such as phase A may be key to subducting water into the transition zone and upper most lower mantle (Nakao et al., 2016; Yang et al., 2018; Nakagawa and Nakakuki, 2019) potentially retaining ∼2000 ppm. Regardless of the range of estimates for both the water input to the subduction zone and for the regassing efficiency, estimates for the amount of water that make it past the arc front are $\sim 10^{11}$ kg/ yr to 10^{12} kg/ yr. However, this is only applicable for Earth today. Higher mantle temperatures in the past would result in dehydration reactions occurring at shallower depths, decreasing the mass of water transported to the deep mantle. Magni et al. (2014) estimate a regassing efficiency of 3 % to 13 % in the Archean and van Keken et al. (2011) estimate the average efficiency over 4.6 Gyrs to be ∼9 %. Sandu et al. (2011) is one of the few parametrised studies where efficiencies are not assumed, but the parameter space is searched for regassing efficiency and solutions are constrained for the present day Earth. In this case, regassing efficiencies are found to lie between 0.1 % to 1 %, perhaps more like the average regassing efficiency of van Keken et al. (2011).

Together with degassing estimates, the net change in ocean mass today is equivalent to the difference between degassing and regassing, equivalent to 2.9×10^{11} kg/ yr to 10^{12} kg/ yr net movement of water into the mantle, defined as net regassing.

1.6 Water and Deformation

The transfer of water is controlled by how easily the mantle deforms and flows, varying how fast plates are subducted and diverge at MORs. Deformation is quantified by the relationship between the stress applied and the resultant strain rate. A material's resistance to the applied stress is defined as the viscosity η and it's this ratio of stress σ to strain rate $\dot{\epsilon}$ that describes how easily a material flows:

$$\eta = \frac{\sigma}{\dot{\epsilon}}$$

where stress and strain rate are related as

$$\dot{\epsilon} = A(T, C, G, ...)\sigma^n$$

with A dependent on numerous material properties such as temperature T, composition C and grain size G. Deformation via diffusion creep can be modelled where $n = 1$ and stress is linearly proportional to strain rate; this is also the definition of Newtonian viscosity and remains a constant with variation in stress and strain rate. However, for dislocation creep, the stress-strain rate relationship is extremely non-linear where n varies between 2 and 5. This non-linearity results in a stress-dependent, effective viscosity that changes with stress and strain rate. Nevertheless, effective viscosity is a useful tool in understanding how the mantle deforms and flows.

The incorporation of water (OH^-) into the crystal lattice encourages deformation that weakens the material. To what extent this 'hydrolytic weakening' occurs in mantle minerals under high pressure and high temperature conditions is an area of active research. Most studies have concentrated efforts on olivine which contributes most to the overall upper mantle rheology, and whose high pressure polymorphs constitute the majority of the mantle.

Experiments on single crystal olivine (Fei et al., 2013) show approximately one order of magnitude change in viscosity whereas polycrystalline data exhibits up to three orders of magnitude variation (Karato et al., 1986; Mei and Kohlstedt, 2000a; Jung and Karato, 2001). Numerical experiments on lower mantle minerals have shown that the effect of water on their viscosity may be negligible for water contents of $\sim$100 ppm (Muir and Brodholt, 2018). The effects are only seen when

the water content is 1000 ppm in the deepest parts of the lower mantle coupled with grain sizes smaller than 0.1 mm. However, this study does not take into account the possible effects of water along grain boundaries. The discrepancies between single crystal and polycrystalline data requires further investigation.

This disparity in the few hydrous experiments published is also reflected in anhydrous experiments. It is important to note that more experiments need to be carried out on the constituent mantle minerals at representative pressures and temperatures to fully comprehend deformation effects of water (Karato, 2010). However, initial constraints of mantle flows laws from these studies gives a starting point to investigate the effects of water on viscosity and in turn the effect of a water-dependent viscosity on mantle dynamics.

1.7 Convection Models

1.7.1 Dimensional Models of the Water Cycle

Two-dimensional (2D), spherical annulus models of the water cycle have shown an increase in plate motions when considering a water-dependent viscosity (Nakagawa et al., 2015). Higher velocities cause more cooling and higher viscosities are reached in the lower mantle when the viscosity law is more sensitive to water content. Further work has shown that the mantle water capacity may have a large impact on how much water resides in the mantle (Nakagawa, 2017), with the most recent models suggesting that up to 10 oceans could be subducted into the mantle (Nakagawa and Nakakuki, 2019).

In contrast, three-dimensional (3D) models show that for representative mantle temperatures and realistic plate velocities, between 1 and 2 oceans are expected for the mantle water content today (Price et al., 2019). Water capacity is also expected to change a relatively small amount based on simplified water capacity tables (Iwamori, 2004).

Price et al. (2019) also suggest that these discrepancies cannot be fully explored in 3D (and 2D) due to the high computational resources required and in their place, parametrised models can be used. These simplified models can capture behaviour representative of the physics governing the system by solving only for how average mantle temperature and average mantle water content vary with time, allowing greater exploration of the parameter space.

1.7.2 Parametrised Models

1.7.2.1 Thermal Evolution

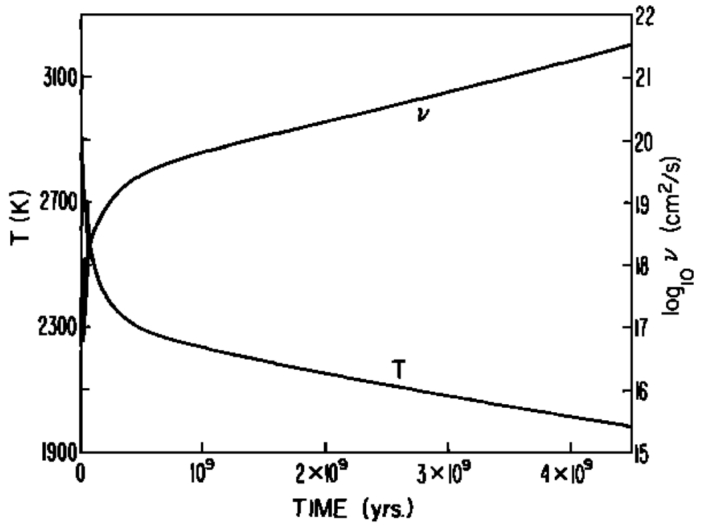

Figure 1.3: Evolution of average mantle temperature and viscosity solved for by a parametrised convection model (Schubert et al., 1980).

The first approach that considered a convecting mantle was proposed by Turcotte and Oxburgh (1967). They examine a singular convection cell with a viscous core solving analytically for the flow along the vertical and horizontal boundaries. From this analysis, they were able to match velocities associated with continental drift and match heat flux estimates from the oceanic crust. For further study, one of the most interesting outcomes was the derivation of the relationship between the convective velocity along the horizontal boundaries of the cell, u and Rayleigh number, Ra

$$u = 0.142 Ra^{\frac{2}{3}} \tag{1.1}$$

Ra is a ratio of diffusive to advective timescales, indicating whether viscous or buoyant forces dominate. This relation can tie together the convection of the interior with the movement seen at the surface. As such, if the material properties of the mantle are known, Ra can be calculated and estimates made for the 'plate velocity'. This surface movement can be used to calculate the heat lost at mid-ocean ridges and together with the (radiogenic) heat input, a simple conservation equation can be constructed of the form

$$\frac{dT}{dt} = \frac{H - Q_s}{c_p} \tag{1.2}$$

where the change in average mantle temperature T with time t is dependent on the difference between the heat provided to the mantle from radiogenic heating H and the heat taken away via surface heat flow Q_s. The dependence of Q_s on plate velocity and hence Ra also makes Q_s dependent on mantle viscosity Viscosity is not only a function of temperature and pressure, it also depends on composition of the mantle C, water content X (and other volatiles) and grain size G, among others:

$$\eta = A\left(C, X, G, etc.\right) exp\left(\frac{E + PV}{RT}\right) \tag{1.3}$$

Early parametrised convection studies show a temperature-dependent viscosity impedes convection, regulating the release of heat from the interior to the surface (Figure 1.3). Earlier in Earth history when mantle temperatures were high, viscosity was relatively low, convection vigorous and surface heat flow high. The release of heat decreases temperature and increases the viscosity, reducing the vigour of convection and surface heat flow (Sharpe and Peltier, 1978; Schubert et al., 1980; Christensen, 1985). This relatively simple view of the effect of a temperature-dependent viscosity on convection highlights this feedback controlling planetary cooling. The relation continues to be extended further to investigate grain size dependent viscosities (Solomatov, 2001), and most recently the effects of a water-dependent viscosity (Crowley et al., 2011; Sandu et al., 2011; Korenaga, 2011; Höning and Spohn, 2016; Komacek and Abbot, 2016).

1.7.2.2 Coupled Thermal Evolution and the Deep Water Cycle

With water weakening evident in olivine (e.g. Chopra and Paterson, 1984), inclusion of water in parametrised model viscosity laws could be used to assess the effects of a water-dependent viscosity on thermal evolution. Initial inclusion manifested as time-varying activation temperature and the assumption that the mantle had been in a continuous state of degassing since its formation (Jackson and Pollack, 1987). McGovern and Schubert (1989) included the effects through a water-dependent activation enthalpy derived from experimental work of Chopra

and Paterson (1984) and showed overall degassing increases mantle temperatures and regassing results in a decrease, for the present day.

Williams and Pan (1992) and Franck and Bounama (1995) solve for the thermal evolution and water cycle simultaneously linked by a water-dependent viscosity from experimental work of Karato and Wu (1993). These models were the first to self consistently determine whether the mantle was in a state of degassing or regassing and continue in this way to the present day. These models solve for the conservation of mass $^{dX}/_{dt}$

$$\frac{dX}{dt} = R - D \tag{1.4}$$

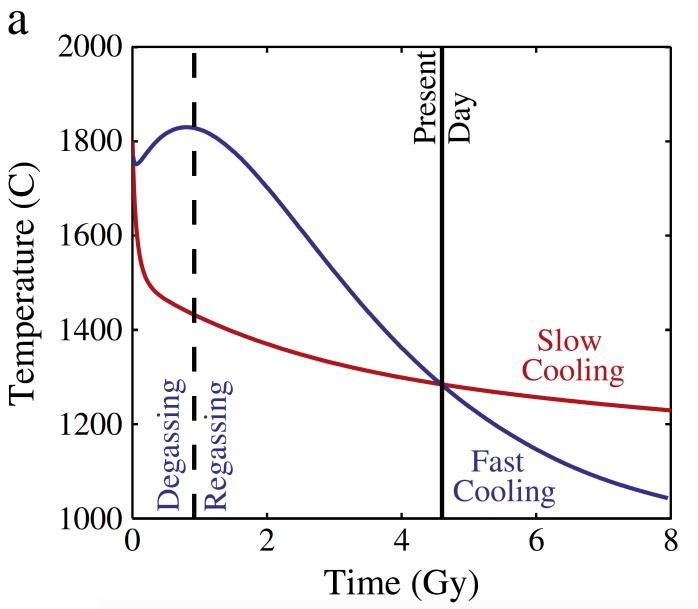

Figure 1.4: Temperature evolution from Crowley et al. (2011) where viscosity is either water-independent (red) or water-dependent (blue).

where the difference between mantle regassing at subduction zones, R, and degassing at MORs, D, shows whether mantle water content is increasing or decreasing. Crowley et al. (2011) and Sandu et al. (2011) both include viscosity laws dependent on water and temperature linking the thermal evolution and water cycle. Older models show thermal evolution beginning with a period of cooling adjustment before heat decays at a rate proportional to radiogenic heating. While both Crowley et al. (2011) and Sandu et al. (2011) models show a period of heating before they cool (e.g. Figure 1.4) during the adjustment, the hydrous mantle degasses; the release of water to the surface increases the viscosity to the extent

that convection is inefficient and heat builds up in the mantle. The heating acts to reduce viscosity and cooling controlled by radiogenic decay occurs. Korenaga (2011) defined a viscosity contrast between the mantle and lithosphere that considers the effects of melting and water content. By including the evolution of the upper boundary layer in the model, the author also defines stagnant and mobile lid tectonic regimes, linking the persistence of plate tectonics throughout Earth's history with the early dehydration of mantle. These three studies highlight the importance of including a linked water and thermal feedbacks and how the thermostat effect changes when a water dependent rheology is introduced; most recently, these models have been extended to include continental generation stabilised by the biosphere (Höning and Spohn, 2016) and how a water and temperature dependent rheology affects the evolution of Super Earth waterworlds (Schaefer and Sasselov, 2015; Komacek and Abbot, 2016).

1.8 Implications for Thermal and Chemical Evolution

Changes in viscosity also have implications for the preservation of geochemical reservoirs (Manga, 1996) such as ${}^{3He}/_{4He}$ and ${}^{40}Ar$. These differences can be seen in the geochemical zoo identifying different sources regions in the mantle. The mantle is expected to be relatively degassed and low geochemical signatures are seen in MORBs. However, OIBs present high signatures in their source region, implying the lower mantle may be relatively undegassed. The high viscosity lower mantle (Hager et al., 1985; Rudolph et al., 2015) is invoked as a potential reason for these differences; higher viscosity implies that flow is relatively slow in the lower mantle and the lower viscosity upper mantle flows relatively fast. This can be qualitatively assessed in a few different ways. The mixing time is the period it takes for a heterogeneity (i.e. subducted slab) to be stretched to the sub-metre scale, where homogenisation is dominated by diffusion. Estimates range from $<$1 Gyrs to 10 Gyrs, reflecting the range of assumptions used in these estimates. However, when similar assumptions are made about the diffusive length scale and flow velocity, this range narrows between 3 Gyrs and 4 Gyrs. Another measure is the residence time. This is equivalent to the period of isolation a reservoir experiences, often until it is sampled by melting. Estimates can be similar to the mixing time $\sim$3 Gyrs to 10 Gyrs (Tackley, 2015).

Upper mantle material with a relatively low viscosity is processed quickly at MORs which is equivalent to a short residence time whereas high viscosities of the lower mantle and associated low flow velocities imply a long residence time (Gurnis and Davies, 1986). Changes in viscosity and the associated flow velocity also have implications for how long heterogeneities survive in the mantle. As with residence time, higher viscosities invoke longer mixing times and longer survival of isolated reservoirs.

With respect to water, higher concentrations are found in OIBs samples compared with MORBs (Section 1.4). These differences are also likely to be the result of the viscosity structure of the mantle. The overall impact of a delay in transport of water across the mantle is particularly interesting due to the potential feedback to the thermal evolution and has not yet been investigated with respect to heterogeneity.

1.9 Further Possible Constraints on Water?

It is clear that water has a crucial role to play in our understanding of Earth's evolution. Information can be inferred from geological samples for the present day but due to the volatile nature of water, understanding its role in Earth's evolution is a task best tackled with convection models.

The majority of geodynamic studies investigating the deep water cycle have used parametrised models. By their nature, they assume any subducted material (including water) is instantaneously and homogeneously mixed into the mantle. In reality, due to the geological timescales of convection, it takes time for this mixing to occur. This phenomena is evident in geochemical data and implicit in 2D and 3D convection models (Tackley, 2015).

Some of the most useful tracers of heterogeneity are isotopes such as $^{3}He/^{4}He$ and ^{40}Ar. By measuring their abundances and combined with their fractionation and decay behaviour, present day mixing times from geochemical constraints vary from $\sim$0.5 Gyrs to 4 Gyrs (Gonnermann and Mukhopadhyay, 2009; Tackley, 2015), potentially explaining the survival of enriched reservoirs feeding OIBs. Estimates from geodynamic models suggests mixing times up to 1 Gyrs for the present, however when extrapolating these results over Earth history, tectonic regime must be considered. For early Earth, Hadean mixing times on the 0.1 Gyrs scale are predicted from models with a mobile lid, i.e. plate tectonics (e.g. Kellogg

and Stewart, 1991; Samuel et al., 2011) whereas mixing in a stagnant lid model by O'Neill et al. (2013) suggests mixing operates on timescales more comparable to the present day. Mixing has been used to explore how isotopic reservoirs may form, yet the impact of mixing on the water cycle has not yet been explored.

Previous convection models have also focused their attentions on mantle water content, which is still up for debate. However, this leaves out an important piece of the puzzle, and possibly the most definitive constraint of the water cycle: the surface ocean mass. Recent studies have shown that using sea level can be a great constraint on the water cycle. Deep water contributions to sea level changes since 230 Ma shows regassing dominates during periods of continental break up and that deep water cycle contributions help to explain overall sea level changes (Karlsen et al., 2019). On longer timescales, persistent sea level records do not exist.

One method used is to assume 'continental freeboard', defined as the 'maximum elevation of a continent above mean sea level'. Calculating freeboard requires knowledge of how sea level has changed, understanding when continental crust was produced and how the ocean and continent volumes have varied over time. If ocean and continent volumes have been constant since the Archean, continental freeboard would also have been constant since then (Wise, 1974).

Korenaga et al. (2017) assume constant continental freeboard since $\sim$2.5 Ga but do not assume a constant ocean volume. They model a hypsometry that varies with evolving mantle temperature and conclude in order to maintain constant freeboard, ocean volume has been progressively decreasing estimated at 3×10^{11} kg/yr to 4.5×10^{11} kg/yr. This lies within the range of net change estimates from Section 1.5.

This thesis aims to understand the effects of mixing and further constrain how much water may reside in the mantle. Ideally, this would be carried out in fully 3D convection models, solving for evolving mantle temperature and water content across the entire mantle. However, owing to low resolution of these models at present and difficulties in modelling water transport processes throughout the mantle, parametrised models present a low cost (computation resources and time) solution. It will be shown that even with a simple yet representative convection model, impactful conclusions can be drawn, with the potential of extending into planetary sciences.

1.10 Summary

- 'Deep water' is H^+ accommodated in the structure of nominally anhydrous mantle minerals as a hydroxyl
- The deep water cycle consists of the surface and mantle interior reservoirs and water is transported between them at subduction zones and MORs
- How much water resides in the mantle?
- What are the effects of mixing are on planetary evolution?
- This thesis will use a parametrised convection model to investigate mixing and further constrain the amount of water in the mantle

2 Methods

2.1 Fluid Dynamics

Our understanding of mantle convection in planetary interiors has come from the application of fluid dynamics. The mantle can be modelled as a viscous fluid with two boundary layers: the hot core-mantle boundary (CMB) and the cold lithosphere. The mantle is also heated internally from radiogenic elements U^{238}, U^{235}, Th and K (Lay et al., 2008). Negatively buoyant subducting slabs sink into the mantle, forcing a passive flow of material towards the surface feeding MOR systems. Mantle plumes are positively buoyant rising from the CMB forming large igneous provinces (LIPs) and hotspot tracks if they reach the surface (Davies, 1998). These three transfer mechanisms are illustrated in Figure 1.1.

2.1.1 Dimensional Models

Flow in any viscous fluid is described by the Navier-Stokes equations. These consist of the conservation of mass (Eq. 2.1), conservation of momentum (Eq. 2.2), and conservation of energy (Eq. 2.3),

$$\underline{\nabla} \cdot \underline{u} = 0 \tag{2.1}$$

$$\frac{\partial \underline{u}}{\partial t} + (\underline{u}.\underline{\nabla})\,\underline{u} = -\frac{\nabla P}{\rho_0} + \nu \nabla^2 \underline{u} + \alpha \theta g \hat{\mathbf{y}} \tag{2.2}$$

$$\frac{\partial \theta}{\partial t} + (\underline{u}.\underline{\nabla})\,\theta = \kappa \nabla^2 \theta \tag{2.3}$$

from Turcotte and Oxburgh (1967) where $\underline{u}$ is the velocity vector, P is pressure, ρ_0 is a reference density, kinematic viscosity $\nu = \eta/\rho$, η is the dynamic viscosity and α is thermal expansivity. The temperature difference $\theta = T - T_0$, equivalent

to the difference between the mantle temperature T and the reference temperature T_0 that defines ρ_0. g is gravity, $\hat{\mathbf{y}}$ is the unit vector in the y-direction (Figure 2.1) and κ is thermal diffusivity. The Boussinesq approximation has been applied for an isoviscous mantle, where small changes in density have little effect in the inertial terms (left-hand side, LHS, of Eq. 2.2). However, the same small density changes are important in the body force (buoyancy) term, $\alpha\theta g\hat{\mathbf{y}}$, driving convection. This also allows the application of the incompressible form of the conservation equations, where density does not vary with pressure. Eq. 2.1 states no mass is created or destroyed. Eq. 2.2 gives the instantaneous viscous flow induced by lateral density variations and Eq. 2.3 advects these variations in time. This convective behaviour can also be used to examine the water cycle

$$\frac{\partial C_w}{\partial t} - \underline{u} \cdot \nabla C_w = 0 \tag{2.4}$$

where C_w is the mantle water content (Nakagawa et al., 2015; Price et al., 2019).

Although the conservation equations are presented in dimensional quantities, it is convenient to use non-dimensional variables. They simplify the equations making them easier to solve and independent of scale, allowing application to a variety of experimental environments (laboratory or numerical). Length, time, pressure and temperature scales are non-dimensionalised using Eqs. 2.5-2.9

$$\nabla = \frac{\widetilde{\nabla}}{d} \tag{2.5}$$

$$\underline{u} = \frac{\widetilde{\underline{u}}\kappa}{d} \tag{2.6}$$

$$P = \frac{\widetilde{P}\rho_0\nu\kappa}{d^2} \tag{2.7}$$

$$\theta = \widetilde{\theta}\beta d \tag{2.8}$$

$$t = \frac{\widetilde{t}d^2}{\kappa} \tag{2.9}$$

where $\sim$ denotes a non-dimensional quantity, d is mantle depth and β is the temperature gradient across the mantle ${}^{T_{bot}-T_{top}}/_{d} = {}^{\Delta T}/_{d}$ in the absence of convection.

Eqs. 2.1-2.3 become

$$\widetilde{\underline{\nabla}} \cdot \widetilde{\underline{u}} = 0 \tag{2.10}$$

$$\frac{\kappa}{\nu}\left[\frac{\partial \widetilde{\underline{u}}}{\partial t} + \left(\widetilde{\underline{u}}.\widetilde{\underline{\nabla}}\right)\widetilde{\underline{u}}\right] = -\widetilde{\nabla}\widetilde{P} + \widetilde{\nabla}^2\widetilde{\underline{u}} + \frac{\alpha\widetilde{\theta}\beta d^4 g\hat{\mathbf{y}}}{\kappa\nu} \tag{2.11}$$

$$\frac{\partial \widetilde{\theta}}{\partial \widetilde{t}} + \left(\widetilde{\underline{u}}.\widetilde{\underline{\nabla}}\right)\widetilde{\theta} = \kappa\widetilde{\nabla}^2\widetilde{\theta} \tag{2.12}$$

This condenses material properties into two non-dimensional parameters: the Prandlt number

$$Pr = \frac{\eta}{\rho\kappa} \tag{2.13}$$

and Rayleigh number

$$Ra = \frac{\rho\alpha\Delta T d^3 g}{\kappa\eta} \tag{2.14}$$

and Eq. 2.11 becomes

$$\frac{1}{Pr}\left[\frac{\partial \widetilde{\underline{u}}}{\partial t} + \left(\widetilde{\underline{u}}.\widetilde{\underline{\nabla}}\right)\widetilde{\underline{u}}\right] = -\widetilde{\nabla}\widetilde{P} + \widetilde{\nabla}^2\widetilde{\underline{u}} + Ra\widetilde{\theta}\hat{\mathbf{y}} \tag{2.15}$$

The Prandtl number is a ratio of momentum diffusivity to thermal diffusivity, describing whether it is easier for the system to transfer heat via conduction ($Pr < 1$) or advection of material ($Pr > 1$). For the Earth's mantle, $Pr >> 1$ with values $10^{21} - 10^{23}$ stating that advection of heat i.e. convection is the dominant heat transfer mechanism. When Ra (Section 1.7.2.1) exceeds a critical value $Ra_c \sim 10^3$ from linear stability analysis (Schubert et al., 2001), buoyant forces dominate and convection takes place and for Earth, $Ra = 10^6 - 10^8$. However, even with these simplifications, the equations can only be solved numerically in order to obtain 2D and 3D solutions.

2.1.2 Parametrised Models

An alternative to 2D and 3D convection models is to use parametrised convection models. As the computationally cheaper alternative, they allow a greater

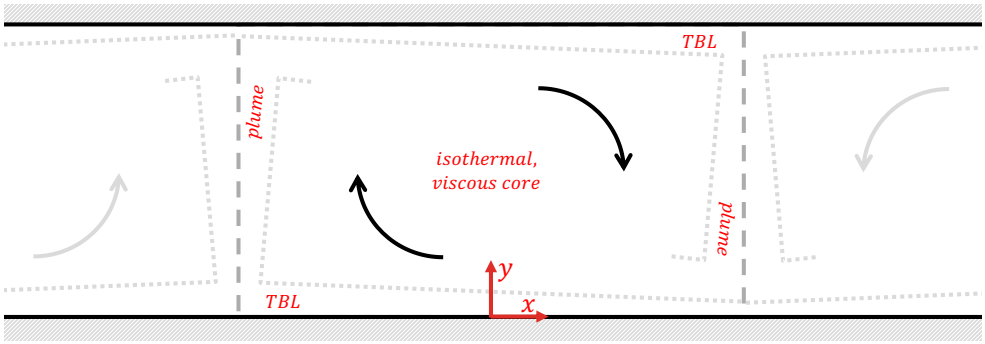

Figure 2.1: Mantle flow model applied to Eqs. 2.16 and 2.17, adapted from Turcotte and Oxburgh (1967).

examination of the parameter space. Parametrised convection models are built on an analytical solution to the conservation of mass, momentum and energy equations (hereafter the conservation equations) under a set of further simplifying assumptions, first proposed by Turcotte and Oxburgh (1967), outlined here. The equations are solved for steady convection. Flow is laminar between two horizontal boundaries, where the temperature of the lower boundary is greater than the temperature of the upper boundary and is restricted to 2D. For steady convection, time varying derivative terms can be neglected and the high Pr for Earth's mantle reduces the LHS of Eq. 2.15 to zero. Hence, Eqs. 2.12 and 2.15 become

$$-\widetilde{\nabla}\widetilde{P} + \widetilde{\nabla}^2\underline{\widetilde{u}} + Ra\tilde{\theta}\hat{\mathbf{y}} = 0 \tag{2.16}$$

$$\left(\underline{\widetilde{u}}.\underline{\widetilde{\nabla}}\right)\widetilde{\theta} = \kappa\widetilde{\nabla}^2\widetilde{\theta} \tag{2.17}$$

However, even with these further simplifications, the equations cannot be solved analytically and in order to reduce them further, Turcotte and Oxburgh (1967) prescribe a model (Figure 2.1) where the viscous fluid is divided into convecting rolls of opposing direction to the adjacent cell. Thin, thermal boundary layers (TBLs) form at the upper and lower boundaries, a result of the imposed temperature conditions. The meeting of two TBLs forms a plume that either rises to the surface or descend to the lower boundary. As either plume reaches the opposing boundary, they become part of the TBL. Whilst this spiralling behaviour forms many thermal layers, Turcotte and Oxburgh (1967) solve only for the flow of the first layer along cell boundaries.

The core of the convecting cell is considered isothermal as the temperature difference between the upper and lower boundaries are accommodated by the TBLs and Eq. 2.16 becomes

$$-\nabla P + \nabla^2 \underline{\widetilde{u}} = 0 \tag{2.18}$$

Using the stream function, this becomes the biharmonic equation

$$\nabla^4 \Psi = 0 \tag{2.19}$$

Variations of vertical velocity (v) in the x-direction though the plume may vary, giving the conditions $^{\partial v}/_{\partial x} = \gamma$ at its outer edge. This condition is also applied to the edge of the core where $x = \pm\delta$ (Figure 2.1), as the plume is thin. Together with applying free-slip conditions, the biharmonic equation is solved for the horizontal velocity u at the upper and lower boundaries

$$u = 0.0804\gamma \tag{2.20}$$

γ is unknown in the viscous core but can be determined in the plumes. Eq. 2.16 is re-written for the y-component valid within the plume

$$\frac{\partial^2 v}{\partial x^2} + \frac{\partial^2 v}{\partial y^2} = \frac{\partial P}{\partial y} - Ra\theta \tag{2.21}$$

Vertical changes in the plume are considered negligible compared with $Ra\theta$ and Eq. 2.21 becomes

$$-\frac{\partial^2 v}{\partial x^2} = Ra\theta \tag{2.22}$$

Integrating gives

$$\gamma \equiv -\left.\frac{\partial v}{\partial x}\right|_{\delta} = Ra\int_0^{\infty} \theta dx_2 \tag{2.23}$$

where x_2 is the distance from the centre of the plume ($x = \pm\delta$). γ ties the horizontal plate velocity to the material properties and temperature difference in the plume. With the initial temperature distribution of the plume, γ can be evaluated in terms of Ra and u

$$\gamma = 0.671 \frac{Ra}{u^{\frac{1}{2}}} \tag{2.24}$$

Substituting into Eq. 2.20,

$$u = 0.142 Ra^{\frac{2}{3}} \tag{2.25}$$

This relationship ties the interior behaviour of the convecting mantle to the surface, matching the order of plate velocities seen at the Earths surface. Velocity can be used to determine how fast the interior can cool and how the transfer of material between the interior and the surface can influence the water cycle.

2.2 Evolution Model

Parametrised models consider the behaviour of one convecting cell with one MOR and one subduction zone, scaling the results to an Earth-like planet (Figure 2.2).

Changes in average mantle temperature, T ($\sim$1400 km in K), and average mantle water content, X (in ppm normalised to the mass of the mantle), are a result of the inputs and outputs into the mantle system. The conservation of energy is

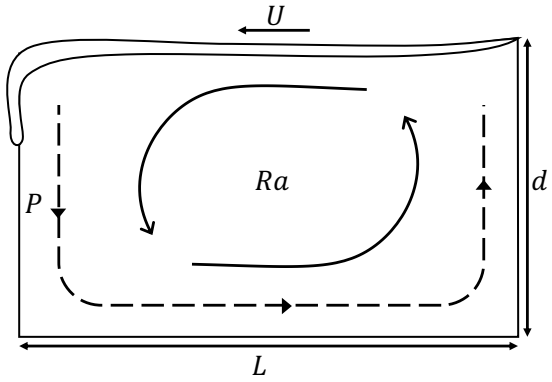

Figure 2.2: The convecting cell of length L and depth d with a convective vigour described by the Rayleigh number Ra. One subduction zone brings water into the mantle and one MOR removes water and heat from the interior, whilst radiogenic heating adds heat to the mantle.The time it takes for subducted material to reach a MOR along the path P is considered to be the mixing time τ either a constant value or dependent on Ra.

$$\frac{dT}{dt} = \frac{-Q_s + H}{\rho V c_p} \tag{2.26}$$

where the change in temperature $^{dT}/_{dt}$ is controlled by the difference between surface heat flow Q_s (heat out of the mantle) at MORs and radiogenic heating H. ρ is average mantle density, V is mantle volume calculated with a depth d of 2880 km, and c_p is heat capacity. The value for these constants and others are found in Table 2.1. H is

$$H = H_{sf} \sum_n \rho C_n H_n exp\left(\frac{ln2\,(t_{pd} - t)}{\tau_n}\right) \tag{2.27}$$

changing as radiogenic elements decay with time. It is the sum of the contributions from U^{238}, U^{235}, Th and K where C_n is concentration (of the n^{th} element), H_{sf} is the scale factor used to calibrate surface heat flow at 4.6 Gyrs, H_n is heat production, τ_n is radiogenic half life, t is time and t_{pd} is present day time of 4.6 Gyrs. Heat contributions are discussed further in Section 2.5.1.

Temperature decreases depending on the surface heat flow,

$$Q_s = 2Sk_cT\left(\frac{U}{\pi L\kappa}\right)^{\frac{1}{2}} \tag{2.28}$$

where S is surface area, k_c is thermal conductivity, L is plate length, U is plate velocity, and κ is thermal diffusivity. $^{L}/_{U}$ is equivalent to the plate age and S scales the surface heat flow to the planetary scale from a per unit length value.

$$\frac{dX}{dt} = \frac{R - D}{\rho V} \tag{2.29}$$

The change in water content in the mantle $^{dX}/_{dt}$ is proportional to the difference between regassing at subduction zones R and degassing at mid-ocean ridges D. The evolution of the surface ocean mass M is calculated similarly

$$\frac{dM}{dt} = \frac{D - R}{10^6 M_{pd}} \tag{2.30}$$

which gives the surface ocean mass in multiples of ocean mass for the present day, M_{pd} =1.39 $\times$ 10^{21} kg. Regassing is

$$R = \frac{S}{L} F_r d_l U \rho X_p \tag{2.31}$$

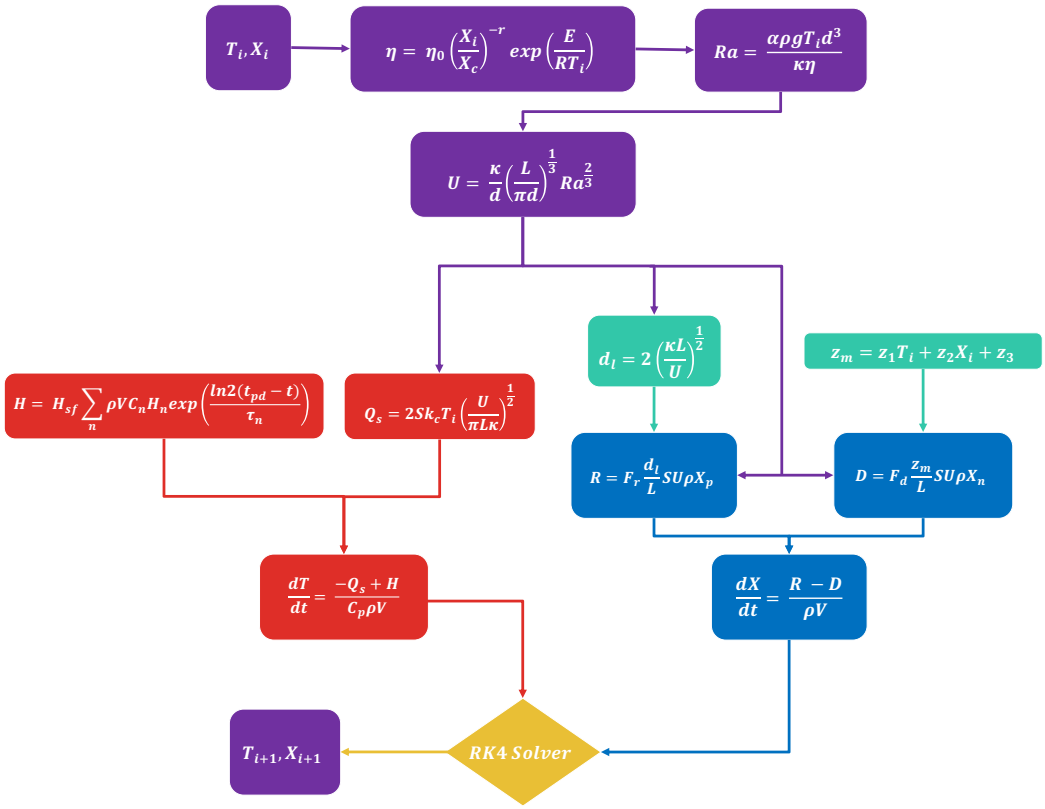

Figure 2.3: Calculation flow to determine the inputs and outputs for the conservation of energy and conservation of mass. Both are solved by the fourth order Runge-Kutta method, which determines the temperature and mantle water content for the next time step $i + 1$.

and varies with evolving plate thickness d_l which is also dependent on plate velocity U

$$d_l = 2\left(\frac{\kappa L}{U}\right)^{\frac{1}{2}} \tag{2.32}$$

as defined by the half-space cooling model (Davis and Lister, 1974). The mass of lithosphere subducted per unit length of subduction zone per unit time is equivalent to $d_l U \rho$ and contains a water content prior to subduction of X_p.

$$X_p = \sum_n \frac{\rho_n d_n X_n}{\rho_n d_n} \tag{2.33}$$

X_p is the average water content of a subducting package (Table 1.1) prior to any dehydration reactions where ρ_n, d_n and X_n are the corresponding density, thickness and water content of each layer n. With a dry lithospheric mantle

section of 85 km, the average slab contains approximately 2000 ppm. For the whole Earth, $d_l U \rho X_p$ is multiplied by the average length of subduction zones S/L (and MORs) giving the total flux of water into the subduction zone. F_r is the regassing efficiency and defines the fraction of water that makes it past the arc front (also known as the subduction factory).

Degassing is given by

$$D = \frac{S}{L} F_d z_m U \rho X \tag{2.34}$$

which varies with evolving U, X and melting depth z_m where

$$z_m = z_1 T_p + z_2 X + z_3 \tag{2.35}$$

T_p is potential temperature in degrees C (Mckenzie and Bickle, 1988) and z_1, z_2 and z_3 are constants. The mass per unit length of ridge that undergoes melting is equivalent to $z_m U \rho$ with the evolving mantle water content, X. For the whole Earth, $d_l U \rho X_p$ is multiplied by the average length of MORs S/L giving the total flux of water into the melt zone. The fraction of water partitioned between the solid mantle and melt is considered to be 1 (Asimow et al., 2004) such that all the water is partitioned into the melt and is not included as a separate parameter. F_d is the degassing efficiency, defining the fraction of water in the melt region that is released into the surface reservoir.

Surface heat flow (Eq. 2.28), regassing (Eq. 2.31) and degassing (Eq. 2.34) are all a function of the plate velocity U (Turcotte and Oxburgh, 1967)

$$U = \frac{\kappa}{d} \left(\frac{L}{\pi d} \right)^{\frac{1}{3}} Ra^{\frac{2}{3}} \tag{2.36}$$

which is dependent on the Ra (Section 2.1.2). It is defined as

$$Ra = \frac{\alpha \rho g T d^3}{\kappa \eta} \tag{2.37}$$

where α is thermal expansivity, g is gravity.

Parameters	Symbol	Value				Units	Reference
present day time	t_{pd}	4.6				Gyrs	-
thermal expansion	α	2.5×10^{-5}				K^{-1}	Schubert et al. (2001)
density	ρ	3500				kgm^{-3}	Schubert et al. (2001)
gravity	g	10				ms^{-2}	-
mantle depth	d	2.88×10^{6}				m	-
mantle volume	V	9.05×10^{20}				m^3	-
surface area*	S	3.62×10^{14}				m^2	-
average plate length	L	$2d$				m	-
specific heat capacity	c_p	1000				$Jkg^{-1}K^{-1}$	Crowley et al. (2011)
thermal conductivity	k_c	3				$Wm^{-1}K^{-1}$	Schubert et al. (2001)
thermal diffusivity	κ	$\frac{k_c}{c_p\rho}$				m^2	-
activation energy	E	3×10^{5}				$Jmol^{-1}$	Xu et al. (2011)
ideal gas constant	R	8.314				$Jmol^{-1}K^{-1}$	-
degassing efficiency	F_d	1				-	Crowley et al. (2011)
regassing efficiency	F_r	0.15				-	Schmidt and Poli (1998)
plate water content	X_p	2056				ppm	Table 1.1 and Section 2.2
melting depth constants**	z_1	286				mK^{-1}	Hirschmann et al. (2009)
	z_2	164				$mppm^{-1}$	
	z_3	-3.266×10^{5}				m	
elements	n	U^{238}	U^{235}	Th	K	-	
concentration	C_n	30.8	0.22	124	36.9	10^{-9} $kgkg^{-1}$	Schubert et al. (2001)
heat production	H_n	9.46	56.9	2.64	2.92	10^{-5} Wkg^{-1}	
half-life	τ_n	4.47	0.704	14	1.25	Gyrs	

Table 2.1: Table of constant parameters for the evolution model. *oceanic basin surface area of Earth. F_d and F_r values are considered constants unless otherwise stated (Chapter 5).

The various constants in this model are chosen to reflect the mantle today (summarised in Table 2.1). Values for α, ρ, c_p and k_c are more consistent with upper mantle conditions; mid-mantle (average) values are α =1 K^{-1} to 2 K^{-1} (Wolf et al., 2015), ρ =4000 kgm^{-3} to 5000 kgm^{-3} (Dziewonski and Anderson, 1981; Wolf et al., 2015), c_p =500 Jkg^{-1} to 800 Jkg^{-1} (Okuda et al., 2019) and k_c =4 $Wm^{-1}K^{-1}$ to 6 $Wm^{-1}K^{-1}$ (Hsieh et al., 2017). If these values and most others in Table 2.1 are varied, this will inevitably cause differences in the evolution. However, these differences are minimised by constraining Q_s to present day values by varying H_{sf} (Section 2.5.1). This limits the variations in both temperature and water content evolution by constraining how the mantle cools, minimising the effects of varying constant parameters.

Most values in Table 2.1 are not expected to vary more than one order of magnitude over mantle conditions throughout evolution in the solid state whereas viscosity is expected to vary more than an order of magnitude due to temperature and water dependencies. Therefore, constants in the viscosity law and the water dependence of viscosity are further explored in Chapter 3. Figure 2.3 summarises the calculations described in this section.

2.3 Mixing Implementation

The model presented in the previous section implies that any subducted water is instantaneously mixed into the mantle and homogeneously distributed. Mixing is implemented in the water cycle as a time lag between subduction and release to the surface ocean via degassing at the MOR. This time lag is considered as the mixing time τ i.e. the time for subducted material to become incorporated into the convecting mantle and be sampled by a MOR. The path P, represented in Figure 2.2, is considered to be taken by a subducted package. The time taken to travel this path can either be (a) constant or (b) variable, representing two end member cases. Constant mixing uses a single mixing time that does not change over the course of the model. Variable mixing changes the mixing time with Ra, such that when Ra is high, convection is vigorous and the mixing time is short and when Ra is low, convection is sluggish and the mixing time is long. By including mixing, this inherently implies that there are different mantle water contents to consider. Two water contents are tracked over the course of the model: (1) the global average water content X and (2) the water content at the MOR $X\left[\tau_{(Ra)}\right]$.

$X\left[\tau_{(Ra)}\right]$ is dependent on constant τ for constant mixing $X[\tau]$ or variable τ_{Ra} for variable mixing $X[\tau_{Ra}]$.

2.3.1 Constant Mixing

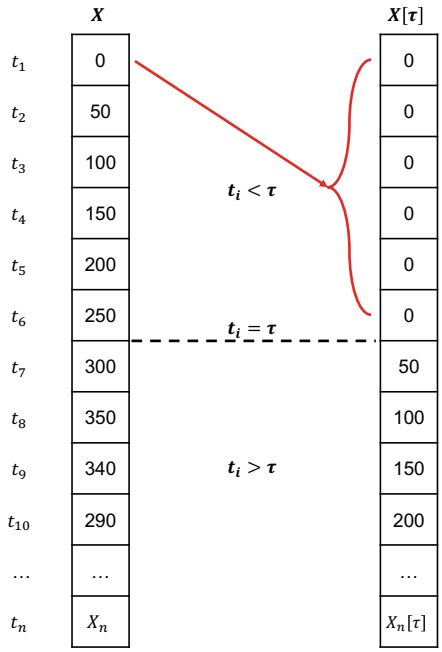

Figure 2.4: Constant mixing schematic for X and $X[\tau]$ arrays. When the model time t is less than the mixing time τ, the water content at the ridge $X[\tau]$ is prescribed the initial whole mantle water content X. When $t > \tau$, $X[\tau]$ is equivalent to X at τ years ago.

Take a mantle that is dry and water begins in a surface ocean, with, for example, $\tau = 1$ Gyrs. For a constant mixing time, the water content of the material feeding the ridge is given by

$$X[\tau] = X[t_i - \tau] \tag{2.38}$$

equivalent to the global water content with a 1 Gyrs time delay. Figure 2.4 shows an example array for X and $X[\tau]$. During the beginning of the model, water may be subducted into the mantle but it cannot yet have reached the MOR to be degassed. At these times, $t_i < \tau$ and the water content at the ridge is equivalent to the starting mantle water content i.e. $X_1 = 0$ ppm. Once $t_i > \tau$, water begins to arrive at the ridge and is equivalent to the water content 1 Gyrs ago. When calculating the evolution (Section 2.2), $X[\tau]$ is carried forward and the water content at the MOR is used to calculate the changes in temperature and water content (Figure 2.4).

2.3.2 Variable Mixing

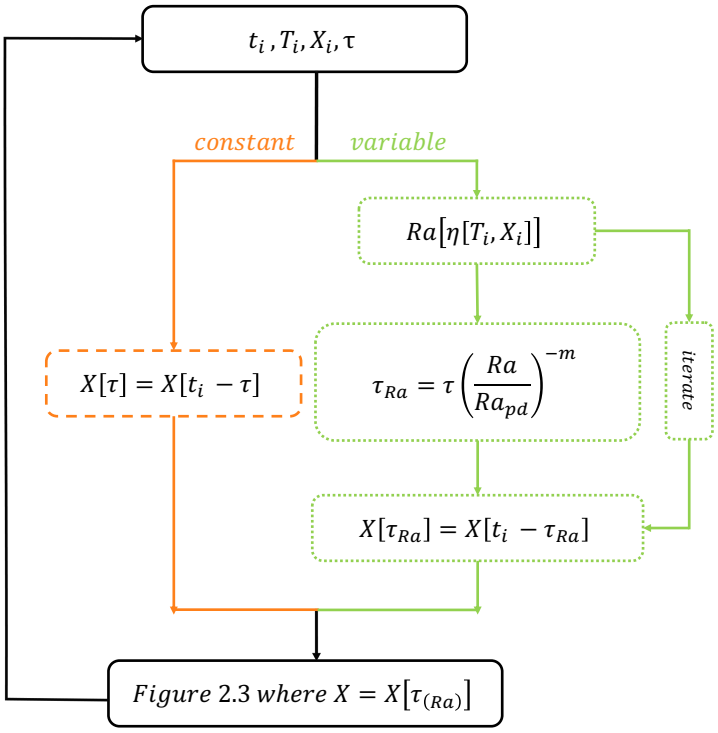

Figure 2.5: Mixing flow chart summarising the steps required to calculate the water content at the ridge for constant and variable mixing. The MOR water content is then used to calculate how the mantle temperature and mantle water content evolve (Figure 2.3 and Section 2.2).

A subducted package travelling along P in Figure 2.2 traverses a distance of $2d + L$. Convection occurs with a vigour Ra and associated plate velocity U (Eq. 2.25). With the distance $P = 2d + L$ and velocity $U \propto Ra^{2/3}$, the time taken to travel this distance i.e. the mixing time

is

$$\tau_{Ra} \propto Ra^{-\frac{2}{3}} \tag{2.39}$$

This relationship states that when convective vigour is high, the mixing time τ_{Ra} is short; when convective vigour is sluggish and Ra is low, τ_{Ra} is long as shown by Samuel et al. (2011). Variable mixing time is calculated as

$$\tau_{Ra} = \tau\left(\frac{Ra\,[T_i, X_i]}{Ra_{pd}}\right)^{-m} \tag{2.40}$$

where τ is a prescribed mixing time scaled by Ra dependent on the average mantle temperature T_i and global water content X_i. Ra_{pd} is the present day Rayleigh number (10^6) and m is the mixing exponent equal to $2/3$ for the classical scaling from Turcotte and Oxburgh (1967).

The water content at the ridge is given as

$$X\left[\tau_{Ra}\right] = X\left[t_i - \tau_{Ra}\right] \tag{2.41}$$

As with constant mixing, when $t_i < \tau_{Ra}$ the water content at the ridge is equivalent to the starting mantle water content e.g. $X_1 = 0\,\text{ppm}$. When $t_i > \tau_{Ra}$, $X\left[\tau_{Ra}\right]$ is no longer equivalent to a simple shift in X, due to the time-varying nature of τ_{Ra}. This also requires iterating over $X\left[\tau_{Ra}\right]$ and smoothing around τ_{Ra} such that $X\left[t_i - \tau_{Ra}\right]$ is an average of an array where i is from $i-2$ to $i+2$.

2.4 Ocean Mass to Sea Level

In order to assess the impact of the water cycle (Section 2.2) on the surface, sea level is considered. To the first order, sea level is dependent on the ocean mass and the ocean basin, which is defined by surface topography. The evolving ocean mass is the solution to Eq. 2.29. The present day surface topography can be described by its hypsometry, defined as elevation to a reference sea level with respect to the surface area (cumulative fraction). This is well known for the present day (Amante and Eakins, 2009) and can also be calculated by considering the isostatic balance of continental and oceanic crust. To calculate the hypsometric curve for the present day, the procedure outlined by Korenaga et al. (2017) is followed. The curve is split into two main sections representing oceanic and continental crust.

2.4.1 Bathymetry

Bathymetry z_b is calculated according to the half-space cooling model (Davis and Lister, 1974)

$$z_b = d_0 + b_0\sqrt{\tau} \tag{2.42}$$

where d_0 is the present day MOR depth of $2654\,\text{in m}$, $b_0 = 323\,\text{mMa}^{-0.5}$ and τ

is the plate age in Ma. Plate age is converted to surface area using an area-age distribution

$$\frac{dA_o}{d\tau} = G_0 \left(1 - \frac{\tau}{\tau_{max}}\right) \tag{2.43}$$

where A_o is the area of oceanic crust, $G_0 = 3.45\,\mathrm{km^2 yr^{-1}}$ and τ_{max} is the maximum plate age. The cumulative integral of this curve divided by the surface area of Earth gives the cumulative fractional surface area below 0.575.

2.4.2 Continental Topography

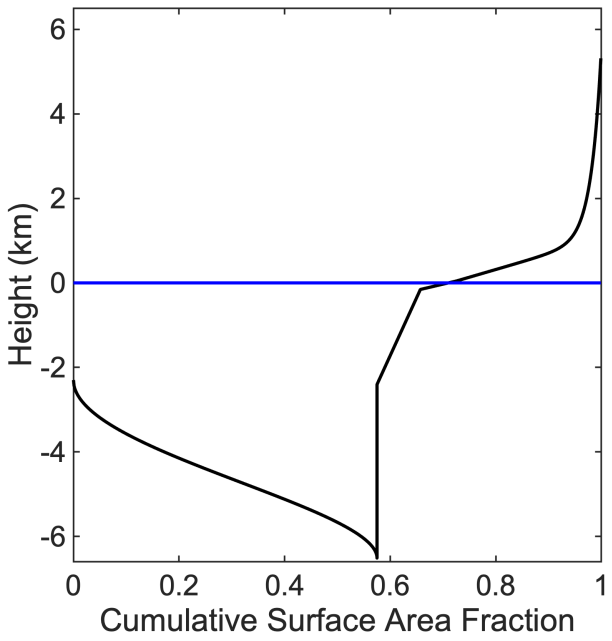

Figure 2.6: The present day hypsometric curve is represented by the black line and the blue line represents the present day sea level, defined as zero.

Above 0.575, the hypsometry is defined empirically by continental crust z_c, and approximated in three sections:

(i) continental shelf $0.575 < x < 0.657$

$$z_c = a_1 + a_2 x$$

where x is cumulative surface area fraction, a_1 = -18.49 and a_2 = 27.36

(ii) continental slope $0.657 < x < 0.725$

$$z_c = a_3 + a_4 x$$

where a_3 = -2.437 and a_4 = 2.932

(iii) sub-aerial crust $0.657 < x < 1$

$$z_c = a_5 + a_6 x + a_7 exp\left[a_8 \left(x - 1\right)\right]$$

where a_5 = -2.952, a_6 = 3.642, a_7 = 4.5 and a_8 = 52.03.

For the present day, sea level is considered at 0 km and intersects at a cumulative surface area fraction of 0.71 i.e. 71% of the Earth's surface is under water. The present day hypsometric curve is shown in Figure 2.6.

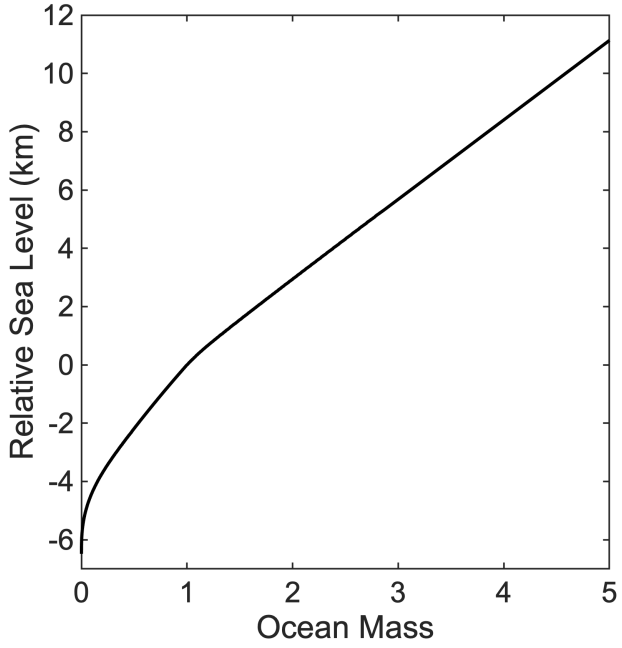

Figure 2.7: Ocean mass-sea level relationship, described in Section 2.4.3.

2.4.3 Calculating Sea Level from Ocean Mass

Before the evolving surface ocean mass from Section 2.2 can be converted to sea level, a relationship between ocean mass and sea level must be established. Integrating between sea level and the hypsometry (for the fraction < 0.71) gives

the ocean volume for the present day and assuming the water in the surface ocean has a density of $1000\,\mathrm{kgm}^{-3}$, the ocean mass.

For a range of sea levels, integrating between the two curves using the trapezoid method gives a complex relationship between the ocean mass and sea level (Figure 2.7). For ocean masses > 2, there are no intersections with the hypsometry and sea level increases linearly with ocean mass. For ocean masses < 2, sea level intersects with the non-linear hypsometry resulting in a complex relationship between ocean mass and sea level. As a result, this data set is interpolated for the evolving ocean mass values.

2.5 Initial and Constrained Conditions

As this convection model is concerned with the solid-state mantle, assumptions must be made about the origins of heat and water and the evolution prior to mantle solidification.

2.5.1 Temperature and Surface Heat Flow

Mantle heat is dominated by primordial heat, heat from the core and radiogenic heat. Primordial heat was generated during accretion, a result of impacts and latent heat release during differentiation (Breuer, 2011). The core continues to heat the mantle from below whilst the radiogenic elements U^{238}, U^{235}, Th and K provide heat from within the layer. These contributions result in a present day surface heat flow of $46 \pm 3\,\mathrm{TW}$ measured from boreholes. How the three sources of heat contribute to this total value is unclear. Geological evidence of K/U and Th/U ratios (Schubert et al., 2001) suggest that $\sim 20 \pm 3\,\mathrm{TW}$ are a result of radiogenic contributions, 6 TW to 8 TW of which are in the continental crust; 5 TW to 15 TW are from the core and 8 TW to 25 TW are from primordial heat (Lay et al., 2008; Jaupart et al., 2015). However, in a effort to minimise the number of parameters, only the radiogenic contribution is implemented (Section 2.2). Rather than representing only the radiogenic contribution, it is scaled such that by the present day at 4.6 Gyrs, $Q_s = 46\,\mathrm{TW}$, in lieu of considering all three contributions separately. The radiogenic contribution currently residing in the crust is the result of repeated melting. However, at the start of solid state mantle convection, this would have been distributed throughout the mantle. As

this model does not consider the partitioning of heat producing elements, these elements remain in the mantle, contributing to the convective regime.

The initial temperature of the mantle is unknown and previous parametrised convection models show that these models cannot be used to distinguish between different starting temperatures (e.g. Williams and Pan, 1992). Instead, the initial mantle temperature is assumed to be 300 K (Grove and Parman, 2004; Condie et al., 2016) higher that the present day average mantle temperature 2200 K (Schubert et al., 1980; Sandu et al., 2011).

2.5.2 Mantle Water Content

Cometary impacts were generally considered to have brought water to a dry proto-Earth (e.g. Hartogh et al., 2011). However, analysis of high $^{D}/_{H}$ ratios from the ROSETTA mission suggests the cometary contribution of water on Earth is less than 1% (Marty et al., 2016). Low $^{D}/_{H}$ ratios found in Icelandic and Baffin Island lavas suggest that water adsorbed onto grains in the protosolar nebula has survived in the mantle since that time (Hallis et al., 2015), building the argument for water retention throughout accretion.

There are two main models of planet formation: pebble and planetesimal accretion.

Pebble accretion concerns objects on the centimetre up to the metre scale, spiralling onto larger bodies and increasing their size. This process may retain anywhere on the order of 100 ppm to 10 000 ppm of water (Ida et al., 2019). Planetesimal accretion increases the size of a protoplanet via collisions with bodies on the scale of 1 km to 100 km. The migration of Jupiter and Saturn (Grand Tack model) are thought to have brought hydrous asteroids (C-type) to the inner solar system and through the accretion of these bodies, introduce water to the rocky planets as they formed (Hallis, 2017). As with pebble accretion, it is not clear how much water is retained through the collisions of these larger bodies. Hypervelocity impact experiments suggest up to 30% of the initial water content can be retained (Daly and Schultz, 2018) and models that include decaying ^{23}Al degasses planetesimals reducing the amount of water in asteroids. ^{23}Al rich asteroids form 'water-poor' planets such as Earth and Mars, indicating that less water may be retained than in pebble accretion. In reality, the growth of a planet is likely to be a combination of both pebble and planetesimal accretion and the fate of water throughout also likely to be a combination of the two.

Giant impacts are particularly important when considering the formation of Earth, especially the Moon forming impact. There is geochemical evidence of multiple giant impacts which would have induced magma oceans (Tucker and Mukhopadhyay, 2014). Magma oceans can contain water (Olson and Sharp, 2018) but their solidification has been shown to effectively degas the mantle (Elkins-Tanton, 2011). This adds water to the atmosphere and once conditions become stable, the atmosphere collapses into a surface ocean. Further work has shown that due to the partition coefficient between solid and melt, lower mantle water would be transported to the upper mantle where hydrous minerals such as wadsleyite and ringwoodite can hold on the order of 10 000 ppm, potentially holding onto water (Tikoo and Elkins-Tanton, 2017). However, as previously discussed (Section 1.3) the water capacity of mantle minerals at temperatures just after solidification are unknown. Experiments have shown that capacity should be reduced (Ohtani et al., 2000; Litasov and Ohtani, 2003)and this would also reduce the amount of water retained as the magma ocean solidifies, but further work is needed to understand this phenomena quantitatively.

Most previous models begin with water in the mantle (e.g. Crowley et al., 2011; Sandu et al., 2011) and whilst tests are shown in Chapters 3 and 5, and Appendix C beginning with water in the mantle, the preferred starting scenario begins with no water in the mantle.

2.6 Summary

- Parametrised models are based on an analytical solution to the conservation equations where horizontal plate velocity is proportional to $Ra^{2/3}$
- Thermal evolution is solved by calculating the heat produced and lost over each time step, giving how average mantle temperature changes over time
- Average mantle water content (ocean mass) evolution is solved by calculating how much water is subducted into and degassed from the mantle
- Mixing in the water cycle is incorporated into the parametrised models as a time delay between subduction and degassing at the mid-ocean ridge
- Present day hypsometry is used to establish a relationship between sea level and ocean mass, allowing the conversion of surface ocean mass evolution to sea level evolution

- Further comparison of sea level to the hypsometry gives the fraction of topography exposed to the atmosphere

3 Viscosity Law Controls on Thermal Evolution

Viscosity is one of the fundamental parameters that govern mantle convection and therefore planetary evolution. Understanding how different viscosity laws are implemented in convection models becomes key due to feedbacks in both thermal evolution and the water cycle (Sections 1.6 and 1.8).

As previously discussed, viscosity is dependent on mineral type, pressure (depth) conditions and deformation mechanism. Viscosity is non-linear, dependent on spatial (down to grain-scale) heterogeneity. The effect of water on these minerals and at the various conditions of the mantle are also variable with depth and mineral. However, the parametrised convection model, chosen for its low cost approach to explore the parameter space, should only be used to discuss the average characteristics of the mantle flow (Tozer, 1965; Schubert et al., 1980). The viscosity law should therefore represent the 'average' mantle, both in space and mineralogy. In order capture the representative average behaviour, a simplified viscosity law with the 'average' effects of temperature and water are considered. Present day estimates for average mantle temperature, mantle viscosity and plate velocity are also considered to constrain a representative evolution.

When considering the water-dependency of mantle minerals, experiments are limited to the upper mantle and transition zone conditions. Whilst lower mantle first principles calculations for bridgmanite do exist, the results are inconclusive (Section 1.6). Li et al. (2008) coupled measured water contents of peridotitic xenoliths with a flow law (Mei and Kohlstedt, 2000b) forming a viscosity law that calculated fugacity from water contents. However, these experiments were carried out at relatively low temperatures and pressures, restricting applicability to the lithosphere, and not the bulk convecting mantle. Single crystal experiments (Fei et al., 2013) at 8 GPa and between 1600 K to 1800 K show an order of magnitude decrease in viscosity whereas data from polycrystalline experiments extrapolated

to higher pressures suggests that water may reduce viscosity by three orders of magnitude (Karato et al., 1986; Mei and Kohlstedt, 2000a; Jung and Karato, 2001).

Water-dependent laws are implemented in various ways in parametrised models. Jackson and Pollack (1987) include a time varying activation temperature (equivalent to activation energy) to test the effects of water on rheology whereas Crowley et al. (2011) and Sandu et al. (2011) implement the water-dependence through a water fugacity (Li et al., 2008). More recently and in a 2D model, Nakagawa et al. (2015) incorporated the order of magnitude effect as a power law function of mantle water content following the work of Fei et al. (2013) and this is the approach adopted in this thesis.

When testing these laws, a calibration point is chosen where laws cross with a water-independent law. This value is often regarded as an expected mantle content such as 500 ppm by Sandu et al. (2011) and 620 ppm by Nakagawa et al. (2015). However, any calibration point greater than zero implies when no water is present, the viscosity is a possible range, dependent on the law. In convection models, this results in higher viscosities when laws are water-dependent (Crowley et al., 2011; Sandu et al., 2011; Nakagawa et al., 2015). This calibration method ensures the convergence of evolution towards the present day but the resulting viscosity when water content is zero (dry), is not supported by experiments.

Testing multiple viscosity laws increases the size of the parameter space to be searched. In order to constrain behaviour applicable to Earth, various observables are considered. Average, mid-mantle ($\sim$1400 km) temperatures of 2200 K are expected for the present day, equivalent to a mantle potential temperature of 1600 K (Mckenzie and Bickle, 1988). Today, plate velocities range from $\leq$1 cm/yr to 10 cm/yr, with early estimates of absolute plate motion by Gordon et al. (1978) and more recently, data from global positioning satellites (GPS) (Larson et al., 1997). Lastly, present day mantle viscosity is constrained by glacio-isostatic rebound, where the viscosity of the underlying mantle controls the uplift (rate) of the surface. Coupled with tectonic plate motions and free-air gravity data, Mitrovica and Forte (2004) show mantle viscosity can vary radially up to three orders of magnitude. For the mid-mantle, this range is from 10^{21} Pa s to 10^{23} Pa s (Rudolph et al., 2015), in agreement with bridgmanite viscosity estimated from first principles simulations at these depths (Ammann et al., 2010).

With these constraints, this chapter aims to constrain which viscosity law (water-independent or water-dependent) is most representative of Earth when consider-

ing evolution in the model described by Section 2.2.

3.1 Calibrating the Laws

The evolution is calculated using the parametrised model outlined in Section 2.2. The evolution depends on the average, mid-mantle (∼1400 km) temperature which for the present day is equivalent to ∼2200 K (Schubert et al., 1980). As bridgmanite makes up 60% of the mantle (Section 1.2), it's properties may also have a controlling factor in the evolution (e.g. Wang et al., 2013). The temperature dependence is captured through the well established Arrhenius equation and the activation enthalpy of bridgmanite is adopted. The average mantle viscosity η is given by

$$\eta = \eta_0 \left(\frac{X}{X_c}\right)^{-r} exp\left(\frac{E}{RT}\right) \tag{3.1}$$

where η_0 is a calibration viscosity, X is the water content in ppm, X_c is the calibration water content, the r exponent controls the sensitivity to water content, the activation energy $E = 300\,\mathrm{kJ\,mol^{-1}}$ (Xu et al., 2011), the ideal gas constant $R = 8.314\,\mathrm{J\,mol^{-1}\,K^{-1}}$ and T is average mantle temperature. For a given η, varying E results in different a different value of η_0 with minimal effects on evolution.

All evolution cases are calibrated to give 46 TW (Lay et al., 2008) surface heat flow and one surface ocean mass by 4.6 Gyrs. Each case begins at 2500 K as 300 K of cooling is expected from geochemical data (Condie et al., 2016). Both the present day mantle temperature and viscosity estimates constrain the range of viscosity laws that govern Earth's evolution when the viscosity law is dry.

3.1.1 Water-Independent Viscosity

For Eq. 3.1 to give a viscosity law only dependent on temperature, $r = 0$ (hereafter, $O(0)$). η_0 is varied in order to give calibrate the viscosity such that at mid-mantle present day temperatures of 2200 K, η is 10^{21} Pas to 10^{23} Pas (Mitrovica and Forte, 2004). This gives $\eta_0 = 7.53 \times 10^{13}\,\mathrm{Pa\,s}$ to $7.53 \times 10^{15}\,\mathrm{Pa\,s}$. These values for η_0 are tested within the evolution model in order to assess their effect on thermal history. The case resulting in a temperature of ∼2200 K at 4.6 Gyrs is used as the basis to test various water-dependent laws.

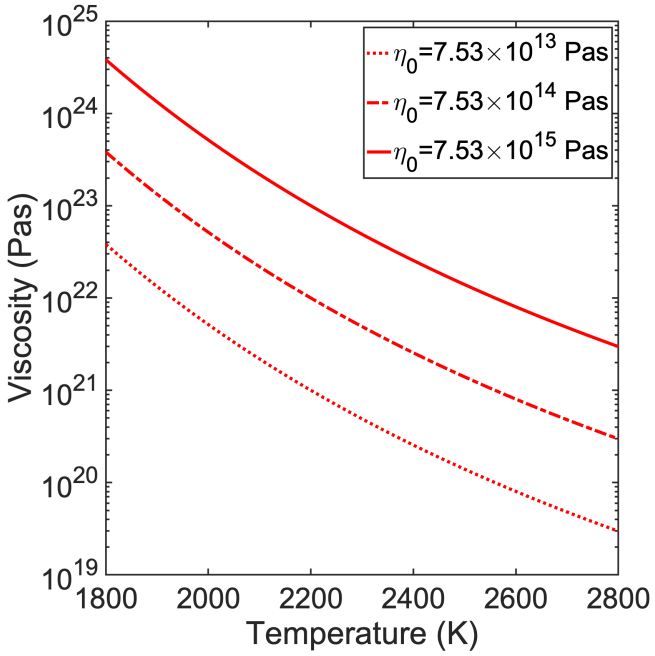

Figure 3.1: Three values of η_0 are chosen to give 10^{21} Pa s to 10^{23} Pa s (Ammann et al., 2010) for an average mantle temperature for the present day 2200 K

3.1.2 Water-Dependent Viscosity

The water dependency in viscosity is tested from two aspects: (a) the sensitivity to water content, determined by the exponent r and (b) 'model' or 'experimental' type laws, determined by the variable X_c. The values are summarised in Table 3.1 and their dependency on water is shown in Figure 3.2. For $r = 0.3$, viscosity varies one order of magnitude for 1000 ppm whilst for $r = 1$, viscosity varies three orders of magnitude, hereafter $O\,(1)$ and $O\,(3)$, respectively. X_c determines the cross-over point between the three laws $O\,(0)$, $O\,(1)$ and $O\,(3)$. When the cross-over is 1 ppm, this represents laws determined by laboratory experiments (Fei et al., 2013). When X_c is 500 ppm, this represents 'model' laws such that when conditions in the model match present-day conditions for Earth, the evolution for each law overlaps (e.g. Sandu et al., 2011; Nakagawa et al., 2015). The effects of r and X_c on thermal evolution and the water cycle are tested, with $O\,(0)$ for comparison.

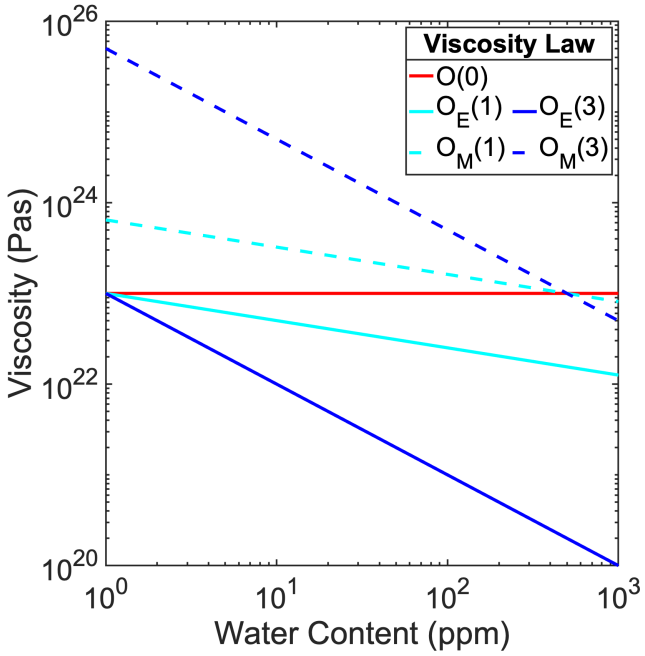

Figure 3.2: Water-dependent viscosity laws defined in Eq. 3.1 and Table 3.1. Solid lines represent 'experimentally' constrained laws and dashed lines represent laws constrained to give the same present day conditions in (parametrised) convection models. Colour represents the approximate order variation in viscosity where red is a water-independent viscosity law $O(0)$, cyan is water-dependent varying $O(1)$ and blue varies $O(3)$.

3.2 Effect on Plate Velocity

3.2.1 Water-Independent Law

When the viscosity law is water-independent, viscosity is defined by temperature. For the three values of η_0, the same temperature defines three different viscosity values (Figure 3.1). Each of these defines a convective vigour (Eq. 2.37) and associated plate velocity (Eq. 2.36). Hence as the mantle temperature evolves, the plate velocity will also evolve.

For $\eta_0 = 7.53 \times 10^{13}\,\mathrm{Pa\,s}$, $\eta\,(t=0)$ is $1.4 \times 10^{20}\,\mathrm{Pa\,s}$. This relatively low viscosity (Figure 3.1) gives a plate velocity on the order of hundreds of centimetres per year, unrealistically large velocities that would be easily visible at the Earth's surface today. As the temperature decreases, viscosity increases, resulting in a plate velocity of 7 cm/yr by 4.6 Gyrs.

For $\eta_0 = 7.53 \times 10^{14}\,\mathrm{Pa\,s}$, $\eta\,(t=0)$ is $1.4 \times 10^{21}\,\mathrm{Pa\,s}$. This higher starting vis-

Law	X_c (ppm)	Sensitivity	r	Dry Mantle Start		Wet Mantle Start
				$M\,(t=0)$	H_{sf}	$X\,(t=0)$
Water-Independent	–	$O(0)$	0	1.723	1.706	756
Experimental	1	$O_E\,(1)$	0.3	1.887	1.724	828
		$O_E\,(3)$	1	2.487	1.783	1091
Model	500	$O_M\,(1)$	0.3	1.702	1.677	749
		$O_M\,(3)$	1	1.651	1.590 1.604	732

Table 3.1: Parameters for 'experimental' and 'model' type viscosity law tests, corresponding to Eq. 3.1. η_0 is 7.53×10^{15} Pa s and T =2500 K for all cases (after calibrating the temperature-dependent viscosity law). For a dry mantle start, all the water in the system begins at the surface (Figure 3.4) whilst for a wet mantle start, all the water in the system begins in the mantle (Figure 3.5). H_{sf} is used to scale the surface heat flow Q_s to 46 TW at 4.6 Gyrs and both M_s and X are used to calibrate the surface ocean mass to one at 4.6 Gyrs.

cosity reduces the plate velocity to ∼100 cm/yr. The decrease in temperature is more gradual hence changes in viscosity are also less extreme. But despite the order of magnitude difference in starting viscosity, the plate velocity at 4.6 Gyrs is 5.8 cm/yr.

For $\eta_0 = 7.53 \times 10^{15}$ Pa s, $\eta\,(t=0)$ is 1.4×10^{22} Pa s. The higher starting viscosity reduces the plate velocity to ∼20 cm/yr at the start of the model. As the temperature rises, viscosity decreases and plate velocity increases. Increasing the starting viscosity by another order of magnitude again only reduces plates velocity by ∼1 cm/yr to 4.6 cm/yr. All three cases have plate velocities at 4.6 Gyrs within the range of plate velocities observed on Earth today. Only $\eta_0 = 7.53 \times 10^{15}$ Pa s has realistic velocities for the majority of the evolution time and is subsequently used to assess the effect of water-dependent laws.

3.2.2 Water-Dependent Laws

When the viscosity law is water-dependent, viscosity is defined by both mantle temperature and mantle water content. This means that plate velocity will also depend on the mantle temperature and water content throughout the model. When water begins in the surface ocean, mantle water content increases over the course of the model. Temperature shows a heating period (of variable length) followed by cooling over the course fo the model.

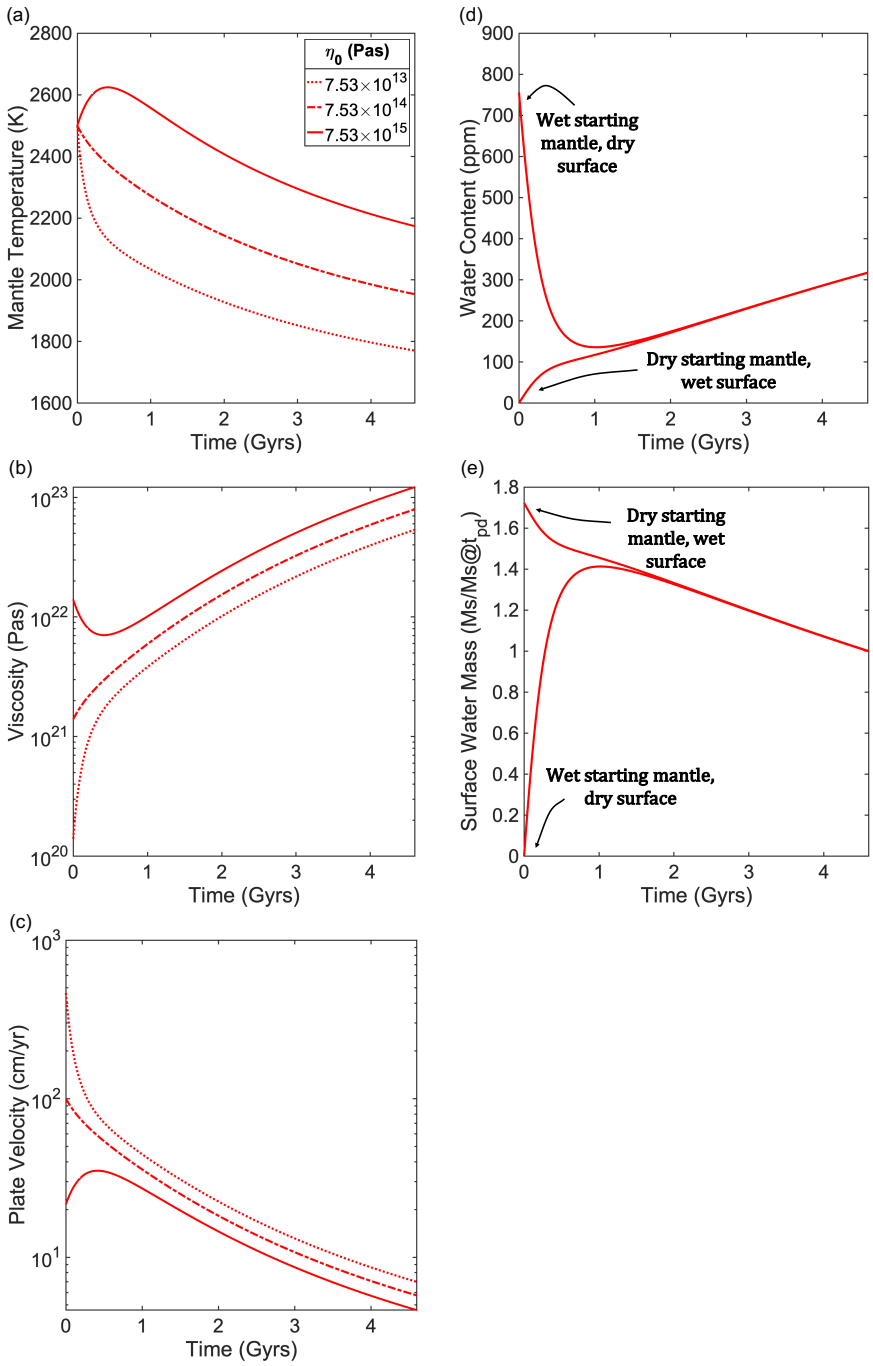

Figure 3.3: (a) Temperature, (b) viscosity and (c) plate velocity evolution for each water-independent viscosity law given by Eq. 3.1 and shown in Figure 3.1. Higher η_0 increases viscosity at the beginning of the model. For η_0 =7.53 × 10^{15} Pa s, the water cycle evolution is shown for the (d) mantle interior and (e) surface ocean. Two cases show the evolution of water mass in these two reservoirs, whether the water begins in the mantle or at the surface.

3.2.2.1 Dry Start

For 'experimental' laws $O_E\,(1)$ and $O_E\,(3)$, starting with an initial temperature of 2500 K and mantle water content 0 ppm give the same starting viscosity of 1.4×10^{22} Pa s (Figure 3.4d). Mantle water content increases but for $O_E\,(1)$ and $O_E\,(3)$, the response in viscosity will be different. As $O_E\,(3)$ has a higher sensitivity to water content, the decrease in viscosity is rapid when compared with $O\,(0)$ and $O_E\,(1)$. Once the mantle begins to cool, viscosity increases and plate velocities decrease. $O_E\,(1)$ and $O_E\,(3)$ ends with $U = 5.5$ cm/yr and $U = 8.1$ cm/yr, respectively.

For 'model' type laws, the same starting conditions (2500 K and 0 ppm) do not give the starting starting viscosities. Instead, $O_M\,(1)$ and $O_M\,(3)$ begin with viscosity of 9×10^{22} Pa s and 7×10^{24} Pa s, with corresponding initial plate velocities of 6 cm/yr and 0.3 cm/yr. Increasing temperature and increasing water content act to decrease the viscosity, and plate velocities increase. After this initial divergence in behaviour, $O\,(0)$, $O_M\,(1)$ and $O_M\,(3)$ begin to cool and converge such that there is little difference in mantle conditions by 4.6 Gyrs.

3.2.2.2 Wet Start

For 'experimental' laws, mantle water content rapidly decreases followed by a steady increase whilst temperature decreases throughout. Starting with water in the mantle gives different starting viscosities. This high mantle water content reduces the starting viscosity and as $O_E\,(3)$ has a higher sensitivity to water content and hence begins with the lowest viscosity (Figure 3.5d), $\sim 1 \times 10^{19}$ Pa s. This translates to the highest plate velocity (Figure 3.5e), approximately three orders of magnitude higher than is seen today. Rapid degassing and cooling increases viscosity, decreasing plate velocity to tens of centimetres per year by 0.5 Gyrs. Again, by 4.6 Gyrs, plate velocity decreases to 5.5 cm/yr and 8.1 cm/yr for $O_E\,(1)$ and $O_E\,(3)$, just as for starting with a dry mantle.

For 'model' laws, the hydrous starting condition of the mantle produces a much smaller range of initial viscosities $\sim 1 \times 10^{22}$ Pa s, as mantle water content is greater than X_c. The initial viscosities are slightly less than $O\,(0)$ and hence plate velocities are marginally faster. Decreasing mantle water content increases viscosity such that it exceeds $O\,(0)$.

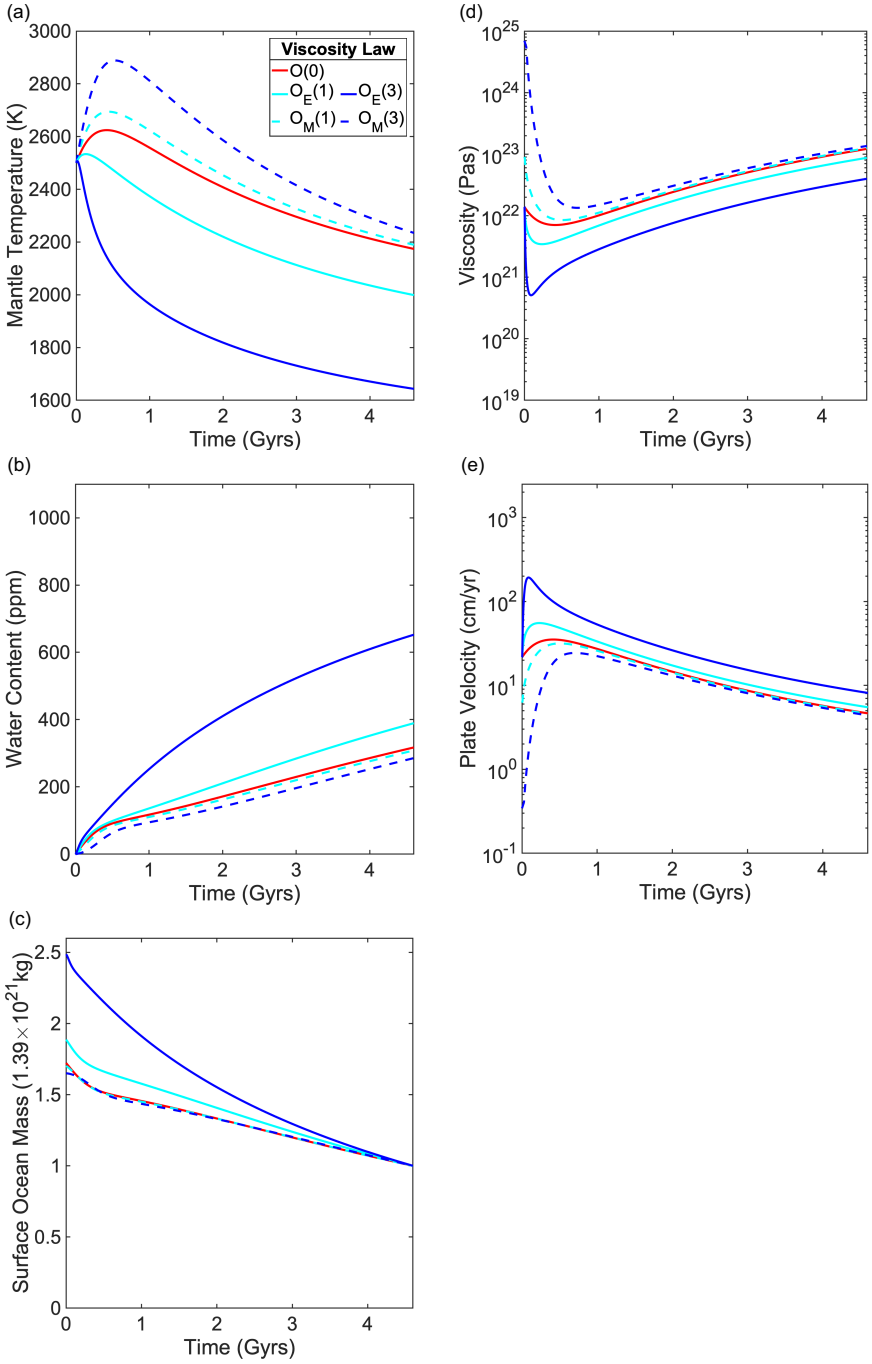

Figure 3.4: The evolution of the viscosity laws defined in Eq. 3.1 and Table 3.1 for when water begins at the surface. The evolution of (a) mantle temperature, (b) mantle water content and (c) surface ocean mass are governed by changes in (d) viscosity and hence (e) plate velocity.

Here, water-dependent model laws have a higher viscosity than water-independent laws, and plate velocities are lower. By 4.6 Gyrs, $O_M\,(1)$ and $O_M\,(3)$ converge with $O\,(0)$ and the plate velocity is $\sim$4.5 cm/yr.

3.3 Effect on Water Cycle

Plate velocity is directly related to the water cycle through regassing at subduction zones (Eq. 2.31) and degassing at MORs (Eq. 2.34). Changes in the plate velocity vary the mass of water subducted and removed from the mantle and their interaction dictates where the water resides over the course of the model.

3.3.1 Water-Independent Law

Figures 3.3d and 3.3e show how the mantle water content and surface ocean evolve for $\eta_0 = 7.53 \times 10^{15}$ Pa s. Two cases are shown where water either begins at the surface or in the mantle interior. The two starting points can be seen in both evolutions, however by $\sim$1.5 Gyrs, the cases converge and cool at the same rate. Whether the mantle begins with water at the surface or in the interior has no effect on the mantle water content at 4.6 Gyrs.

However, it does affect the net transport of water during the beginning of the model. When water begins on the surface, it can be subducted into the mantle. As there is no water in the mantle, none can be degassed. Hence at the start of the model, only regassing operates increasing mantle water content and decreasing the size of the surface ocean. Once $X > 0$, degassing can begin so both regassing and degassing operate for the rest of the model. Degassing never exceeds regassing and the mantle is in a state of net regassing for the entire model.

When water begins in the mantle, both regassing and degassing operate from the start of the model. Degassing is more effective than regassing and the mantle water content decreases. As the water content decreases, degassing also decreases. The decreasing plate velocity slows the transport between the surface and interior reservoirs. This combination causes regassing to exceed degassing for the remainder of the model.

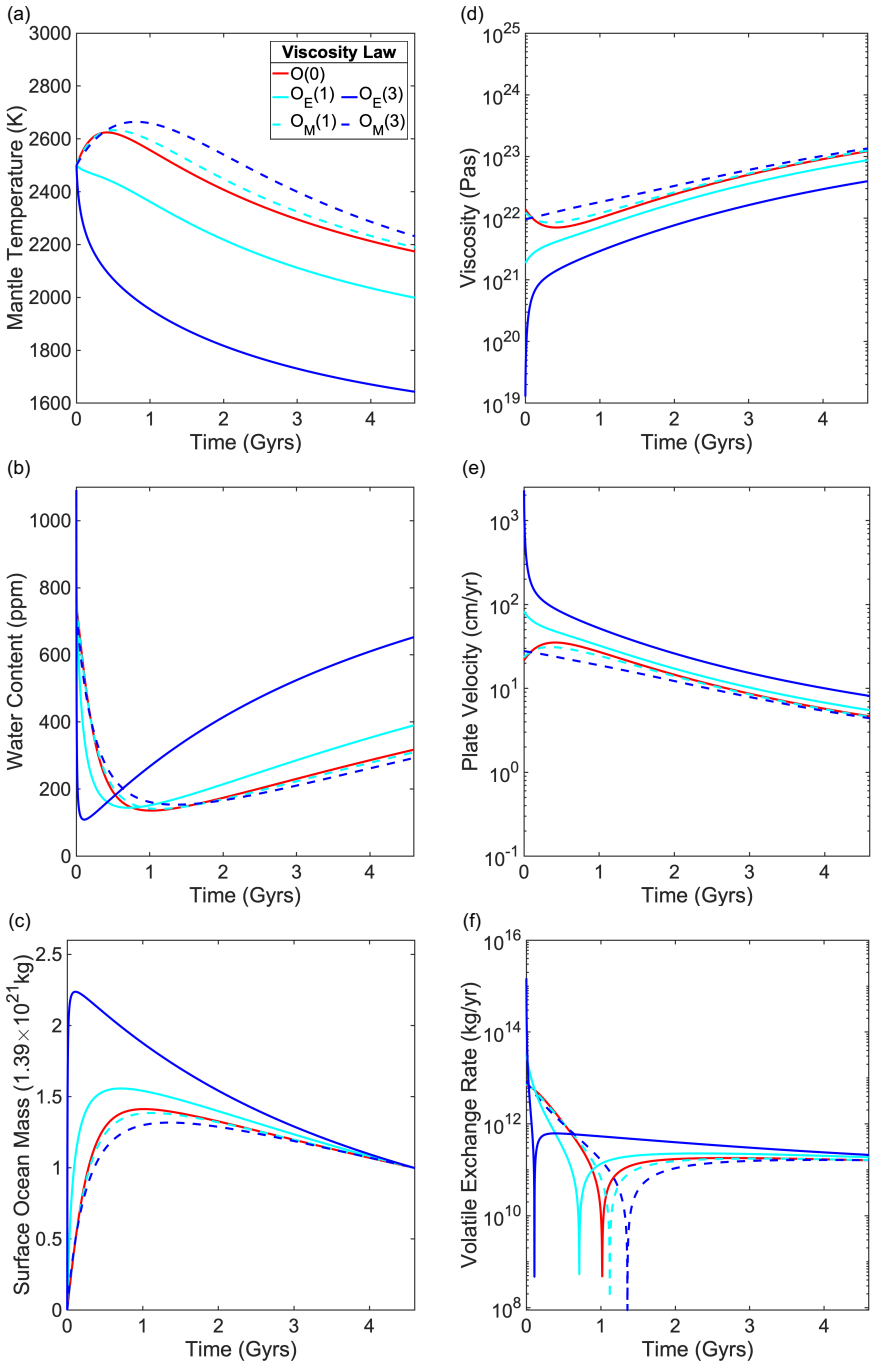

Figure 3.5: The evolution of the viscosity laws defined in Eq. 3.1 and Table 3.1 for when water begins in the mantle interior. The evolution of (a) mantle temperature, (b) mantle water content and (c) surface ocean mass are governed by changes in (d) viscosity and (e) plate velocity. The (f) volatile exchange rate highlights transitions in the water cycle from net degassing to net regassing that appear when water begins in the mantle.

3.3.2 Water-Dependent Laws

Water-dependent viscosity laws create a negative feedback in the water cycle (Williams and Pan, 1992). Water content affects viscosity, influencing Ra and plate velocity. This influences regassing and degassing, hence the water content through the conservation of mass (Figure 2.3).

3.3.2.1 Dry Start

For 'experimental' laws $O_E\,(1)$ and $O_E\,(3)$, starting with an initial temperature of 2500 K and mantle water content 0 ppm give the same starting viscosity of 1.4×10^{22} Pa s (Figure 3.4d). Water is subducted into the mantle but for $O_E\,(1)$ and $O_E\,(3)$ the response in viscosity and hence plate velocity is different. $O_E\,(1)$ sees the mantle water content increasing with a steeper gradient during the first $\sim$0.4 Gyrs than the rest of the model, due to the increasing plate velocity. Once plate velocity begins to decrease, water content increases more slowly. $O_E\,(3)$ increases rapidly due to the maintained low viscosity and hence high plate velocity, allowing water to be rapidly subducted into the mantle. Whilst regassing remains effective, degassing is not due to rapidly decreasing temperature, shallowing melting depth (Eq. 2.35). It is also worth noting that as more water is subducted for $O_E\,(3)$, more water overall is required in the system in order to meet the constraint for one ocean mass at 4.6 Gyrs.

For 'model' type laws, the same starting conditions (2500 K and 0 ppm) do not give the same starting viscosities. Plate velocities of 6 cm/yr and 0.3 cm/yr for $O_M\,(1)$ and $O_M\,(3)$ at the beginning of the model slow the transport of water between the surface and interior. Little water is subducted into the mantle due to these slow velocities and water is effectively degassed due to high temperatures increasing melting depths. This way, mantle water content increases slowly, ending with less than 300 ppm in the mantle.

3.3.2.2 Wet Start

Beginning with water in the mantle shows similar trends in mantle temperature to Figure 3.5a. For 'experimental' laws, starting with water in the mantle gives different starting viscosities. This translates to the highest plate velocity (Figure 3.5e), giving high degassing rates, faster than water is subducted back into the mantle and the water cycle begins in a state of net degassing (Figure 3.5b).

The mantle water content decreases, most rapidly for $O_E\,(3)$, a surface ocean forms (Figure 3.5c). This reduction also decreases the amount of water that can be degassed. The drier mantle increases viscosity, lowering plate velocities and limiting transport between the surface and interior. Hence degassing decreases becoming less than regassing, and the water cycle is in a state of net regassing. As with a dry mantle start, more water is subducted into the interior for $O_E\,(3)$ due to higher plate velocities dictated by lower viscosity throughout the evolution.

For 'model' laws, plate velocities are marginally faster than $O\,(0)$. High water content does not affect viscosity a great deal but does allow degassing to exceed regassing. This decreases mantle water content and viscosity increases. Plate velocities decrease, degassing no longer exceeds regassing and the water cycle is pushed into a state of net regassing. Water content stays lower than for $O\,(0)$ due to higher viscosities and lower plate viscosities limiting transport between the surface and interior.

Beginning with a wet mantle introduces the transition in the water cycle, from net degassing to net regassing. In order to examine this transition more closely, the volatile exchange rate, $|R - D|$, is plotted in Figure 3.5f where the troughs indicate this transition. For 'experimental' laws, the transition occurs earlier than $O\,(0)$ while for 'model' laws the transition occurs later. The timing of the transition is controlled by the viscosity. 'Model' laws reach the highest viscosities and therefore the slowest velocities. This reduces transport between the surface and interior, delaying the switch from net degassing to net regassing. On the other hand, 'experimental' laws cause the lowest viscosities and hence highest plate velocities, increasing transport between the interior and surface.

3.4 Effect on Thermal Evolution

As with the water cycle, thermal evolution can be affected both by temperature and water content of the mantle. Whilst radiogenic heating decreases with time, surface heat flow depends on plate velocity and through this, the various viscosity laws tested result in (sometimes) wildly different thermal evolutions.

3.4.1 Water-Independent Law

For $\eta_0 = 7.53 \times 10^{13}$ Pa s, high plate velocities facilitate high surface heat flow such that $Q_s \gg H$. Rapid cooling characterises the initial stage of the model and as the temperature decreases, viscosity increases. The corresponding drop in plate velocity reduces surface heat flow and the mantle cools more slowly resulting in a mantle temperature of ∼1800 K.

For $\eta_0 = 7.53 \times 10^{14}$ Pa s, higher starting viscosity reduces the plate velocity and hence surface heat flow. The decrease in temperature is more gradual throughout the model, reaching 1950 K by 4.6 Gyrs.

For $\eta_0 = 7.53 \times 10^{15}$ Pa s, higher starting viscosity reduces the plate velocity such that surface heat flow is less than the heat provided by radiogenic heating. $Q_s < H$ and the mantle begins in a state of heating. As the temperature rises, plate velocity increases. This increases surface heat flow until by ∼0.4 Gyrs, $Q_s > H$ and cooling proceeds for the rest of the model. The period of heating slows cooling and mantle temperature is ∼2200 K by 4.6 Gyrs. Whilst all three cases have plate velocities at 4.6 Gyrs within the range observed on Earth today, only $\eta_0 = 7.53 \times 10^{15}$ Pa s matches average mid-mantle conditions expected for today, hence it's comparison in water-dependent models exploring the effects of the water cycle.

3.4.2 Water-Dependent Laws

3.4.2.1 Dry Start

For 'experimental' laws $O_E\,(1)$ and $O_E\,(3)$, starting with an initial temperature of 2500 K, the relatively high starting viscosity means the mantle begins heating. For both 'experimental' laws, lower viscosity due to increasing mantle water content results in higher plate velocity, increasing surface heat flow. This damps heating, shortening the period from 0.42 Gyrs for $O\,(0)$ to 0.13 Gyrs and 0.014 Gyrs for $O_E\,(1)$ and $O_E\,(3)$, respectively. Surface heat flow becomes greater than radiogenic heating and the mantle cools for the rest of the model. Cooling is more pronounced for $O_E\,(3)$ as the higher sensitivity to water content results in faster plate velocities.

$O_M\,(1)$ and $O_M\,(3)$ begin with plate velocities of 6 cm/yr and 0.3 cm/yr. The low plate velocities reduce surface heat flow. High viscosity is maintained due to the

low water content such that heating is more extreme and lasts up to 0.52 Gyrs. As the temperature increases during heating, plate velocities speed up and surface heat flow exceed radiogenic heating ending the temperature increase. After this initial divergence in behaviour, $O\,(0)$, $O_M\,(1)$ and $O_M\,(3)$ cool such that there is little difference in mantle conditions by 4.6 Gyrs.

3.4.2.2 Wet Start

Beginning with water in the mantle shows similar trends in mantle temperature (Figure 3.5a) to starting with a dry mantle. For 'experimental' laws, the lowest viscosity translates to the highest plate velocity (Figure 3.5e). This allows surface heat flow to exceed radiogenic heating and the mantle begins (and continues) in a state of cooling.

For 'model' laws, a much smaller range of initial viscosities does not cause the mantle to begin cooling directly but surface heat flow is reduced and heating is damped. High viscosities keep plate velocities low and this extends heating. However, heating is not as extreme as the dry start start case with temperature reaching less than 2700 K compared with almost 2900 K.

3.5 Discussion

It is clear that the cross-over between water-independent and water-dependent laws affect both the temperature and water cycle evolution. 'Model' type laws show differences early on in their evolution, later converging to the same conditions whilst experimental laws diverge from the outset, resulting in a large range of conditions by 4.6 Gyrs. The convergence in 'model' laws is used as a constraint for present day conditions but effectively allows viscosities higher than $O\,(0)$, in violation of what is expected experimentally. This leads to higher viscosities resulting in delays to features such as heating and the transition from net degassing to net regassing. 'Experimental' laws have the opposite effect as the introduction of water leads to lower viscosities; heating occurs for shorter periods of time and the water cycle transition occurs earlier, due to the higher plate velocities facilitating faster transport between the interior and surface.

Beginning with water in the mantle rather than at the surface has little effect on the temperature evolution and broad trends apply with some dampening.

However, the water cycle exhibits net degassing in the first ∼1 Gyrs, forming a surface ocean with water then being slowly returned to the mantle. This does not affect the conditions post-2 Gyrs, after which is indistinguishable as to whether water began on the surface on in the interior, and will be discussed further in Chapters 4 and 5.

For further comparison to present day conditions on Earth, only experimental laws are considered. Plate velocities for these laws at 4.6 Gyrs all lie in the range of velocities seen today at the Earth's surface 2 cm/yr to 10 cm/yr. The mantle temperature exhibits a much larger range, a result of the differences in plate velocities early on in the model. Water-dependence in $O_E\,(1)$ and $O_E\,(3)$ cause high plate velocities that act to cool the model, bringing temperatures down to 2000 K and 1600 K, respectively. $O\,(0)$ best fits present day mid-mantle temperatures of 2200 K, at ∼2170 K. This model also has implications for the mantle water content at the present day. Cool mantle conditions of $O_E\,(3)$ are associated with a relatively wet mantle of 652 ppm (∼1.5 oceans), compared with 317 ppm (∼0.7 oceans) for $O\,(0)$. Further testing of parameters to assess the water content of the mantle are also discussed in Chapter 5.

These result highlight the importance for understanding the silicate Earth early in planetary evolution. They suggest that during the Hadean and Archean, even if material is recycled by mechanisms other than subduction, cannot be overtly effective as this would have resulted in rapid cooling of the mantle interior. Perhaps this also implies that average mantle viscosities cannot have been particularly low, but if surface recycling was not controlled by subduction as we see it today (e.g. heat-pipe mechanism suggested by Moore and Webb, 2013), it may have been possible for a relatively low viscosities to be maintained within the interior. The viscosity law $O\,(0)$ may best match present day Earth conditions due to it's maintained high viscosity acting as a proxy for spatially dependent changes such as changes in transport mechanism or changes in efficiency for subduction and melting at MORs (Sandu et al., 2011).

It is also evident that high rates of surface recycling (plate tectonics or otherwise) early on in Earth's history would have resulted in cool mantle at the present day. This implies that slow and sluggish convection, and hence average plate velocities comparable to today, is needed to maintain a warm mantle interior. This is already expected due to high mantle temperature changing the nature of subduction, making it less efficient in the past (van Hunen and Moyen, 2012).

3.6 Conclusion

The conditions at which water-independent and water-dependent viscosity laws are calibrated result in two groups of temperature evolution. Laws calibrated to give the same viscosity when there is no water ('experimental') show evolutions in temperature that diverge from each other, whilst laws calibrated at 500 ppm ('model') converge by 4.6 Gyrs. By calibrating at 500 ppm, 'model' laws reach higher viscosities than a water-independent viscosity law, violating evidence presented by experimental data. Hence, in the following chapters only viscosity laws that are calibrated at dry conditions are implemented. With these mineral physics constraints, the water-independent viscosity law is most representative of present day Earth conditions. These initial tests also suggest less than one ocean of water resides in the mantle, further tested in Chapter 5.

3.7 Summary

- Which viscosity law best matches present day estimates for average mantle temperature and plate velocity?
- When comparing temperature- and water-dependent viscosity laws, only those that converge when there is no water present are valid
- A temperature-dependent viscosity law best matches mantle temperature estimates when present day average (mid-mantle) viscosity is 10^{23} Pa s
- Recycling in the early Earth cannot have been overtly efficient as present day mantle would be comparatively cool

4 Mantle Mixing and the Water Cycle

4.1 Introduction

Parametrised models assume the mantle is a homogenous box with subduction bringing water into the mantle and water leaving the mantle at MORs. Any subducted water is instantaneously mixed into the mantle and can immediately be released into the surface reservoir. However, in reality it takes time for water to be transported across the mantle to be degassed at MORs. Due to the effects of water on melting depth and potential effects of water on viscosity, this delay has the potential to greatly influence both the mantle water content and thermal evolution of Earth.

Time delays in dynamical systems have been studied in non-linear optics, population dynamics and physiology (May, 1980; Mackey and Glass, 1977; Niculescu et al., 1998) and have been shown to push systems to instability (Niculescu et al., 1998; Doyne Farmer, 1982). Introduced as a mixing time, a time delay in a convecting mantle may also show this behaviour. A gradually increasing time delay transforms a periodic response to a more complex, multi-component response, leading the system to chaos (Mackey and Glass, 1977; Junges and Gallas, 2012). These studies have shown that the impact on the final state of the system can be dramatic. If these responses are also seen in the water cycle for the solid, convecting Earth, they may effect thermal evolution, water content evolution and sea level via melting and viscosity effects. Therefore, a mixing time is incorporated into the water cycle in order to understand the effects heterogeneity in mantle water content on the thermal evolution.

4.2 Methods

The evolution model is described in Section 2.2 and mixing implementation is outlined in Section 2.3. A water-independent $O(0)$ and water-dependent $O(1)$ viscosity laws are tested (Table 4.1) to understand how mixing may affect the feedbacks in a coupled system. These viscosity laws are based on the 'experimental' type laws defined in Chapter 3.

Instantaneous mixing cases ($\tau = 0$) are calibrated by tuning the initial ocean mass to give 1 ocean (1.39×10^{21} kg) at the present day (4.6 Gyrs) whilst for constant and variable mixing, mantle water content is allowed to evolve freely to assess the effects of mixing on water in both the mantle and surface reservoirs. H_{sf} values in Tables 4.1 and C.1 constrain the surface heat flow from 45 TW to 46 TW at the present day (Section 2.5.1).

A suite of mixing times is examined varying from 0.002 Gyrs to 9 Gyrs, for constant and variable mixing and each viscosity law (Table 4.1). The case where the mixing time is 9 Gyrs is equivalent to only regassing operating; $X\left[\tau_{(Ra)}\right]$ is always zero as no water ever reaches a MOR to be degassed. Running models to 9 Gyrs ensures that any behaviour of the system is captured until it reaches a steady state.

	O (0)	**O (1)**	**Units**
$M_s(t_0)$	1.723	1.887	1.39×10^{21} kg
$T(t_0)$	2500		K
H_{sf}	1.706	1.724	-
η_0	7.53×10^{15}		Pas
r	0	0.3	-
R	8.314		$\mathrm{Jmol^{-1}K^{-1}}$
E	3×10^5		J
F_d	1		-
F_r	0.15		-

Table 4.1: Starting conditions and viscosity constants for instantaneous mixing cases. For both viscosity laws, the mixing times are tested from 0.002 Gyrs to 9 Gyrs on the orders of 0.001 , 0.01 ,0.1 and 1 Gyrs.

4.3 Results

The evolving mantle temperature and mantle water content will increase or decreases depending on which is greater: the input or the output. This defines two states where either the input (H or R) or output (Q_s or D) is dominant. When the input is dominant, the mantle heats and the water cycle is in a state of net regassing, respectively. When the output is dominant, the mantle cools and the water cycle is in a state of net degassing. These results show that the mantle is cooling and net regassing, as has previously been shown (e.g. Crowley et al., 2011; Korenaga et al., 2017; Nakagawa and Spiegelman, 2017) (Figure C.3). However, when mixing is considered, this is shown not be the case.

4.3.1 Water-Independent Viscosity

4.3.1.1 Instantaneous Mixing

Three cases are shown in Figure 4.1, representing behaviour over 9 Gyrs when mixing is instantaneous, constant or variable for $O\left(0\right)$. The instantaneous case is least complex with $\tau = 0$. The mantle begins with a short period of heating to ∼2600 K followed by cooling to ∼2000 K at 9 Gyrs (Figure 4.1a). The water cycle is in a state of net degassing for the entire 9 Gyrs with mantle water content reaching ∼425 ppm by the end of the model (Figure 4.1b). Viscosity is only a function of temperature; as the temperature increases, viscosity decreases and when temperature decreases, viscosity decreases. (Figure 4.1c). Melting depth is a function of both temperature and mantle water content, it's evolution a combination of the increasing and decreasing temperature and the increasing mantle water content. During the first 5 Gyrs, changes in temperature are greater than changes in the mantle water content whilst after 5 Gyrs, changes in mantle water cause the increasing in melting depth. The mantle water content at the ridge (Figure 4.1e) is the same as the average mantle water content (Figure 4.1b).

4.3.1.2 Constant Mixing

With a constant mixing time of $\tau = 1$ Gyrs, the mantle water content and melting depth evolution change dramatically (Figures 4.1b, 4.1d and 4.1e). As the viscosity is only dependent on temperature, the changes are not seen in the thermal evolution or viscosity (Figures 4.1a and 4.1c).

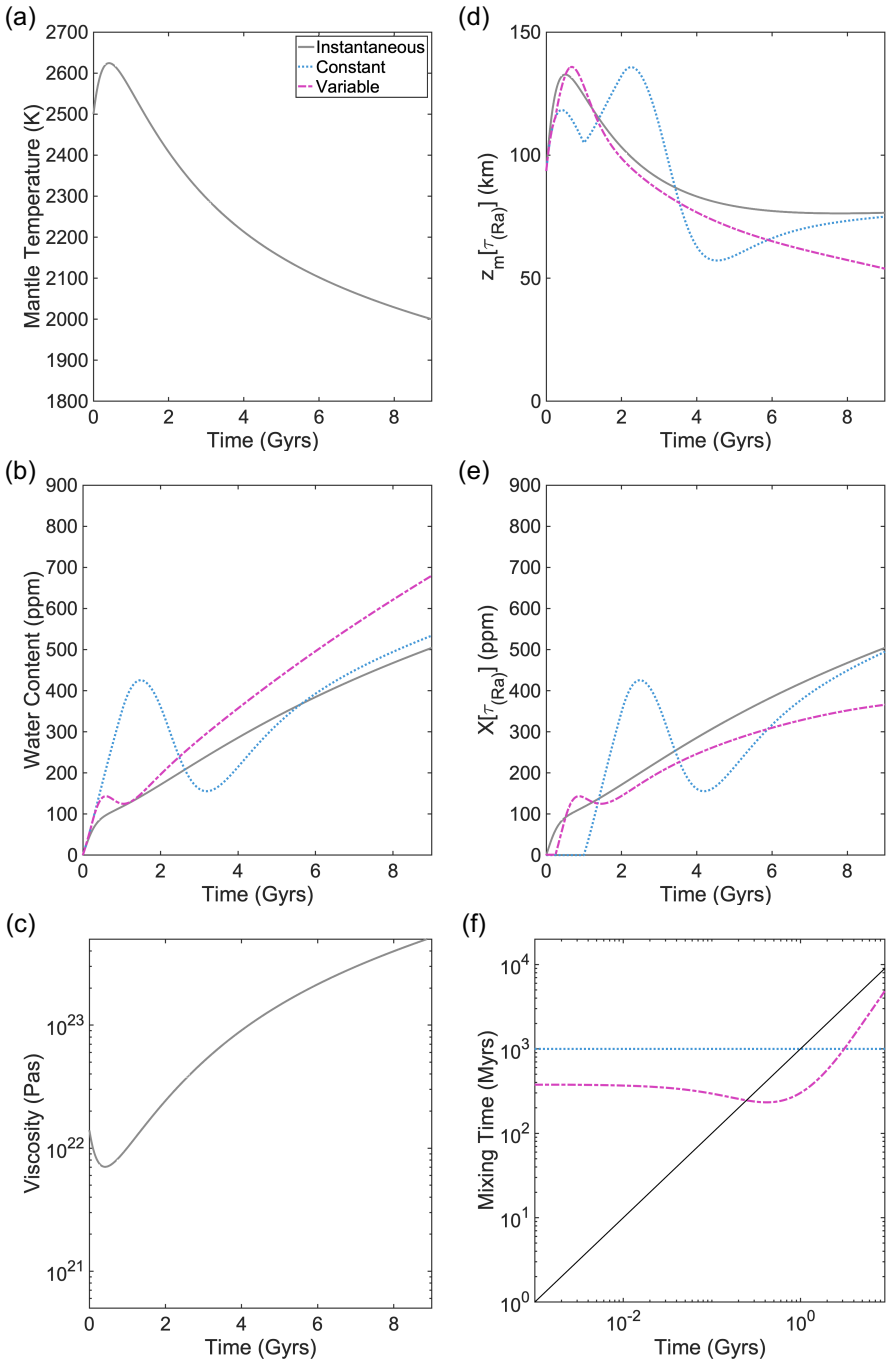

Figure 4.1: Representative cases of a temperature-dependent viscosity law with various mixing implementations, represented by line style. Mixing time $\tau = 1\,\text{Gyrs}$ for both constant mixing and variable mixing (before being scaled by Ra). The panel consist of the resulting (a) mantle temperature T and (b) water content X evolution, (c) viscosity, (d) melting depth, (e) MOR water content at $t_i - \tau_{(Ra)}$ and (f) mixing time. The solid black line in (f) represents the line above which $X\left[\tau_{(Ra)}\right] = 0$ and below $X\left[\tau_{(Ra)}\right] > 0$ as defined in (d).

For the first 1 Gyrs, no water reaches a MORs (i.e. $t < \tau$) and $X[\tau] = 0$. The absence of water in the melting zone means melting depth varies only with temperature during this time and no water is degassed. Only regassing operates and the mantle water content increases during this period of net regassing. Once $t > \tau$, water begins to arrive at the ridge and as $X[\tau] > 0$ (Figure 4.1e), degassing begins by ∼2 Gyrs (Figure 4.1b). The melting depth increases with the introduction of water and the rapid increase of water content in the region pushes the water cycle into a state of net degassing. Mantle water content decreases and together with the decreasing mantle temperature, there is rapid decrease in melting depth. The decreasing mantle water content pushes the water cycle back to a state of net regassing where regassing is the dominant transport mechanism. The MOR water content remains relatively low when compared with the whole mantle average resulting in less water being degassing for the remaining time and more water remains in the mantle. As the local mantle water content increases over the last 4 Gyrs, melting depth also increases (Figure 4.1d).

4.3.1.3 Variable Mixing

When mixing is scaled by the convective vigour Ra (and $m = 2/3$), the transitions in the water cycle present for constant mixing are damped, more comparable to the instantaneous mixing case. This is the result of the variable mixing time τ_{Ra} (Figure4.1f). As function of viscosity through Ra, earlier times of lower viscosity and high convective vigour result in short τ_{Ra}. This causes the time for which $X[\tau_{Ra}] = 0$ to become shorter at the beginning of the model. For a cooling mantle, the decrease in convective vigour increases τ_{Ra}.

This can be examined in Figure 4.1f, where the black line denotes $t = \tau_{Ra}$. For constant mixing, there is no change in τ. For variable mixing, τ_{Ra} begins with a smaller mixing time than the constant case and τ_{Ra} then spends less time above the line where $X[\tau_{Ra}] = 0$. This means the period where only regassing operates is shorter and less water is regassed. This causes the later responses in degassing to be less extreme and hence the period of net degassing is limited in both time and amplitude. As the mixing time increases, it takes longer for subducted water to reach the MOR and therefore less is degassing. This results in more water in the mantle than either the instantaneous or constant mixing case.

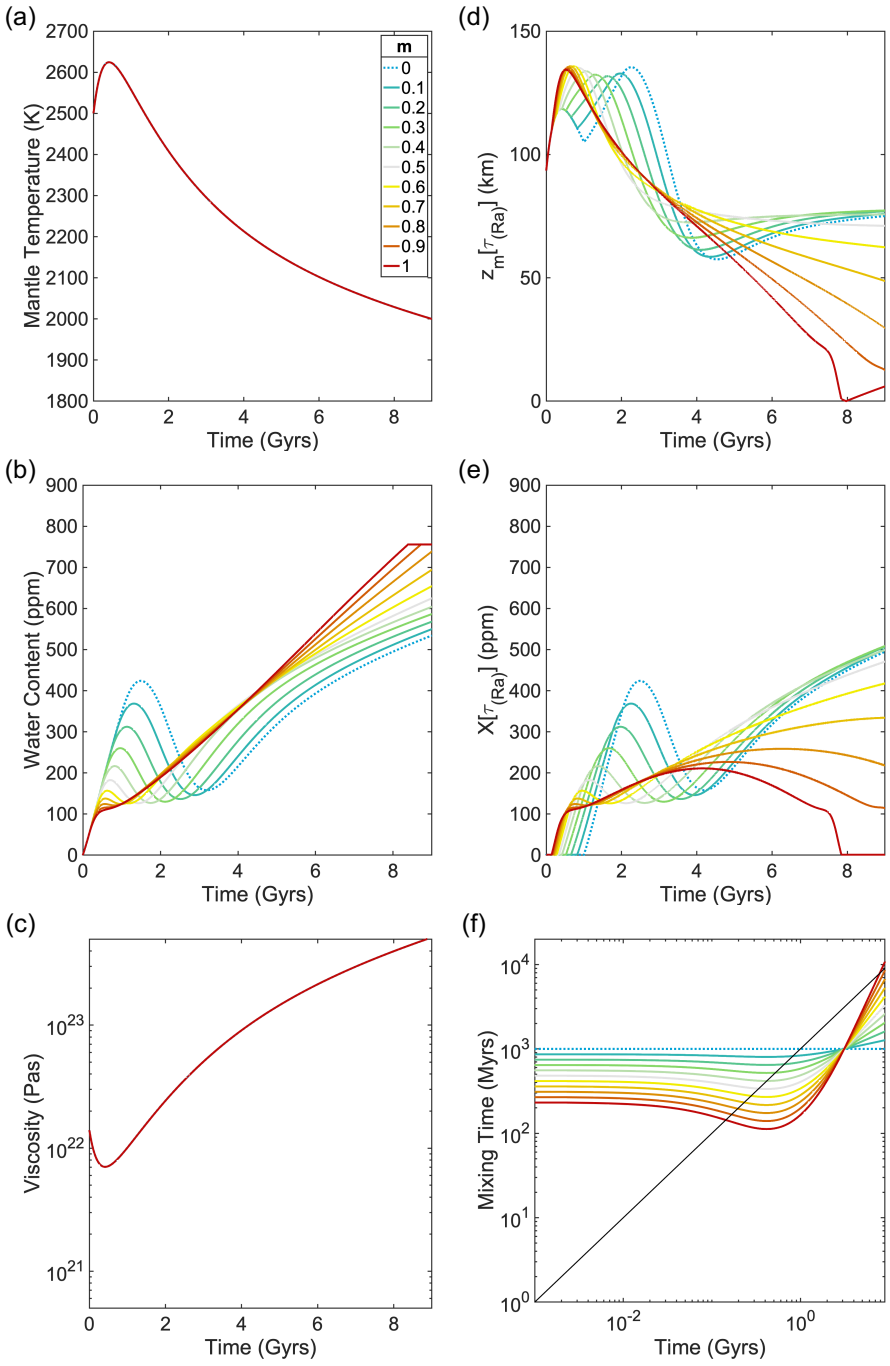

Figure 4.2: Variation in evolution due to changing m-exponent in the variable mixing time relationship of Eq. 10. (a) average mantle temperature, (b) average mantle water content, (c) average mantle viscosity, (d) melting depth, (e) local water content at MOR and (f) mixing time. $m = 0$ (dashed orange) represents the constant mixing case also presented in Figure 4.1 and dark blue represents $m = 1$.

4.3.1.4 Influence of Mixing Time Scaling

Variable mixing is also a function of the exponent m (Eq. 2.40). Figure 4.2 shows how the evolution changes when m is varied from 0 to 1. As with Figure 2.40, the temperature (Figure 4.2a) and viscosity (Figure 4.2c) are the same for each case. $m = 0$ is is equivalent to a constant mixing time and when m is increased, the initial τ_{Ra} at the beginning of the model decreases (Figure 4.2f) τ_{Ra} from 1 Gyrs for $m = 0$ to 0.23 Gyrs for $m = 1$. This reduces the time where only regassing operates restricting the period of net degassing until $m = 0.8$ where there is no period of net degassing. This implies that the more coupled the mixing of water is to convection (i.e. the more tracer-like), the more likely water is to become trapped in the mantle. Smaller values for m only weakly couple τ_{Ra} and Ra allowing up to 425 ppm of water to build up in the mantle for the initial period of net regassing. The corresponding, induced net degassing lasts from 1.5 Gyrs to 3.2 Gyrs. These cases may thus be divided into two sets: cases where mixing time is weakly dependent on Ra ($m < 0.8$) with a period of net degassing and cases where mixing time is strongly dependent on Ra ($m \geq 0.8$) where there is no net degassing.

4.3.2 Water-Dependent Viscosity

4.3.2.1 Instantaneous Mixing

Figure 4.3 shows cases as in Figure 4.1 but with a water-dependent viscosity law. For instantaneous mixing where $\tau = 0$, the mantle begins with a short period of heating ($\sim$0.15 Gyrs) to $\sim$2550 K followed by cooling to $\sim$1850 K at 9 Gyrs (Figure 4.3a). The mantle only experiences net regassing, increasing water mantle content to $\sim$600 ppm by 9 Gyrs (Figure 4.3b). Both viscosity and melting depth evolve with temperature and water content. Increasing temperature and water content during heating result in a decrease in viscosity (Figure 4.3c) and increase in melting depth (Figure 4.3d). The decrease in viscosity allows surface heat flow to increase until it becomes greater than radiogenic heating and the mantle cools. The decreasing temperature increases viscosity whilst the increasing water content leads to an increase in degassing and a slow increase in melting depth.

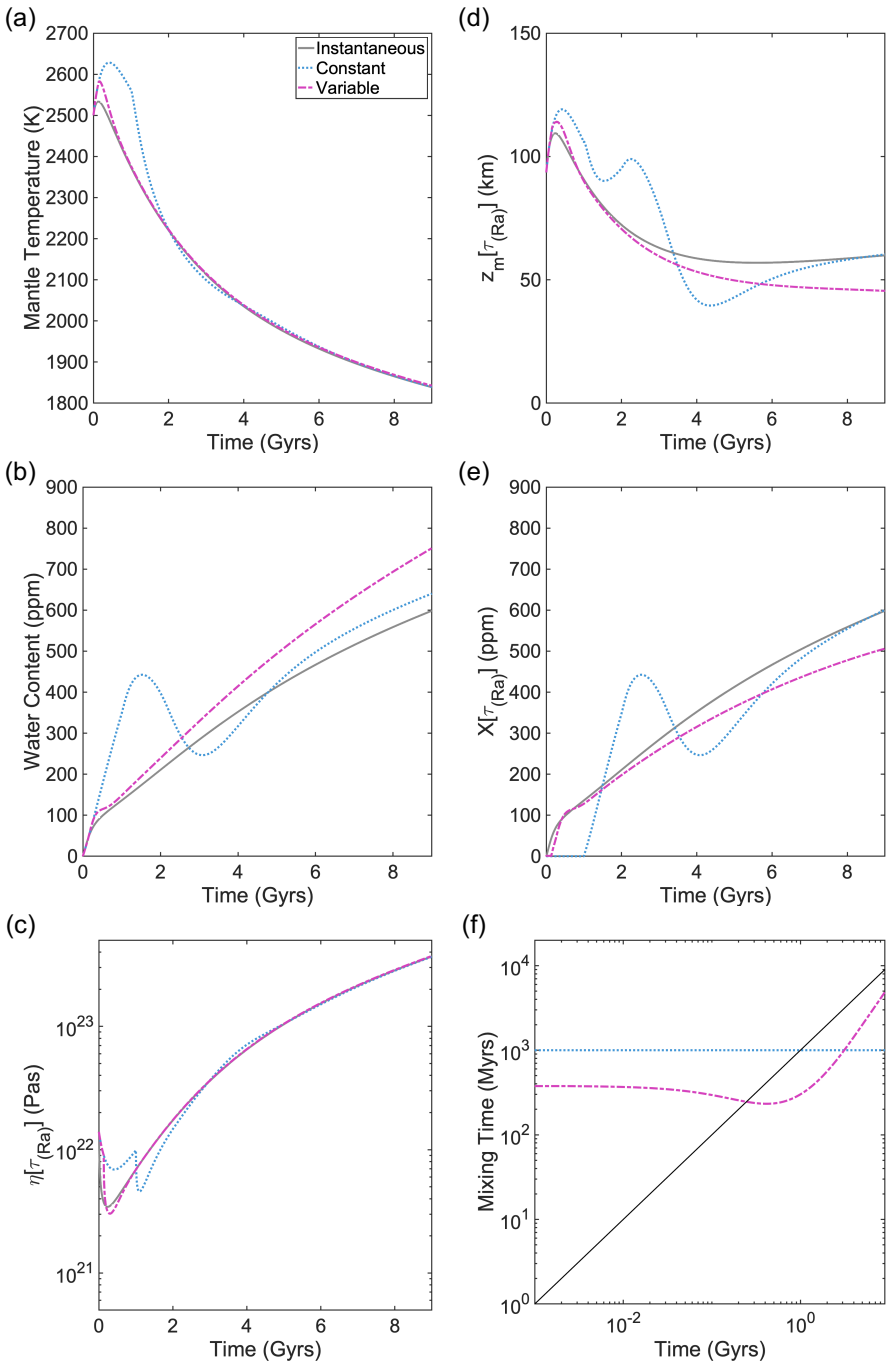

Figure 4.3: Representative cases of a water-dependent viscosity with various mixing implementations where $\tau = 1\,\text{Gyrs}$ for both constant mixing and variable mixing (before being scaled by Ra). (a) is average mantle temperature and (b) is average mantle water content. When mixing is instantaneous, (c) represents the average mantle viscosity and when mixing is included (constant or variable), (c) represents the local viscosity at the MOR. (d) is the melting depth, (e) is local water content at the MOR and (f) is the mixing time.

4.3.2.2 Constant Mixing

Constant mixing in the presence of $O(1)$ is similar to Figure 4.1 with additional feedback to the thermal evolution and viscosity before 4 Gyrs (Figures 4.3a and 4.3c). The fluctuations in water content and melting depth are damped with initial net regassing leading to 443 ppm by 1.5 Gyrs (Figure 4.1b).

When $X[\tau] = 0$, the local (MOR) viscosity (Figure 4.1c), melting depth (Figure 4.1c) and surface heat flow are only a function of temperature. As the material in the melt zone is still dry, MOR viscosity is high and the surface heat flow is low, relative to the instantaneous case. This allows a more pronounced period of heating to develop. As the temperature increases, viscosity decreases increasing surface heat flow. This decreases temperature and the thermal evolution is in a state of cooling for the remainder of the model.

As the water content at the ridge begins to increase after 1 Gyrs, this decreases viscosity and facilitates a period of rapid cooling. Competing increases in water content and decreases in temperature form a local maximum in the melting depth (Figure 4.3d). The increase in local water content at the MOR induces net degassing (Section 4.3.1.2).

With both temperature and water content decreasing at $\sim$2.5 Gyrs, there is a rapid decrease in the melting depth. This decrease also reduces degassing, pushing the system back into a state of net regassing.

4.3.2.3 Variable Mixing

Variable mixing and $O(1)$ also closely resembles the instantaneous mixing case (Figure 4.1), a result of shorter mixing times at the beginning of the model. However, even a small period of net degassing is no longer observed. Instead, there is a short period of approximately constant water content for 0.2 Gyrs suggesting that both variable mixing and $O(1)$ damp the effects seen for constant mixing. Both melting depth and viscosity are more comparable to instantaneous mixing but as τ_{Ra} increases trapping more water in the mantle, less water reaches the MOR (Figure 4.3e). This results in a relatively shallow melting depth (Figure 4.3d) and higher mantle water content (Figure 4.3b).

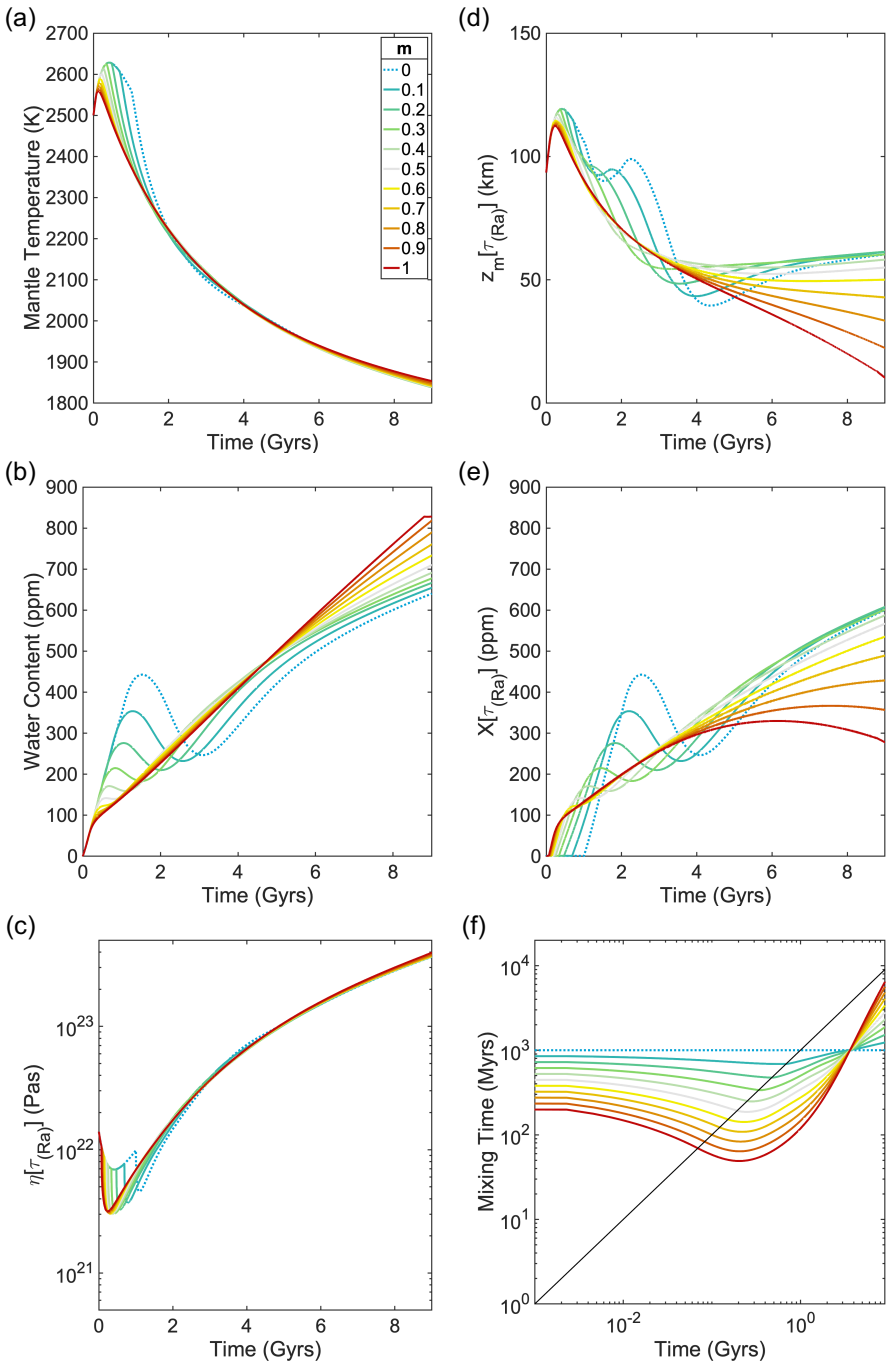

Figure 4.4: Variation in evolution due to changing m-exponent in the variable mixing time relationship for a water-dependent viscosity. $m = 0$ represents the constant mixing case in Figure 4.3.

4.3.2.4 Influence of Mixing Time Scaling

As with $O\,(0)$, increasing m from 0 to 1 increases the coupling to convective vigour. This shortens the period where $X\,[\tau_{Ra}] = 0$ to 0.2 Gyrs, reducing the amount of water subducting during initial net regassing. Varying m results in less water at the MOR to later influence degassing, preventing large periods of net degassing occurring. Net degassing is only induced for $m \leq 0.5$ implying that if the initial τ_{Ra} is varied by less than an order of magnitude, net degassing will occur. The feedback to thermal evolution and viscosity is also evident in Figures 4.4a and 4.4c, although the water-dependent viscosity damps the fluctuations of Figure 4.2.

In short, a period of net degassing is induced when mixing is constant (τ =1 Gyrs and $m = 0$) whilst both variable mixing and a water-dependent viscosity act to damp these oscillations. Constant mixing assumes a finite transit time for water to arrive at a MOR after being subducted past the arc front. Net regassing dominates, allowing water to build up in the mantle after which net degassing is induced to bring the mantle back to a steady state evolution. When mixing is strongly coupled to the convective vigour, high mantle temperatures (and increasing mantle water content) ensure τ_{Ra} is short for much of Earth history, making variable mixing cases more comparable to instantaneous mixing cases.

Deviations in $X\,[\tau_{Ra}]$ ensure the mantle water content evolutions diverge whereas thermal evolutions converge by 9 Gyrs (Figures 4.2 and 4.4). As with previous models, this makes cases at the present day indistinguishable from each other. During the early Earth, changes in temperature, water content and hence Ra are rapid facilitating oscillations in both thermal and water content evolution. Evolution is particularly sensitive to the initial mixing time at the beginning of the model, leading to up an ocean of water being subducted into the mantle in less than 2 Gyrs, highlighting the sensitivity of initial mantle conditions in order to understand evolution on the planetary scale.

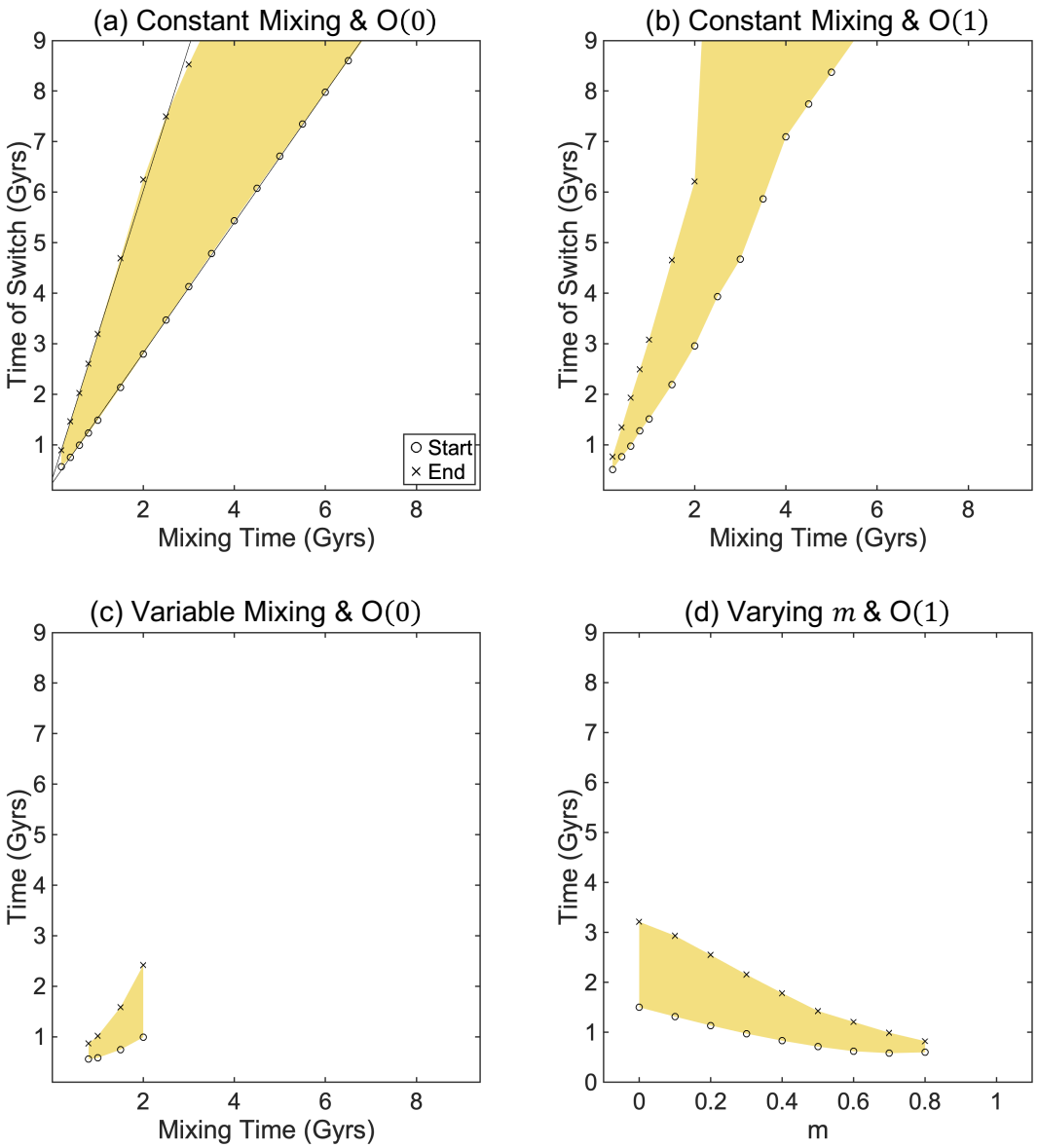

Figure 4.5: The start (black diamonds) and end (magenta diamonds) of periods of net degassing for constant mixing, variable mixing, and both viscosity laws, for τ varying between 0.002 and 9 Gyrs (a, b and c), and for different values of m (d). The y-axis corresponds to the x-axis in Figures 4.1 to 4.4 for (a), (b) and (c). Where there are no points, no net degassing period occurs. A linear trend is fitted to $\tau_{(Ra)} < 2$ Gyrs in (a). Shaded regions corresponds to net degassing.

4.4 Discussion

4.4.1 Net Degassing

Present day estimates for the mixing time vary from a few 100 Myrs to 4 Gyrs (Kellogg and Stewart, 1991; Samuel et al., 2011; Tackley, 2015) and varying τ will change the timings of the transitions between net degassing and net regassing seen in Section 4.3. The inclusion of a mixing time causes the water cycle to experience three phases: (1) $X\left[\tau_{(Ra)}\right] = 0$ causes rapid net regassing, (2) $X\left[\tau_{(Ra)}\right] > 0$ inducing net degassing and ending in (3) net regassing. These three phases define two transitions at the start and end of the period of net degassing in the mantle water content evolution X.

These points are plotted in Figure 4.5 for a range of τ from 0.002 Gyrs to 9 Gyrs, for constant and variable ($m = 2/3$) mixing and water-independent and water-dependent viscosity laws. Where there are no (turning) points, no period of net degassing occurs. Constant mixing and $O(0)$ across this range of τ in Figure 4.5a show that net degassing does not occur when $\tau < 0.2$ Gyrs. For these cases, τ is small enough that it's evolution behaves almost exactly as the instantaneous mixing case. When net degassing is induced, increasing τ delays the start of net degassing and extends the period so that it ends at a later time. The starting points fall on a straight line as the start of net degassing is controlled by the period where $X[\tau]$ is zero i.e. is defined by τ. The end of the period is linear only until τ =2.5 Gyrs, after which the end points deviate from this trend.

Constant mixing and $O(1)$ in Figure 4.5b shows a region of net degassing similar to Figure 4.5a. However, net degassing begins later and ends earlier, resulting in a shorter period of net degassing. The feedback caused by $O(1)$ influences the thermal evolution and the surface heat flow is scaled to ensure 45 TW to 46 TW condition is met at the present day (Table C.1), also shortening the net degassing period.

Variable mixing massively restricts the occurrence of net degassing. For $O(0)$, net degassing only occurs for $\tau = 0.8$ Gyrs to 2 Gyrs lasting from ∼0.3 Gyrs to 1.4 Gyrs whereas for constant mixing net degassing lasts ∼1.4 Gyrs to 3.5 Gyrs for these values of τ. Net degassing also begins earlier for $\tau = 0.8$ Gyrs to 2 Gyrs at ∼0.6 Gyrs to 1 Gyrs for variable mixing compared with ∼1.2 Gyrs to 3 Gyrs for constant mixing.

When both variable mixing and $O(1)$ are considered, no period of net degassing

occurs. At the beginning of the evolution, both mantle temperature and mantle water content are increasing. This acts to decrease viscosity, increasing Ra and decreasing τ_{Ra} (Eq. 2.40). The short τ_{Ra} results in an evolution similar to the instantaneous mixing case, with a few cases showing only small deviations. For $\tau = 1\,\text{Gyrs}$ to $2\,\text{Gyrs}$, net degassing is damped such that short periods of approximately constant water content or slower increases water content are seen, similar to Figure 4.3b. From Figures 4.5a, b and c, both variable mixing and a water-dependent viscosity restrict the occurrence of net degassing. These results demonstrate how the existence and duration of a period of degassing is very sensitive to both the mantle viscosity and the estimates of the mantle mixing time.

Variable mixing is dependent on both τ and the exponent m. If instead τ is kept constant and m is varied (Figure 4.5d), the duration of net degassing is seen to decrease as m increases (Figure 4.4). This decreases τ_{Ra} and therefore less time is spent where $X\left[\tau_{Ra}\right]$ is zero where only regassing operates. Less water is subducted and once this reaches a MOR, the influence on degassing is limited and regassing remains the dominant transport process. As m increases, mixing is more coupled to the mantle causing net degassing to begin earlier for a shorter period.

Variations in τ and m highlight the importance of initial conditions. The first few hundred million years ($X\left[\tau_{(Ra)}\right] = 0$) are the main control on water content evolution prior to $\sim$4 Gyrs, as result of the initial mixing conditions. Therefore, models to test an initially wet mantle with no water on the surface are shown in Figure C.1 and Figure C.2. There is an additional period of net degassing before the three stages described at the beginning of this section. This short, rapid net degassing period releases all the water to the surface, drying the mantle. The evolution after this is followed by the net regassing-net degassing-net regassing cycle previously discussed, suggesting that net degassing may occur regardless of the initial mixing conditions.

Values of degassing efficiency will also effect the period of net degassing. Whilst the F_d values are unclear (Section 1.5.1), the value assumed here is the most efficient (Crowley et al., 2011; Rüpke et al., 2013). F_d is varied between 0 and 1 (Figure C.5) showing that while transition times remain unaffected, amplitude is reduced when $F_d < 1$. Net degassing does not occur for values less than 0.4.

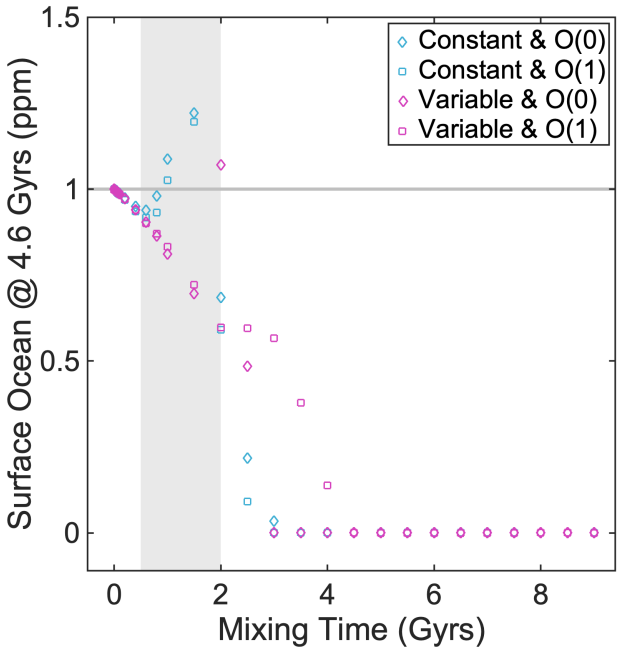

Figure 4.6: Number of surface oceans at 4.6 Gyrs in each of the models in Figure 4.5, normalised by Earth's present day ocean mass . The light grey shaded region corresponds to 0.5 Gyrs to 2 Gyrs mixing time estimates from geochemistry and the dark grey line is equivalent to one ocean mass (∼439 ppm).

4.4.2 Surface Ocean

Thus far, only mantle water content evolution has been examined. This inevitably has an effect on the surface ocean. For cases examining the effect of τ for constant mixing, variable mixing, $O\,(0)$ and $O\,(1)$ (Figure 4.5), the surface ocean mass at 4.6 Gyrs is extracted and collated in Figure 4.6. As τ increases, the surface ocean mass decreases. For τ<4 Gyrs, most cases result in less than the expected 1 ocean at the surface. For τ>4 Gyrs, the surface ocean mass is zero as all water has been returned to the mantle interior.

However, there are some cases between 0.5 Gyrs and 4 Gyrs resulting in more water in the surface ocean than in the interior. This is a result of the mantle water content evolution being in a state of net degassing or soon after the period has finished. During net degassing, the net movement of water is toward the surface and the decrease in mantle water content is tied to an increase in increase in surface ocean mass. Soon after the period of net degassing, not enough water has been returned to the mantle by 4.6 Gyrs and more water is therefore expected at the surface.

In particular, cases with constant mixing (circles in Figure 4.6) show higher surface ocean volumes. This is due to the sustained periods of net degassing where more water is driven to the surface from the mantle interior. Net degassing is less likely to occur for variable mixing and $O(1)$ cases and hence more water is subducted into the mantle. Figure 4.6 clearly indicates that the inclusion of mixing into a parametrised model can result in variations in ocean mass of up to 1 ocean. Unless the mantle has experienced a sustained period of net degassing, increasing the mixing time decreases the surface ocean mass.

4.4.3 Implications of Mixing for Earth

Considering mixing in the deep water cycle has show that Earth may transition between periods of net degassing and net regassing over it's lifetime. Mixing traps water in the mantle either for a constant or variable amount of time. As the mantle cools, the mixing time increases and the mantle is able to trap water for longer, later in the evolution. This means that it takes longer for water to reach a MOR where often mixing time is longer than the age of the Earth. This means that any water subducted during this time would never enter the melt region and be released (overturn in Figure 4.2 and Figure 4.4). Net regassing is the dominant state agreeing with previous works (e.g. Korenaga et al., 2017; Nakagawa and Spiegelman, 2017) whereas unlike previous parametrised models, the mantle is initially assumed dry (Section 2.5.2 and Chapter 3 for more discussion). Variable mixing cases are in agreements with previous studies where the mantle is both hotter and drier in times corresponding to the Archean ($\sim$0.5 Gyrs to 2 Gyrs). As the mantle cools towards the present day and mixing time increases, water is less likely to be degassed.

The effects of mixing are most prominent for cases with a constant mixing time and water-independent viscosity where water has no appreciable affect during evolution. This could either be a result of only small amounts of water in the system being unable to create large changes in viscosity (Muir and Brodholt, 2018) or there being little to no water in the mantle over the course of evolution. However, the effects of water on the melting depth are primary, driving the transitions in the water cycle regardless of the viscosity law. This is due to the direct relationship between $X\left[\tau_{(Ra)}\right]$ i.e. the water content at the ridge and D (Eq. 2.34), inducing periods of net degassing.

Comparisons with present day mixing estimates 0.5 Gyrs to 2 Gyrs (Gonnermann

and Mukhopadhyay, 2009), and the surface ocean mass (Figure 4.6) show only a few cases are close to agree with both. No cases have both $O(1)$ and a variable mixing time but there are three cases closest to this range; $tau = 0.8$ Gyrs where mixing is constant and $O(0)$, $\tau = 1$ Gyrs where mixing is variable and $\eta(T)$ and $\tau = 2$ Gyrs where mixing is constant and $O(1)$. Choosing which of these cases is most like Earth is not clear but the mixing time cannot be greater than 2 Gyrs as too much water would be trapped in the mantle and there would not be enough water at the surface, uncovering too much of the surface to the atmosphere. The longer mixing times discussed previously are a result of understanding geochemical tracers (Section 1.8). However, compared with water, their potential for feedback into the convecting system is limited. Water reduces density, viscosity and increases the melting depth, actively participating in various aspects of mantle convection. The relatively short mixing times in this Chapter may be more reflective of this, perhaps more comparable to short residence times, where the low mantle water capacity of the lower mantle may force water to reside in the upper portions of the mantle. The mixing time is also likely to have varied over Earth's evolution but how is still uncertain. If surface mobility was comparable to today in some form of plate tectonics, estimates for the Hadean can be of the order $\sim$0.1 Gyrs (e.g. Samuel et al., 2011; Kellogg and Stewart, 1991) whereas stagnant lid geodynamic models suggest mixing times $\sim$1 Gyrs.

It is difficult to suggest which cases in Section 4.3 are most applicable for Earth. However, even with the uncertainty surrounding mixing style (constant or variable) and viscosity law (water-independent or water-dependent and Section 1.6), it is apparent that the most significant effects may arise from the interaction of water and the melting depth. Melting depth in conjunction with mixing is considered to be more important than mixing and the viscosity law when considering evolution on the geological timescale.

Earth can also be considered as a dynamic system and the mixing effects compared in this way. The Earth behaves as a first order system when mixing is instantaneous with mantle temperature decreasing with radiogenic decay (Figure 4.3a). The temperature evolution experiences fluctuations when mixing is constant (Figure 4.3a), comparable to the behaviour in experimental time delay systems of Callender et al. (1936). However, the fluctuations are damped when the mixing time is scaled with Ra and is allowed to evolve accordingly. Figure 4.4a highlights this effect for values of $m \gtrsim 0.2$, consistent with previous work where complex dynamics and chaos occur when the time-delay is of a similar or-

der to the characteristic response time of the system (Junges and Gallas, 2012). The evolution timescale of mantle temperature has primarily been controlled by radiogenic elements, hence evolution is controlled by the half lives of these elements that lie in the range from 1 Gyrs to 10 Gyrs (Table 2.1) (Junges and Gallas, 2012). Chaotic behaviour is most likely when the mixing time is approximately the same as the radiogenic half lives (i.e. $\tau_{Ra} \geq$1 Gyrs). This requires the mantle to have cooled somewhat in order to reduce initially short τ_{Ra} , and fluctuations are no longer expected due to the decreasing temperature and mantle water content. This shows that the mixing time will have a minimal effect in the long term as the system behaves in a quasi-steady state regime. But early on in the evolution, fluctuations have been shown to be prominent where mixing times are more comparable to to radiogenic timescales.

As result of the lag between regassing at subduction zones and degassing at MORs, these fluctuations will also effect the surface reservoir (Figure 4.6). The relationship between surface ocean mass and sea level are examined and applied in detail in Chapter 5 and discussed briefly here. Changes of $\sim$1 ppm would increase (or decrease) sea level by $\sim$10 m suggesting that even small changes in surface oceans would have a large impact on the exposure of sub-aerial land. Variations of this order and higher are seen to occur on the 100 Myr and 1 Gyr timescales in Figure 4.6b. For comparison, global mean sea level is rising $\sim$3 mm/yr (Watson et al., 2015) whilst the largest changes in these models would suggest variations on the order of $\sim 10^{-3}$ mm/yr, indicating that long term mantle related signals would be lost in short term climatic changes. When mixing times are $<$1 Gyrs, surface ocean mass varies up to 0.1 oceans, sea level would still vary by $\sim$400 m, flooding considerable areas of the current sub-aerial land. The first phase of net regassing removes $\sim$1 ocean from the surface. Less than 1 ocean would remain at the surface, potentially uncovering highs such as MORs to the atmosphere. This period of net regassing can last $\sim$1 Gyrs exposing highs to sub-aerial weathering, a process important in forming continental crust (Höning et al., 2014). This timing could overlap with the onset plate tectonics, considered to be $\sim$2.5 Ga or earlier, if water can be transported efficiently into the mantle during this time.

When considering the deep water cycle, sea level is an ideal constraint from geological data (e.g. Korenaga et al., 2017), often overlooked. Karlsen et al. (2019) show that by considering mantle contributions to sea level since the end of Pangea, ocean mass has declined toward the present day. Modelling that extends this work to consider multiple supercontinent cycles may also show delays

between period of rapid subduction and supercontinent break-up in response to melting of relatively hydrated material. Understanding the process during the early parts of Earth's evolution can only be accessed with more indirect tools. One transition between net degassing and net regassing has been shown by Parai and Mukhopadhyay (2018), examining atmospheric xenon isotopes. Work such as this may uncover more periods in Earth history where such transitions have occurred. The tectonic regimes the Earth has experienced would also need to be considered. In particular, for the early Earth where the regime is still unclear, different mechanisms have been proposed (e.g. Sleep et al., 2014) such as heat pipe (Moore and Webb, 2013) and 'squishy lid' tectonics (Lourenço et al., 2018). Net degassing is also seen in the results of 2D (Nakagawa and Nakakuki, 2019) and 3D (Price et al., 2019) models. Multiple transitions are seen on the order of 100 Myrs in 2D models whereas in 3D, time between transitions are 500 Myrs. Corresponding changes in surface ocean mass of ∼130 ppm translate to changes in sea level of a kilometre. Further dimensional models investigating these changes are required to aid the understanding of mixing and it's impact on the surface ocean.

4.5 Conclusion

Mixing is included in a parametrised model that solves for the evolution of average mantle temperature and average mantle water content. A time delay is implemented in the water cycle such that any water subducted past the arc front takes a mixing time $\tau_{(Ra)}$ to arrive at the MOR. This requires the tracking of both the whole mantle average water content and the water content at the MOR. This results in the degassing process being controlled by the local water content which can induce a period of net degassing. This local water content has a larger effect on the degassing and hence the evolution of the water cycle, than the indirect effects from a water-dependent viscosity. Any mixing times larger than ∼4 Gyrs transport all the water to the mantle, leaving a dry surface. Lastly, as small variations in surface ocean mass can lead to large variations in sea level, the development of subduction as an efficient transport mechanism of water may have removed water from the surface ocean, reducing sea level and aiding sub-aerial weathering in the early Earth.

4.6 Summary

- Parametrised models inherently assume that mixing in the mantle is instantaneous and water would be homogeneously distributed
- How does mixing effect the water cycle and thermal evolution of the mantle?
- Mixing traps water in the mantle
- A period of net degassing can also be induced
- Once subduction became a viable water transport mechanism to the mantle, the size of the surface ocean could be reduced potentially aiding sub-aerial weathering

5 No Oceans in the Mantle?

5.1 Introduction

In the early Earth, higher mantle temperatures would reduce mineral capacity for water (Section 1.3). For example, an increase of 600 K can reduce wadsleyite and ringwoodite capacity by an order of magnitude from 10 000 ppm to 1000 ppm (Litasov and Ohtani, 2003; Ohtani et al., 2000). If a further 600 K increase in temperature results in the reduction of capacity by another order of magnitude, this implies that the capacity for transition zone minerals close to the solidus (Zerr et al., 1998; Hirschmann, 2000) would be ∼100 ppm. If the same reasoning is applied to other mantle minerals, their capacity would be <1 ppm. This implies that just after the mantle has solidified, the whole mantle capacity would be < 0.1 oceans.

Over time as the Earth cools, the solubility of water increases considerably and an important question is how much water is in the mantle now? While Earth has one ocean of water at the surface today, the amount of water in the mantle is currently debated. Evidence from OIBs suggest that the mantle may contain up to 2 oceans, hydrous transition zone mineral imply ~ 4 oceans, and geochemical arguments suggest almost an order of magnitude larger, up to ~ 14 oceans, (Sections 1.3 and 1.4). It is commonly cited in the literature that many oceans worth of water reside in the mantle, from geochemical (Marty, 2012a), geodynamic (e.g. Nakagawa and Iwamori, 2017) and mineral physics arguments (Fei et al., 2017). However, previous convection models considering the water cycle are often restricted to the mantle interior and how much water is subducted, neglecting the effects on the surface ocean. Subduction of multiple oceans would vary sea level on the order of kilometres over Earth history, implying that much, if not all, of today's topography would be flooded. This is an important constraint ignored in most previous studies.

For example, 5 oceans (4 oceans in the mantle and 1 ocean at the surface) would

result in an ocean 11 km deep. In the Hadean, zircon evidence indicates the presence of surface water at 4.1 Ga (Trail et al., 2018) but not the depth of the ocean. The earliest tracers of ocean depth are sandstones from 3.5 Ga that show evidence of deltas, indicating that some crust must have been sub-aerial at this time (DiMarco and Lowe, 1989). Recent analysis of triple-oxygen isotopes shows that sub-aerial continental crust supported a modern hydrological cycle at 2.5 Ga (Bindeman et al., 2018). This crustal exposure suggests that ocean volumes and sea level from 1-2 billion years after Earth formed cannot have been wildly different as to those seen today, and excess ocean volumes must have been subducted by this time.

In this chapter, I examine whether several oceans of water in the mantle is compatible with geological constraints.

5.2 Methods

In order to test which cases lead to a scenario that best fits conditions expected at the surface, the evolution model in Section 2.2 is used with the water-independent viscosity law presented in Chapter 3, most representative of Earth's evolution. As in previous chapters, the temperature and mantle water content evolution are calculated by solving Eq. 2.26 and Eq. 2.29, respectively. The surface ocean mass evolution is calculated by solving Eq. 2.30 and converted to sea level, outlined in Section 2.4.

The amount of water in the system (mantle and surface) is varied between 2 and 5 oceans; the efficiency of regassing at subduction zones F_r (Eq. 2.31) and degassing efficiency at MORs F_d (Eq. 2.34) are varied between 0 and 1 with orders of 0.001, 0.01 and 0.1. For each whole system water content tested, 29×29 models are run. Constraints for the water cycle are for present day conditions and cases are further constrained in time by examining the effects on the surface ocean. Cases which agree with the degassing flux of 10^{10} kg/yr to 10^{11} kg/yr for the present day are outlined (Figure 1.1 and Section 1.5) and compared with cases which have 1 ocean in the surface reservoir by the present day. Broader constraints of topographic exposure between 1 Gyrs and 2 Gyrs (see Section 5.1) are used for first order comparisons.

5.3 Results

5.3.1 Mantle Water Content

Figures 5.1, 5.2 and 5.3 present contour maps of mantle water content (ppm) at the present day (4.6 Gyrs) as a function of both F_d and F_r. At the point where $F_d = 0$ and $F_r = 0$, both regassing and degassing are reduced to zero (Eqs. 2.31 & 2.34), there is no transfer of water between reservoirs and the initial water content of both reservoirs is maintained for the model. For the models along the x-axis, $F_r = 0$ and only degassing operates. Similarly, along the y-axis, $F_d = 0$ and only regassing operates. First, I discuss models where water beings in the mantle, and then I move on to models where water starts at the surface.

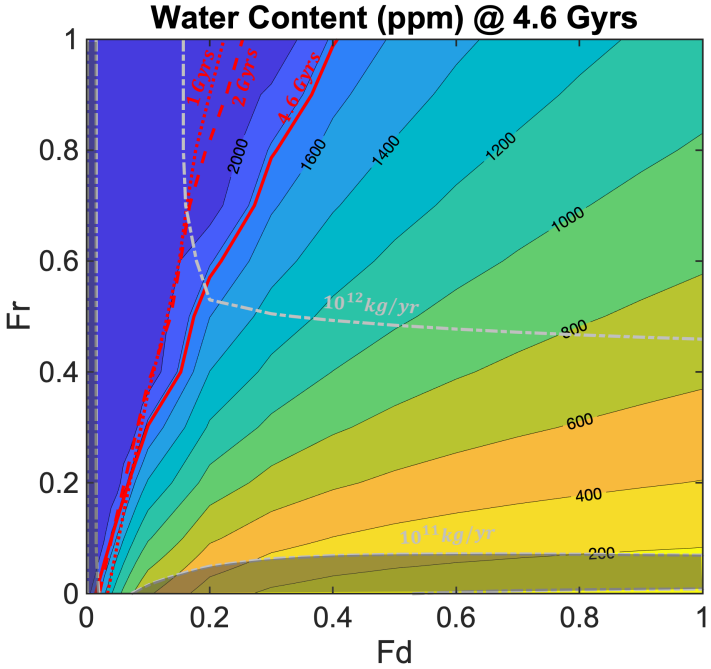

Figure 5.1: Contours in increments of 200 ppm show the water content at 4.6 Gyrs for various combinations of F_d and F_r in a system that begins with 5 oceans of water in the mantle. The solid, red contour shows for which values of F_d and F_r result with 4 oceans in the mantle and 1 ocean at the surface at present day. The red dashed and red dotted contours show which values of F_d and F_r give 4 oceans in the mantle and 1 ocean at the surface at 2 Gyrs and 1 Gyrs, respectively. Dashed-dotted grey lines represent the contours of 10^{10} kg/yr to 10^{12} kg/yr for degassing flux. The shaded grey region shows the values of F_d and F_r for which constraints on degassing flux at MORs are met.

Figure 5.1 shows the results of tests beginning with 5 oceans in the mantle. The contours intersect with the x-axis i.e. where $F_r = 0$ where only degassing operates, transporting water from the mantle interior to the surface as water begins in the interior. The grey, shaded regions show that cases that end up matching estimates for the present day degassing flux. However, when comparing with the mantle water content contours, it is clear that there is either too much or too little water in the mantle (hence too little or too much water at the surface, respectively). For cases in the region along the y-axis, regassing efficiency is higher than degassing efficiency and any water degassed to the surface is rapidly returned to the mantle, similar to having only regassing operating, essentially keeping all the water in the mantle. Cases in agreement with the degassing flux along the x-axis have little water in the mantle by 4.6 Gyrs as degassing efficiency is relatively high transporting almost all the water to the surface ocean.

The red contours show for which cases 4 oceans are in the mantle by 4.6, 2 and 1 Gyrs. When this contour crosses into the shaded region, degassing fluxes and 1 surface ocean mass constraints are met for the present day where $0.015 < F_d < 0.019$ and $0 < F_r < 0.017$. Contours indicating which cases have 4 ocean in the mantle by 2 and 1 Gyrs generally lie above the 4.6 Gyrs contour. This suggests that in order to meet the water content conditions earlier, regassing efficiency must be higher. Overlap with degassing constraints also occurs for the 2 Gyrs contour where $F_d \sim 0.021$ and $0 < F_r < 0.002$. In order to meet reservoir water content and degassing flux conditions, values of both F_d and F_r are very low with orders ≤ 0.01.

Figure 5.2 shows the models beginning with a dry mantle and 5 oceans at the surface. The mantle water content contours show little change when F_d and F_r are high but intersect the y-axis, a product of the new starting condition. When $F_d = 0$, as only regassing operates and water begins at the surface, water is only transported from the surface to the interior. Only one region occurs matching the present day degassing flux, covering low degassing and low regassing values. All three contours now overlap with net degassing estimates with 2 and 1 Gyrs clearly lying above the 4.6 Gyrs contour where higher F_r are required in order to subduct 4 oceans in a shorter period of time. However, as 2 and 1 Gyrs lie above 4.6 Gyrs contour at the present day, more than 4 oceans of water are subducted into the mantle, and they do not meet present day conditions. Cases along the 4.6 Gyrs contour meet degassing constraints when $0.002 < F_d < 0.02$ and $0.246 < F_r < 0.270$.

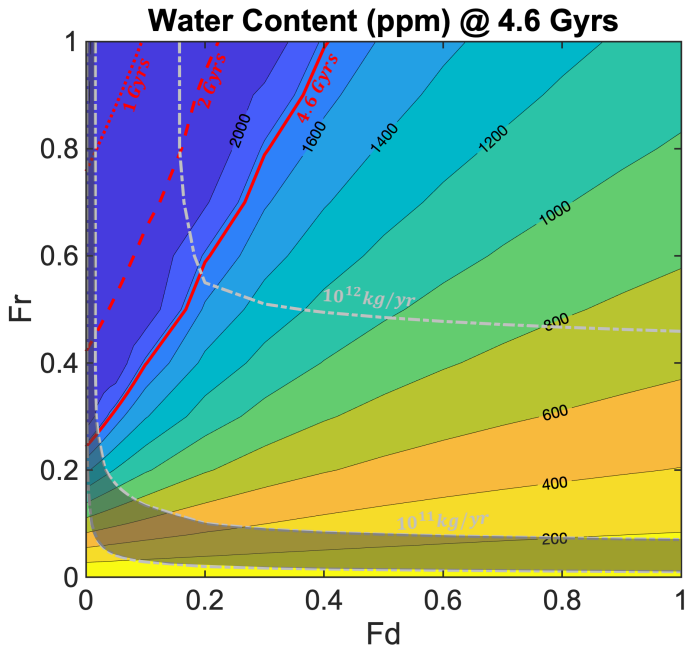

Figure 5.2: Contours show the water content at 4.6 Gyrs for various combinations of F_d and F_r in a system that begins with 5 oceans of water in the surface ocean.

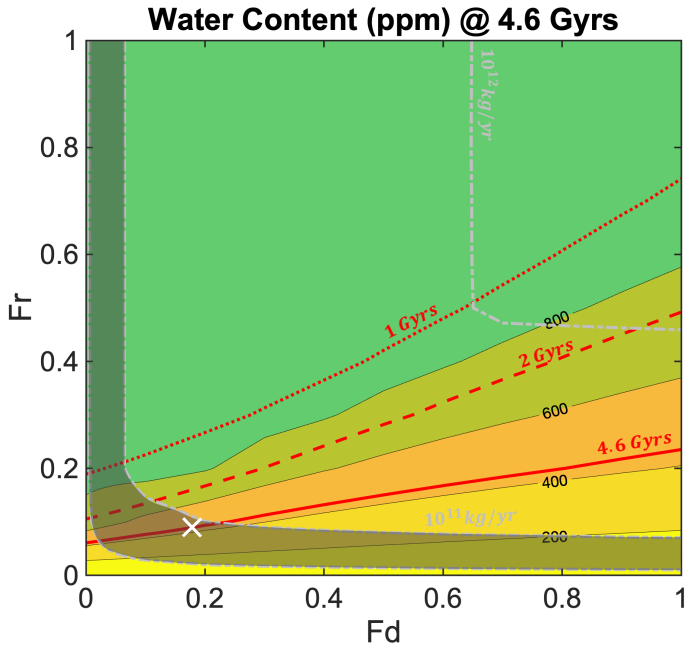

Figure 5.3: Contours show the water content at 4.6 Gyrs for various combinations of F_d and F_r in a system that begins with 2 oceans of water at the surface. The white cross indicated where $F_r = 0.09$ (van Keken et al., 2011) intersects with the 4.6 Gyrs contour in the grey region where $D = 10^{10-11}$kg/yr (Section 1.5).

Figure 5.3 shows models where only 2 oceans begin at the surface. Cases that agree with the degassing flux estimate are again seen where either F_d or F_r are low. The contours now mostly lie in the region where $F_d > F_r$; both the 2 and 1 Gyrs contours lie above the 4.6 Gyrs contour, indicating higher F_r are required to subduct 1 ocean in a shorter period. As before, this also indicates that the present day conditions of 1 ocean mass at the surface is not met as more than 1 ocean water has been subducted into the mantle, leaving the surface with less than an ocean. Figure 5.3 also shows a white x. This indicates the case which agrees with present day ocean mass, degassing flux and takes $F_r = 0.090$ from van Keken et al. (2011) as an additional constraint. $F_d = 0.182$ approximately twice the regassing efficiency.

5.3.2 Sea Level

Figures 5.1, 5.2 and 5.3 show a number of models are able to match one ocean at the surface now and the current degassing rate at MORs. Select models are presented in Figures 5.5 and 5.6 in order to understand the impact over time on the surface. Subducting oceans of water from the surface to the interior reduces the size of the surface ocean and hence lowers sea level.

Figure 5.4 shows sea level for different ocean masses with respect to the present day topography. The topography exposed to the surface is calculated by finding for which cumulative surface area fraction the sea level intersects the hypsometry. For example, for 1 ocean, the intersection is at 0.71 corresponding to the surface area covered by the ocean. To find how much is exposed to the atmosphere, the difference between the total area fraction and the point of intersection is calculated i.e. $1 - 0.71 = 0.29 \equiv 29\%$. Hence, for the present day 1 ocean mass leaves 29% of the hypsometry exposed. Similarly, the exposure can be calculated for 2-5 ocean masses. For 2 ocean masses, only 2 % of the topography is exposed, restricted to today's highest peaks. For any more oceans, the entire surface is flooded an none of the topography is exposed.

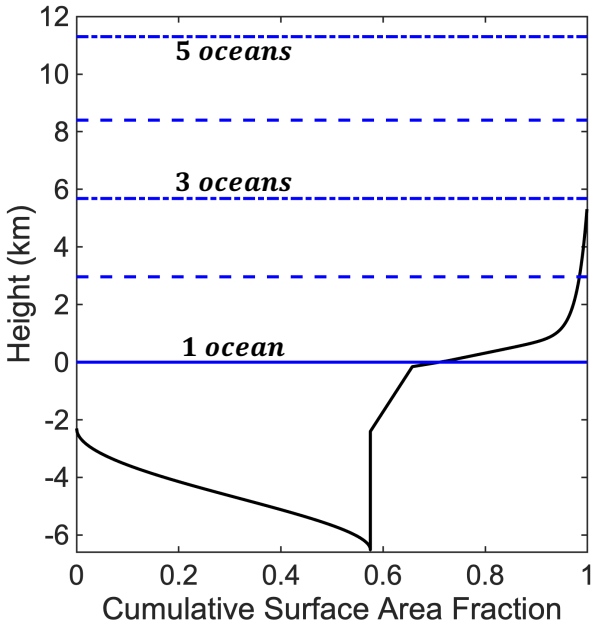

Figure 5.4: Present day hypsometry and corresponding sea level for 1 to 5 oceans.

		$\mathbf{F_d}$	$\mathbf{F_r}$	**Topography Exposure** (%)	
				1 Gyrs	2 Gyrs
$\mathbf{M_s}$ $(\mathbf{t = 0})$	2	0.124	0.080	3	5
	3	0.040	0.140	1	2
	4	0.020	0.199	0	1
	5	0.009	0.255	0	0
$\mathbf{X}$ $(\mathbf{t = 0})$	2195	0.019	0.017	42	37

Table 5.1: Starting ocean mass (or mantle water content) with corresponding values of F_d and F_r, and resulting topographic exposure at 1 Gyrs and 2 Gyrs for Figure 5.5.

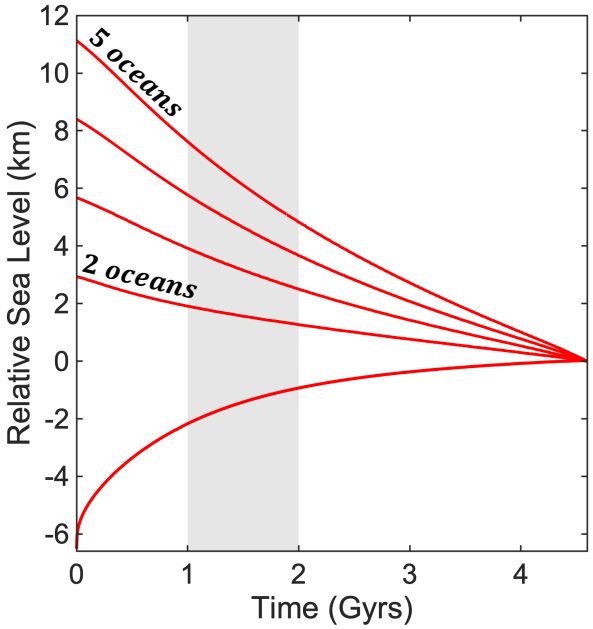

Figure 5.5: Evolution of sea level over time for starting with 2 to 5 ocean masses at the surface and 5 oceans in the interior. All meet the 1 ocean condition at 4.6 Gyr. The grey region corresponds approximately to times when there is evidence for continental exposure. The four curves beginning with a positive relative sea level begin with water in the surface ocean and the case that begins with a negative relative sea level begins with 5 oceans in the mantle.

Figure 5.5 shows the evolution of sea level for 5 cases: 1 case beginning with 5 oceans in the mantle and 4 cases beginning with 2, 3, 4 and 5 oceans at the surface (Table 5.1). When water begins in the mantle, initial sea level is −6.5 km, equivalent to having no water at the surface. Over the course of the evolution, the ocean mass and hence sea level increase such that by the present day, the sea level is as expected (at 0 km) and 1 ocean of water resides at the surface. Surface exposure by 1 Gyr is 42 % and by 2 Gyr, this has reduced to 37 %.

For the four cases starting with 2, 3, 4 and 5 oceans, some exposure is expected between 1 Gyrs and 2 Gyrs (Table 5.1). Beginning with 2-4 oceans exposes a few percent of the hypsometry to the atmosphere during this period whereas starting with 5 oceans does not expose the topography until after 2 Gyrs. Similarly, if the 1 ocean at the surface condition is met at 1 Gyrs (Figure 5.6), exposure is 29 %. However, the regassing of these models are too fast, leaving a dry surface for 2.5 Gyrs.

Figure 5.7 shows the evolution of regassing and degassing for the cases shown in Figure 5.5. Figure 5.7a shows that when water begins in the mantle, in order

		$\mathbf{F_d}$	$\mathbf{F_r}$
$\mathbf{M_s\,(t=0)}$	2	0.03	0.200
	3	0.02	0.396
	4	0.005	0.576
	5	0.009	0.779

Table 5.2: F_d and F_r values for Figure 5.6 to subduct 2-5 oceans by 1 Gyr. These values are also used ad the basis for Figure 5.8.

to get a release of water such that 1 ocean mass is at the surface by 4.6 Gyrs, degassing is required to be larger than regassing over the course of the evolution. The degassing flux estimate is met by the present day varying up to an order of magnitude. However, regassing is lower than present day estimates. Figure 5.7b shows the transport fluxes for cases where 2-5 oceans begin at the surface. Regassing fluxes lie higher than the degassing fluxes, both meeting flux constraints at the present day. Regassing flux is higher when there are more oceans in the system to subduct more oceans by the present day, also varying with increasing and decreasing plate velocity as described in Chapter 3. The evolving degassing flux is more complex. At the beginning of the model, degassing flux is zero as there is no water to be degassed. As the model progresses, water is subducted into the mantle and degassing flux increase rapidly. After 1 Gyrs, degassing decreases with decreasing plate velocity. In order to subduct oceans into the mantle and trap them regassing is required to be greater than degassing for the whole of Earth history.

5.4 Discussion

Models that begin with water in the mantle and end up with one ocean at the surface, slowly degas water into the surface ocean where sea level gradually increases from 0 to 1 ocean, over the course of 4.6 Gyrs. When water starts in the mantle (Figure 5.1), sea level is lower and topographic exposure is consistently higher than for the present day (Figure 5.5). Whilst there is geological evidence for lower relief in the past from continental flood basalts (Flament et al., 2011) and ancient erosional surfaces (Korenaga et al., 2017), none has thus far suggested that exposure is more than the present. Thus these models are not considered as

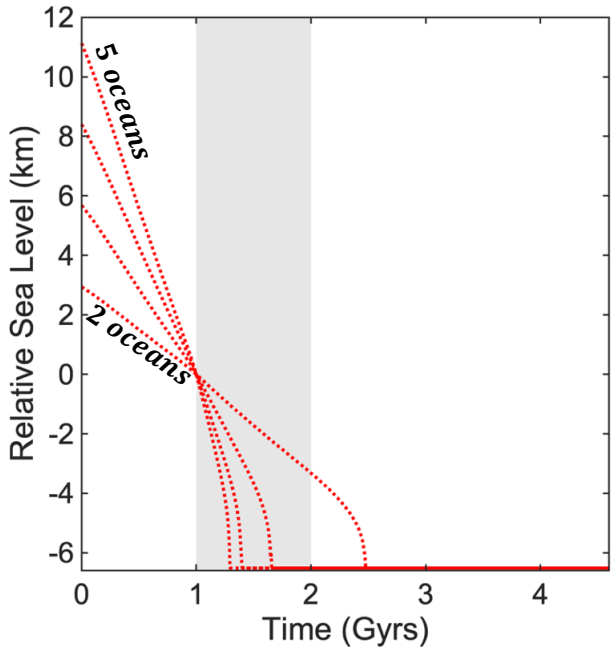

Figure 5.6: Evolution of sea level over time for starting with 2 to 5 ocean masses, but meeting 1 ocean condition at 1 Gyr.

representative of Earth.

Instead, attentions are turned to those models that begin with water at the surface. Consider a case where water can be quickly returned to the mantle until it is saturated (Figure 5.8). At saturation, 4 oceans are expected in the mantle and 1 ocean at the surface. If this is by 1 Gyrs, 4 oceans would have to be subducted in the first 1 Gyrs (Figure 5.6), at $\sim 5 \times 10^{12}$ kg/yr, five times larger than the regassing flux today. This would also require water capacity of mantle minerals to be 4 oceans, the capacity expected for the present day mantle (Section 1.3). Any further subduction of water would result in over-saturating the mantle, and any excess water would be rapidly returned to the surface. Any water that is subducted after 1 Gyrs must be balanced by degassing of the excess (Figure 5.8b). Both degassing and regassing would be required to balance each other, and both decreases at the same rate, as the mantle cools. Degassing need to increase by almost two orders of magnitude after 1 Gyrs in order to match the water being subducted into the mantle (Figure 5.8b). This increase also results in the degassing flux at the present day becoming over an order of magnitude higher than the upper limit of 10^{11} kg/yr. Even if mantle saturation was only 1 ocean (indicated by 2 oceans lines in Figure 5.8), degassing is approximately five times higher than expected. This implies that subducting oceans and keeping

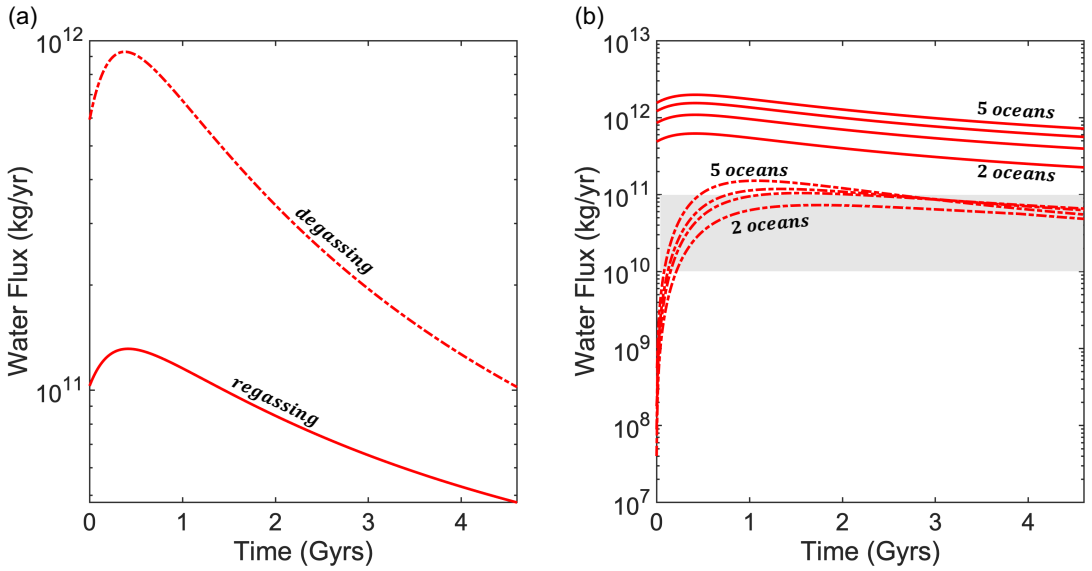

Figure 5.7: Transport fluxes for cases presented in Figure 5.5 showing degassing (dashed-dotted) and regassing (solid) for (a) 5 oceans starting in the mantle and (b) 2-5 oceans beginning at the surface.

them in the mantle is not plausible.

To best meet observational constraints (degassing flux and present day ocean mass), the models that begin with water at the surface suggest there are at most 2 oceans in the mantle-surface ocean reservoirs with only 1 ocean (or likely less) in the mantle. Evolving sea level provides further constraints; the representative cases in Figure 5.5 show only a few percent of topography exposed during times equivalent to the Archean. These models show sea level with respect to the present day hypsometry. However, during the Archean, topographic relief is expected to be less extreme due to the hotter mantle at this time (Flament et al., 2008). With a damped hypsometry, continental topography would be lower and even two oceans would easily submerge almost all continents. In order to match similar constraints of continental exposure as expected for the present day, less than two oceans at the start would be required resulting in less than 1 ocean being subducted to meet this condition (Bindeman et al., 2018).

The ocean mass-sea level relationship is not restricted to parametrised models and can be extended to interpret results from 2D and 3D models of the water cycle. For example, Nakagawa and Nakakuki (2019) subduct over 10 oceans into the mantle from the surface ocean over the course of 4.6 Gyrs. This would result in topography exposure only in the last 0.1 Gyrs, when the surface ocean mass is more comparable to the present day. Similarly, Price et al. (2019) begin with 5

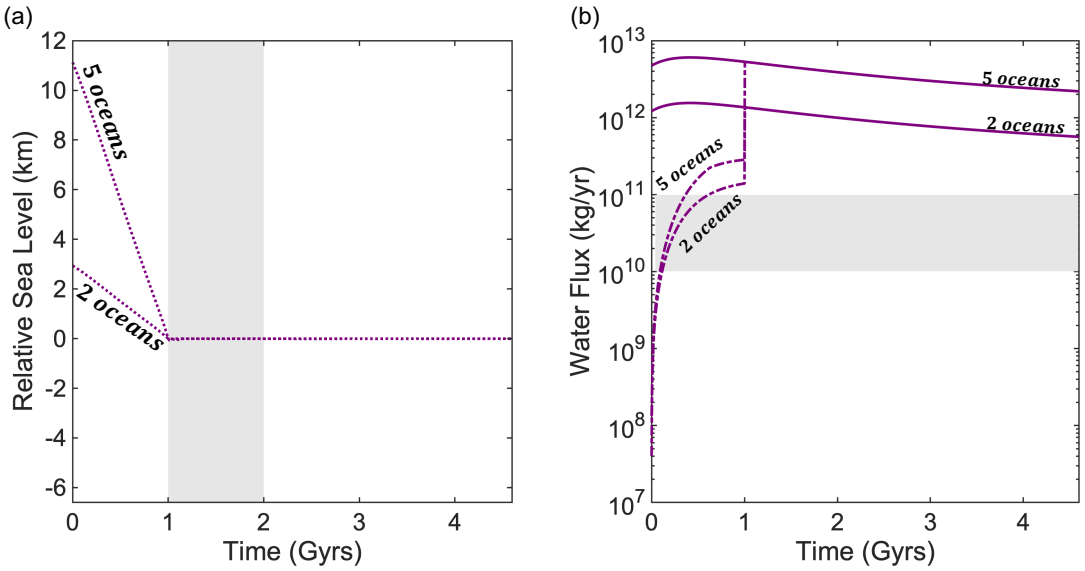

Figure 5.8: Schematic evolution of sea level over time when starting with 2 and 5 ocean masses at the surface, meeting 1 ocean condition at 1 Gyrs. After 1 Gyrs, the mantle becomes saturated and any subducted water that over-saturates the mantle is degassed. To keep the ocean mass and sea level constant after 1 Gyrs, regassing must be balanced by degassing.

oceans in their mantle-surface system. Approximately ∼1.5 oceans are subducted into the mantle over 0.9 Gyrs leaving 2.5 oceans at the surface until the end of the model. Therefore in order to have only one ocean at the surface, the Earth can only have 2.5 oceans across both reservoirs.

It is interesting to further consider the effects of water capacity of mantle minerals, varying over Earth evolution. Given the assumptions of low solubility after magma ocean solidification (Section 2.5.2), these models could be considered a conservative estimate for mantle water content. If initial mantle (post magma ocean) water solubility is higher than estimated here, this would result in a higher starting mantle water content, the resulting evolution of which is discussed in Chapter 3. It also still unclear if the magma ocean crystallised from the bottom-up or middle-out. The middle-out scenario has been suggested to trap and maintain a magma ocean in the lower mantle (e.g. Labrosse et al., 2007) and the consequences for water transport in this part of the mantle and at this time are unknown.

As previously discussed, after mantle solidification water capacity may be very low. However as the mantle begins to cool and subduction begins (not necessarily as part of the present day plate tectonic regime) to bring water into the mantle,

the water cycle is likely restricted to the upper mantle (Tikoo and Elkins-Tanton, 2017). If water from accretion is retained through the magma ocean stage and survives large impact, degassing events, high water capacities coupled with high convective vigour would result in wide-spread melting. Zircon evidence suggests that some form of crustal recycling must be occurring in the Hadean as early as 4.1 Ga and also show signatures of water interactions (Trail et al., 2018). Geodynamic studies have also shown effective recycling via the heat pipe mechanism and intrusive magmatism. Heat pipes (Moore and Webb, 2013) are the conduits through which melts and heat are brought to the surface. Rapid downward advection easily buries material, reaching the base of the lithosphere. However, this cool material will exceed the solidus and melts again, returning to the surface. Similarly, intrusive magmatism in the 'squishy lid' framework (Lourenço et al., 2018) warms and thins the lithosphere facilitating recycling of the crust and cooling of the mantle. During these multiple episodes of melting and recycling, the water preferentially partitions into the solid from the melt. For the heat pipe model, water would be expected to escape to the surface. For water in intrusive melts of the squishy lid model, it would freeze into the lithosphere. As the lithosphere becomes thinned and delaminates, water could be taken into the mantle. However, as it reaches deeper regions at a time when higher temperatures render water capacity to be low, water would again be released towards the surface. Deep water in the earliest times of solid-state convection of the Earth are hence unlikely. This restriction could be key to understand how water has helped to facilitate plate tectonics without pervasively hydrating the mantle, as seen in OIBs and MORBs (Section 1.4).

5.5 Conclusion

The evolution model presented in Section 2.2 is used to test the conditions under which 4 oceans can reside in the mantle by the present day. In order to meet present day degassing flux estimates, both degassing and regassing fluxes cannot have been greatly different than today. To also meet ocean mass conditions for the present day, the total amount of water in the system is best matched by having only 2 oceans across both the mantle interior and surface ocean.

To investigate the potential effects on the surface, the evolving surface ocean mass is converted to sea level (Section 2.4). For exposed topography by $1-2$ Gyrs, expected by geological data, the mantle cannot contain more than $\sim$1 ocean or

less of water. Further consideration of temperature-dependent water capacity for mantle minerals is vital for understanding where water resides throughout Earth history and the role of water in plate tectonics.

5.6 Summary

- How much water is in the mantle today?
- Giant impacts inducing magma oceans and the low water capacity of newly solidified mantle minerals would drive almost all the water present in a magma ocean to the surface
- To match present day ocean mass, any excess oceans must be subducted by the present day
- To match present day degassing fluxes, there cannot be more than 2 oceans across the surface ocean and in the mantle
- Further consideration of sea level and continental exposure suggest even less than 1 ocean mass may reside in the mantle

6 Concluding Remarks

This thesis uses a parametrised model to investigate the thermal evolution and water cycle on Earth, based on the analytically derived relationship between the Rayleigh number and plate velocity (Section 2.1). The chapters presented employ constraints and consideration of the time-dependent nature of convection in a viscous medium to investigate feedbacks that control the system and potential effects on the surface environment.

6.1 Viscosity Controls

As viscosity is the fundamental control on planetary evolution, determining which viscosity law is most applicable to Earth evolution is first investigated in Chapter 3. The range of mid-mantle (1400km) viscosity estimates from glacio-isostatic rebound are used to form three initial viscosity laws that give 10^{21}, 10^{22} and 10^{23} Pa s at 2200 K. These laws give three different thermal histories in the evolution model (Section 2.2) and the law constrained to give 10^{23} Pas best matches the expected present day, mid-mantle temperature of 2200 K. Lower viscosities for the other laws facilitated rapid plate velocities and therefore higher surface heat flow, promoting rapid cooling and present day temperatures much lower than expected. By similar reasoning, water-dependent laws maintain lower viscosities as water is subducted into the mantle. The 10^{23} Pas calibrated law has the most reasonable plate velocities throughout it's evolution and matches the present day temperature.

This suggests that for Earth, temperature is the main control on evolution. These results also imply that either water has little or no effect on viscosity or there is not enough water in the mantle to considerably affect evolution. Experimental results have shown both a large and small effect of water on viscosity (Fei et al., 2013, and references therein) whilst samples of mantle water content (Section

1.4) suggesting that the mantle is under-saturated Section 1.3. The mantle water content was subsequently explored further in Chapter 5.

6.2 Mantle Mixing

The implicit assumption of parametrised models (Chapters 3 and 5) is that any water subducted into the system is instantaneously and homogeneously mixed into the mantle, and also be transported back to the surface ocean instantaneously. Geochemical constraints show that this is not the case (Section 1.8) and in order to understand some of the differences that arise between parametrised and dimensional models, Chapter 4 seeks to understand the effects of a mixing time in the parametrised evolution model. Mixing is implemented in the evolution model as a time lag in arrival of water at the mid-ocean ridge (Section 2.3). Two mixing end-members are considered where the mixing time, defined as the time taken for subducted water to reach a MOR, is constant or variable with Ra. High Ra are associated with fast plate velocities and hence short mixing times whilst low convective vigour results in long mixing times.

Regardless of the mixing end-member, mixing acts to trap water in the mantle and therefore mantle water content is higher in cases that consider mixing in comparison with those that do not. Mixing times on the order of hundred of millions of years to billions of years can also induced periods of net degassing, where the delayed arrival of water allows degassing of water to exceed regassing at subduction zones. Variable mixing acts to greatly restrict the appearance of this period due to to short mixing times early on in the model.

Mixing traps water in the mantle at the expense of the surface ocean, and when examining the effects on the surface for a specific time such as the present day, the water cycle may be in or soon after a period of net degassing. If this is the case, more water may be at the surface than expected. When the water cycle is in a state of net regassing, more water is in held in the mantle and less is expected at the surface. Mixing times greater than $\sim$2 Gyrs result in all of the water in the system being subducted whilst mixing times less than $\sim$0.1 Gyrs show little difference compared with instantaneous (i.e. no) mixing. The cases that best agrees with the 1 ocean mass constraint at 4.6 Gyrs are for constant and variable mixing (with a temperature-dependent viscosity law) for mixing times of 1 and 0.8 Gyrs, respectively, within the range of mixing times expected for today

(discussed in Section 4.4.3).

On Earth, plate tectonics as it operates today is not thought to have occurred throughout its history, as this model implies. This would require water to be rapidly subducted into the mantle, such as during periods of continental break-up (Karlsen et al., 2019) or potentially rapid subduction episodes in the Early Earth (Sleep et al., 2014). This rapid influx and delay in outflux of water of the mantle may also explain rapid periods of net regassing and net degassing seen mainly in 2D models.

6.3 Surface Ocean Constraints on Mantle Water Content

Many studies regarding the water cycle suggest 4 oceans or more may reside in the mantle. Chapter 5 takes the evolution model, varying degassing and regassing efficiencies to find under which conditions 4 oceans may reside in the mantle by the present day, if regassing efficiency is greater than degassing efficiency. Comparison with degassing flux for the present day indicates that conditions are best matched when water begins at the surface rather than in the interior.

As when considering the effects of mixing, the impact on the surface can be assessed. In particular, the development of a procedure to convert ocean mass to sea level with respect to a present day hypsometry allows the measurement of continental exposure throughout Earth history. However, exposure in the Archean is expected to be similar to the present day, and in order to match these constraints, even less than one ocean is expected to be subducted suggesting that the mantle is under-saturated at present.

6.4 Outlook and Future Avenues

The dry, thermally controlled evolution of the mantle best fits present day mantle temperatures and viscosities, surface ocean mass, regassing and degassing fluxes and continental exposure conditions. There are opportunities, particularly based on the work from Chapters 4 and 5 to investigate the effects of mixing and modelling continental exposure. The mixing implementation can easily be extended to isotopic reservoirs such as $^{3He}/_{4He}$ and ^{40}Ar discussed in Section 1.8, and can act

as a further constrain for Earth evolution. The ocean mass-sea level relationship could be further developed, to take into account a variable hypsometry. Whilst conclusions from Chapter 5 would still be applicable, further complexities may arise due to isostatic balance and be more relevant when comparing to geological data.

Lastly, it is clear the understanding of the water cycle would be greatly extended if further laboratory experiments and first principles simulations were carried out regarding the temperature-dependent water capacity of mantle minerals. Understanding how this varies, particularly at the high-pressure, high-temperature conditions across the mantle would not only benefit our understanding of the Earth, but other silicate planets as well.

A Evolution Code

A.1 multi_runs.m

Main function that runs code with given input parameters.

```
clear all; close all

tic
%% Background
% Author: Kiran Chotalia
%         kiran.chotalia.11@ucl.ac.uk
%         6th Nov 2019

% This code is based on the code of Crowley et al. (2011), solving for the
% thermal evolution of a planet with Earth-like plate tectonics. It solves
% the three differential equations for dT/dt, dXm/dt and dMs/dt.

% (1) Set input paramters below
%       - can run for single or multiple cases
%       - columns are separate cases
% (2) Choose settings for solver
%       - details for choosing viscosity law, see eta_calc.m
%       - number of timesteps, nsteps, best at 1e3
%       - for mixing, nsteps should be 2e3
% (3) Set figure generation


%% %%%%%%%%%%%%%%%%%%%%%%%%%%%% CHANGE HERE %%%%%%%%%%%%%%%%%%%%%%%%%%%%

%% Input Parameters
% - Viscosity -
SET.etalaw   = [ 100         ]; % Viscosity Law (see eta_calc.m for more details)
IN.eta0      = [ 7.53e15     ]; % Calibration Viscosity (Pas)
IN.E         = [ 300e3       ]; % Activation Energy (J/mol)
IN.beta      = [ 2/3         ]; % Exponent for U proportional to Ra^(m)

% - Temperature -
IN.T         = [ 2500        ]; % Initial Average Mantle Temperature (K)
IN.Hsf       = [ 1.706       ]; % Scaling for Radiogenic Heating (non-dim)

% - Water -
IN.Xm        = [ 0           ]; % Initial Mantle Water Concentration (ppm)
IN.Ms        = [ 1.723       ]; % Initial Surface Ocean Mass (multiples of 1 ocean = 1.39e21 kg
    )
IN.Fd        = [ 1           ]; % Degassing Efficiency (non-dim)
IN.Fr        = [ 0.15        ]; % Regassing Efficiency (non-dim)

% - Mixing -

IN.mixing    = [ logical(1) ];
    IN.mixlag    = [ 1e9         ]; % Mixing Time (years)
    IN.Rapd      = [ 1e6         ]; % Present Day Rayleigh Number (Ra)
    IN.varmix    = [ 0           ]; % 1 = Variable Mixing 0 = Constant Mixing
    IN.m         = [ 2/3         ]; % Exponent for Variable Mixing Scaling

%% Settings
% - Solver -
```

```
SET.end      = 1;                        % Multipes of Earth Age i.e. how long to run solver
    for 1 => 4.6 Gyrs, 2 => 2 x 4.6 Gyrs etc...
SET.nsteps   = [ 2e3        ] .* SET.end; % Number of timesteps in 4.6 Gyrs (recommended: 2e3)
SET.cases    = length(IN.T);              % Number of cases to compare (i.e. no. of columns
    above). Set with respect to length of IN.T array

% - Figures -

FIG.make         = [2];        % generate figures; see fig_plot for details 1=subplots 2=
    individual figures (for posters, papers, talks etc.)
FIG.save         = [1];            % save figure to FIG.savename
FIG.savename     = 'test/test';    % data saved in working directory as FIG.savename.mat file
FIG.fntsz        = 36;             % font size (suggested 36 for individual figures, 20 for
    subplot)
FIG.lim          = [0 4.6];        % time (x-)axis range (Gyrs)
FIG.calib        = [1];            % show present day calibration guides = 1
FIG.lc           = [ 1 0 0 ];      % matrix of rgb colours for each case
FIG.ls           = char('-');      % line styles for each case


%% %%%%%%%%%%%%%%%%%%%%%%%%%%%%%%%%%%%%%%%%%%%%%%%%%%%%%%%%%%%%%%%%%%%%%%%%%%%%%%%%%%
%% Solve to compare multi

for i=1:SET.cases

    output{i,1}=solver_Eqs(IN.Xm(i),IN.T(i),FIG.make,IN.Hsf(i),FIG.savename,...
        SET.nsteps(i),SET.etalaw(i),IN.Ms(i),IN.eta0(i),SET.end,...
        IN.Fr(i),IN.Fd(i),IN.mixlag(i),IN.Rapd(i),IN.varmix(i),IN.mixing(i),...
        IN.m(i), IN.beta, IN.E(i));

    clear global
end

%% Saving Data
if(isempty(FIG.savename)==0)
   save(FIG.savename,'output');
end

%% Plotting Figures
% Can use this section to plot cases that have already been calculated
% load a saved .mat file (load(FIG.savename)) and click 'Run Section'

for x=1:length(FIG.make)
    fig_plot(FIG.make(x),FIG.savename,output,SET.cases,FIG.save,...
        FIG.fntsz,FIG.lim,FIG.calib,[],IN.mixing,FIG.ls,FIG.lc)
end

%%
toc
```

A.2 solver_Eqs.m

Controls inputs depending on which solver to use (native or SOLVER_vart2_wetstart.m). Calculates relative strength number and saves output for plotting.

```
% clear all
% close all

%%
function output = solver_Eqs(Xm_init,T_init,fig,Hsf,savename,nsteps,etalawin,...
    Ms_init,etain,fin,Fr,Fd,mlag_yrs,Rapd,varmix,mixing,m,beta,E)
%% Input Parameters

par_solver;
t_fin = fin*4.6e9*yr_s;

global etalawin
global dynsol
global etain
global Fr
global Fd
global etain
global m
global Hsf
global beta
global E

%% Solving

if mixing
        % Fourth Order Runge-Kutta solver
        [t,X,tlag,Xmlag,mixt,merror] = SOLVER_vart2_wetstart(linspace(0,t_fin,nsteps),[
            Xm_init,T_init,Ms_init],mlag_yrs,Rapd,varmix);

        % defining output from solver
        t = t(1:end-1)';
        Xm = X(1:end-1,1);
        T  = X(1:end-1,2);
        Ms = X(1:end-1,3);

        output.Xmlag = Xmlag';
        output.mixt = mixt';
        output.mterr = merror'; % error associated with variable mixing time
        output.Rapd = Rapd;
        output.tlag_Ga = tlag'./(yr_s*1e9); % Ga

else

        % ode15s matlab solver

        options=odeset('NonNegative', [1 2 3], 'AbsTol', [1e-4 1e-2 1], 'MaxStep', t_fin/1e3)
            ;
        [t,X]=ode15s(@derivatives_solver,linspace(0,t_fin,nsteps),[Xm_init,T_init,Ms_init],
            options);

        % defining output from solver
        Xm = X(:,1);
        T  = X(:,2);
        Ms = X(:,3);

        output.mterr    = [];
        output.mixt     = [];
        output.Xmlag    = [];
        output.mixt     = [];
        output.mterr    = []; % error associated with variable mixing time
        output.Rapd     = [];
        output.tlag_Ga  = []; % Ga


end
```

```
%% Calculate Dynamic Quantities
% to save for output

if mixing
    % whole mantle averages
    [eta,Ra,U,dl,zm,dM_dt,~,R,D,Qs,H,~]...
        = dynamics_solver_paper_maths(t,Xm,T,etalawin,etain,Fr,Fd,Hsf,beta);
    % MOR (lag) values
    [eta_lag,Ra_lag,U_lag,dl_lag,zm_lag,~,~,R_lag,D_lag,Qs_lag,~,~]...
        = dynamics_solver_paper_maths(t,Xmlag',T,etalawin,etain,Fr,Fd,Hsf,beta);
else

    [eta,Ra,U,dl,zm,dM_dt,~,R,D,Qs,H,~] = dynamics_solver_paper_maths(t,Xm,T,etalawin,etain,
        Fr,Fd,Hsf,beta);

end

%% POST PROCESSING
%% Calculate Relative Strength Number Swt

if mixing
    Xmlag_in = max(Xmlag',1);
    [etaT,etaXm,Swt] = relstrno(T,Xmlag_in,eta_lag,R_lag,D_lag,Qs_lag,H,etalawin);
else
    [etaT,etaXm,Swt] = relstrno(T,Xm,eta,R,D,Qs,H,etalawin);
end

%% Save to Output
%output = zeros(1,37);

output.t_Ga = t/(1e9*yr_s);    %Ga
output.T = T;                  %K
output.Xm = Xm;                %ppm
output.Ms = Ms;
output.U = U*100*yr_s;         %cm/yr
output.eta = eta;              %Pas
output.Ra = Ra;
output.dl = dl/1e3;            %km
output.zm = zm/1e3;            %km
output.dM_dt = dM_dt;          %kg/s
output.Xp = Xp;                %ppm
output.Fd = Fd;                %dimensionless
output.Fr = Fr;                %dimensonless
output.R = R*1e-6*yr_s;        %kg/yr
output.D = D*1e-6*yr_s;        %kg/yr
output.Qs   = Qs;                %W
output.H    = H;                 %W
output.Hsf  = Hsf;
output.E    = E;                 %J/mol
output.etalaw = etalawin;      %viscosity law (see eta_calc.m for more details)
output.etain  = etain;          %eta0 calibration constant
output.etaT   = etaT;           %Pas/T
output.etaXm  = etaXm;         %Pas/ppm
output.Swt    = Swt;              %dimensionless
output.Ur     = H./Qs;            % Urey Ratio
output.Nu     = (Qs.*d)./(Kc.*T.*S); % Nusselt Number
output.timesteps  = nsteps;       % number of timesteps

if mixing
    output.R_lag = R_lag*1e-6*yr_s;       %kg/yr
    output.D_lag = D_lag*1e-6*yr_s;       %kg/yr
    output.eta_lag = eta_lag;             %Pas
    output.Qs_lag = Qs_lag;               %W
    output.m = m;                       % mixing exponent
    output.mlag    = mlag_yrs;            % mixing lag input in years
    output.zm_lag = zm_lag./1e3; %km
else
    output.R_lag = NaN;
    output.D_lag = NaN;
    output.eta_lag = NaN;
    output.Qs_lag = NaN;
    output.m = NaN;
    output.mlag    = NaN;
    output.zm_lag = [];
end
```

A.3 derivatives_solver.m

Calculates derivates $^{dT}/_{dt}$, $^{dX}/_{dt}$ and $^{dM_s}/_{dt}$.

```
%% Calculates dT/dt, dX/dt and dMs/dt
% calculates derivates for use in ode15s solver

function [dX] = derivatives_solver(t,X,Xm_lag)

% X(1) = Mantle Water Content
% X(2) = Average Mantle Temperature
% X(3) = Surface Ocean Mass

% call global parameters
global etalawin
global etain
global Fr
global Fd
global Hsf
global beta

% if number or arguments in is greater than or equal to 3 and Xm_lag is empty
if nargin >= 3 && ~isempty(Xm_lag)>0
    % use Xm_lag instead of Xm so can calculate with delayed values of Xm
    Xm = Xm_lag;
else
    Xm  = X(1);
end
T   = X(2);
Ms  = X(3);

% only extract needed values from dynamics solver
[~,~,~,~,~,~,~,R,D,Qs,H,~] = ...
    dynamics_solver_paper_maths(t,Xm,T,etalawin,etain,Fr,Fd,Hsf,beta);

% contstant parameters
Cp    = 1000;  %J/kg.K specific heat
rho   = 3500;      %kg/m^3 density
V     = 9.05e20;
M_oc = 1.39e21; % surface ocean mass

% calculate derivatives
dX(1) = (R-D)./(rho.*V); %Xmdot = ppm/s
dX(2) = (-Qs+H)./(Cp.*rho.*V); %Tdot = K/s %Qcmb
dX(3) = (1./(M_oc.*1e6)).*(D-R); %1e-6*rho*V/M_oc = 0.0023

% stops ocean mass and mantle water content becoming < 0
if X(1)<=0.1 && dX(1)<0
    % if Xm < 0.1 AND the rate of change of the smantle water content is -ve
    dX(3)=0;
    dX(1)=0;
     X(1)=0;
    % make both the change in X and Ms = 0
end

if X(3)<=1e-3 && dX(3)<0
    % if Ms < 1e-3 AND the rate of change of the surface ocean mass is -ve
    dX(3)=0;
    dX(1)=0;
     X(3)=0;
    % make both the change in X and Ms = 0
end

dX=dX';
```

A.4 SOLVER_vart2_wetstart.m

Calculates derivates $^{dT}/_{dt}$, $^{dX}/_{dt}$ and $^{dM_s}/_{dt}$. Considers constant and variable mixing, using fourth-order Runge-Kutta methods.

```
%% Fourth Order Runge Kutta Solver

% takes into account constant (default) and variable mixing (set in multi_runs.m)

% Y = vector of initial values [Xm, T, Ms and Tc]
% t = vector of time

%%
function [t,Z,tlag_out,Xm_lagvec,mixt,mixterr] = SOLVER_vart2_wetstart(t,Y,lag_yrs,Rapd,
    varmix,dZmax)

% call global parameters
global etalawin
global etain
global m
global E

% set maximum values for derivatives
if(nargin < 6)
    dZ_max = [0.1; 0.1; Inf];
end

% constants
rho = 3500;              %kg/m^3 density
alpha_ra = 2.5e-5;       %1/K thermal expansion coefficient
g = 10;                  %m/s^2 gravitational acceleration
yr_s = 60*60*24*365.25; % 1 yr in seconds
d = 2880e3;              %m depth of mantle
L=2*d;                   %m plate length
Kc = 3;                  %W/m.K thermal conductivity
Cp = 1000;               %J/kg.K specific heat
k = Kc/(Cp*rho);         %m2/s thermal diffusivity
Rp = 6371e3;                 %m Earth radius
d = 2880e3;                  %m mantle depth
Rc = Rp - d;                 %m core radius
V = 4*pi/3 * (Rp^3 - Rc^3); %m^3 mantle volume
M_oc = 1.39e21;              %kg ocean mass for Earth at present day

% timestepping
h = t(2)-t(1);                  % time step size
nsteps = length(t);             % total number of time steps
Z = NaN(length(t),length(Y));   % set up array to save solved values
Z(1,:) = Y;                     % first row of array equivalent to initial values

% mixing time units
tlag = yr_s*lag_yrs; % time lag in seconds

% set up empty vectors
tlag_out = NaN(1,nsteps*2);     % time lag out
Xm_lagvec = NaN(1,nsteps*2);    % water lag out = MOR Xm
mixt = NaN(1,nsteps*2);         % mixing time
mixterr = NaN(1,nsteps*2);      % mixing time error
Xm_lag_vec = NaN(10,1);         % water content when iterating for variable mixing time
tw_extra = [];                  % extra time to consider when lag degasses all water that
    starts in the mantle. lag 'resets'

%% RK4
for i=1:nsteps*2

        % tlag/h = no. of timesteps tlag is equivalent to i.e. = i
        % ilag = max(1, round(i - tlag/h));

        % time we want to find
        % tw = t(i) - tlag;

            if Z(1,1)>0
                if isempty(tw_extra) && Z(i,1)==1
```

```
%                     disp('wet start: all water degassed')
                    tw_extra = t(i);
                    tw_extra_i = i;
                    Xm_lag = Z(tw_extra_i,1);
                    ilag = tw_extra_i;

                elseif ~isempty(tw_extra) && Z(i,1)~=1

                    if t(i)<tlag
%                         disp('wet start: only regassing operating')
                        Xm_lag = Z(tw_extra_i,1);
                        ilag = tw_extra_i;
                    else
%                         disp('wet start: degassing starts again?')
                        tlag_new = tlag-t(tw_extra_i); % tlag adjusted for degassing during
                            wet start
                        tw = t(i) - tlag_new;
                        [~,ilag] = min(abs( t(1:i) - tw ));
                        Xm_lag = Z(ilag,1);
                    end

                elseif ~isempty(tw_extra) && Z(i,1)==1 && varmix
                    if t(i)<tlag
%                         disp('wet start: only regassing operating')
                        Xm_lag = Z(tw_extra_i,1);
                        ilag = tw_extra_i;
                    else
%                         disp('wet start: degassing starts again?')
                        tlag_new = tlag-t(tw_extra_i); % tlag adjusted for degassing during
                            wet start
                        tw = t(i) - tlag_new;
                        [~,ilag] = min(abs( t(1:i) - tw ));
                        Xm_lag = Z(ilag,1);
                    end

                else
%                     disp('normal')
                    tw = t(i) - tlag;
                    [~,ilag] = min(abs( t(1:i) - tw ));
                    Xm_lag = Z(ilag,1);
                end

            else
%                     disp('normal')
                    tw = t(i) - tlag;
                    [~,ilag] = min(abs( t(1:i) - tw ));
                    Xm_lag = Z(ilag,1);
            end

%% Variable Mixing
% default mixing type is constant unless variable mixing is switch on

switch varmix
    case 1 % variable mixing time
        % smooth lag
        smooth_lag = 1;
        if(smooth_lag==1)
            ilag = ilag + (-2:2); % convert ilag to array
            ilag = ilag(ilag>0); % make sure ilag does not go -ve
            ilag = ilag(ilag<=size(Z(isfinite(Z(:, 1)), :),1));
            Xm_lag = mean(Z(ilag,1)); % new Xm_lag with smoothed ilag
            ilag = mean(ilag); % mean of array ilag values
        else
        end

            for n=1:10 % iterate
                % adjusts mixing lag so it scales with Rayleigh number
                % use whole mantle averages to calculate eta and Ra
                eta = eta_calc(Z(i,1),Z(i,2),etalawin,etain,E); % viscosity
                Ra = (alpha_ra.*rho.*g.*Z(i,2).*d^3)./(k.*eta); % Rayleigh number

                % use this Ra to scale mixing time
                mixt(i) = lag_yrs * (Ra / Rapd)^(-m);   %years
                lag_yrs_n = lag_yrs * (Ra / Rapd)^(-m); % Iterate through Mixing Lag
```

```
                tlag_n = yr_s*lag_yrs_n;                % time lag in seconds
%{
                % Calculate new ilag with mixing time adjusted time lag
                % tlag_n
%                 ilag = max(1, round(i - tlag_n/h));
%                 tw = t(i) - tlag_n;
%                 [~,ilag] = min(abs( t(1:i) - tw ));
%}

%% Calculate new ilag with mixing time adjusted time lag

            if Z(1,1)>0
                if isempty(tw_extra) && Z(i,1)==1

%                     disp('wet start: all water degassed')
                    tw_extra = t(i);
                    tw_extra_i = i;
                    Xm_lag = Z(tw_extra_i,1);
                    ilag = tw_extra_i;

                elseif ~isempty(tw_extra) && Z(i,1)~=1

                    if t(i)<tlag_n
%                         disp('wet start: only regassing operating')
                        Xm_lag = Z(tw_extra_i,1);
                        ilag = tw_extra_i;
                    else
%                         disp('wet start: degassing starts again?')
                        tlag_new = tlag_n-t(tw_extra_i); % tlag adjusted for degassing during
                            wet start
                        tw = t(i) - tlag_new;
                        [~,ilag] = min(abs( t(1:i) - tw ));
                        Xm_lag = Z(ilag,1);
                    end

                elseif ~isempty(tw_extra) && Z(i,1)==1 && varmix
                    if t(i)<tlag
%                         disp('wet start: only regassing operating')
                        Xm_lag = Z(tw_extra_i,1);
                        ilag = tw_extra_i;
                    else
%                         disp('wet start: degassing starts again?')
                        tlag_new = tlag-t(tw_extra_i); % tlag adjusted for degassing during
                            wet start
                        tw = t(i) - tlag_new;
                        [~,ilag] = min(abs( t(1:i) - tw ));
                        Xm_lag = Z(ilag,1);
                    end

                else

%                     disp('normal')
                    tw = t(i) - tlag_n;
                    [~,ilag] = min(abs( t(1:i) - tw ));
                    Xm_lag = Z(ilag,1);
                end

            else
%                     disp('normal')
                tw = t(i) - tlag_n;
                [~,ilag] = min(abs( t(1:i) - tw ));
                Xm_lag = Z(ilag,1);
            end

            if(smooth_lag==1)
                ilag = ilag + (-2:2);
                ilag = ilag(ilag>0);
                ilag = ilag(ilag<=size(Z(isfinite(Z(:, 1)), :),1));
                Xm_lag = mean(Z(ilag,1));
            else
                Xm_lag = Z(ilag,1);
            end

            Xm_lag_old = Xm_lag;
            Xm_lag_vec(n,1) = Xm_lag;
```

```
            mixterr(i) = abs(Xm_lag_old / Xm_lag - 1);

            if( (abs(Xm_lag_old / Xm_lag - 1) < 1e-3 ))
                break
            end

            end
            ilag = round(mean(ilag));

    otherwise
            smooth_lag=0;
            mixt(i) = lag_yrs; %years
end

        % save lag values to output vector s
        if(smooth_lag==1)
            Xm_lagvec(i) = Xm_lag;
        else
            Xm_lagvec(i) = Z(ilag,1);
        end
        tlag_out(i) = t(ilag);

        %% Calculate Values for Next Timestep (RK4 Solver)
        % Solver uses Xm_lag to calculate how the water content (and
        % temperature) evolve over time

        % Calculate time derivatives of Y at i
        [dX1] = derivatives_solver(t(i),Z(i,:),Xm_lag);

        % First Estimate k1
        k1 = h .* dX1;
        t(i+1) = t(i) + h;

        % Calculate time derivatives of Y at midpoint t(i) + h./2 and Y(i) + k1/2
        t_new = t(i) + (h/2);
        Z_new = Z(i,:) + (k1'./2);
        [dX2] = derivatives_solver(t_new,Z_new,Xm_lag);

        % Second Estimate k2
        k2 = h .* dX2;

        % Calculate time derivatives of Y at midpoint t(i) + h./2 and Y(i) + k2/2
        t_new = t(i) + (h/2);
        Z_new = Z(i,:) + (k2'./2);
        [dX3] = derivatives_solver(t_new,Z_new,Xm_lag);
        % Third Estimate k3
        k3 = h .* dX3;

        % Calculate time derivatives of Y at t(i) + h and Y(i) + k3
        t_new = t(i) + (h);
        Z_new = Z(i,:) + (k3');
        [dX4] = derivatives_solver(t_new,Z_new,Xm_lag);
        % Fourth Estimate k4
        k4 = h .* dX4;

        % Calculate Y(i+1)
        Z(i+1,:) = Z(i,:) + (k1'./6) + (k2'./3) + (k3'./3) + (k4'./6);

        % Don't let Xm go negative
        switch etalawin
            case { 100, 121, 123, 1201, 1203 }
                Z(i+1,1) = max(Z(i+1,1),1);
                Z(i+1,3) = Z(1,3) - ((-Z(1,1)+Z(i,1)).* 9.05e20*rho/(1.39e21*1e6));%Z(ilag,3)
                    ;

            otherwise
                Z(i+1,1) = max(Z(i+1,1),0); % makes sure mantle water content doesn't go
                    negative
                Z(i+1,3) = max(Z(i+1,3),0); % makes sure ocean mass doesn't go negative
                Z(i+1,3) = min(Z(i+1,3),(Z(1,1)*rho*V/(1e6*M_oc)) + Z(1,3)); % makes sure
                    ocean mass doesn't increase above total water content of the system

        end

end
```

A.5 dynamics_solver_paper_maths.m

Calculates dynamic quantities H, Q_s, D and R for derivatives_solver.m or

SOLVER_vart2_wetstart.m.

```
%% Solves for dynamics

function [eta,Ra,U,dl,zm,dM_dt,Fd,R,D,Qs,H,Fr] = ...
    dynamics_solver_paper_maths(t,Xm,T,lawin,etain,Fr,Fd,Hsf,beta)

    % parameters
    par_solver;

    % for power law water dependence, stops water content going to zero
    switch lawin
        case {121,123,100,2350,2351,2353}
                Xm=max(Xm,1);
        otherwise
    end

    % viscosity
    eta = eta_calc(Xm,T,lawin,etain,E);

    % Rayleigh number
    Ra = (alpha_ra.*rho.*g.*T.*d^3)./(k.*eta);

    % plate velocity
    U = (k/d).*((L/(pi*d))^(1/3)).*Ra.^(beta);

    % lithospheric plate thickness
    dl = 2.32*(k.*L./U).^(1/2);

    % melting depth
    Tp_K = T.* exp(-alpha_ra*g*1445e3/Cp); %K potential T calculated from McKenzie and Bickle
        (1988)
    Tp_C = Tp_K - 273;                      %C
    zm = (z1.*(Tp_C)) + (z2.*Xm) + (z3);    %m
    zm = max(0,min(zm,300e3));              %m

    % mass flux
    dM_dt=S.*U.*(dl./L)*rho; %m^2 * ms^-1 * kgm^-3 = kgs^-1

    % water flux
    R = S.*Fr.*(dl./L).*U.*rho.*Xp ;  %ppm.kg/s
    D = S.*Fd.*(zm./L).*U.*rho.*Xm ;  %ppm.kg/s

    % surface heat flow
    Qs = 2*S*Kc.*T.*(U./(pi*L*k)).^(1/2); %W

    % internal heating
    H_El(:,1) = h_El(1,1).*h_El(2,1).*exp((log(2).*(t_pd-t))./h_El(3,1));
    H_El(:,2) = h_El(1,2).*h_El(2,2).*exp((log(2).*(t_pd-t))./h_El(3,2));
    H_El(:,3) = h_El(1,3).*h_El(2,3).*exp((log(2).*(t_pd-t))./h_El(3,3));
    H_El(:,4) = h_El(1,4).*h_El(2,4).*exp((log(2).*(t_pd-t))./h_El(3,4));
    H  = Hsf .* rho .* V .* sum(H_El,2); %W %2 in sum() sums along each row not column

end
```

A.6 relstrno.m

Post-processing step calculates relative strength number (S_{wt}) from Crowley et al. (2011).

```
% function for calculating the relative strength number Swt
% to determine the dominant influence on the viscosity

function [etaT,etaXm,Swt] = relstrno(T,Xm,eta,R,D,Qs,H,etalawin)

par_solver;

switch etalawin

    case {121 2351}
        etaT = -(E./(Rg.*T.*T)).*eta;
        etaXm = -0.3*Xm.^-1.*eta;

    case {123 2353}
        etaT = -(E./(Rg.*T.*T)).*eta;
        etaXm = -1*Xm.^-1.*eta;

    otherwise
        disp('no Swt available')
        etaT=0; etaXm=0;
end

SwtXm = etaXm.*(R-D);
SwtT = etaT.*(H-Qs)./Cp;

Swt = abs(SwtXm./SwtT);

end
```

A.7 eta_calc.m

Calculates viscosity given T, X and E.

```
%% eta_calc.m

% calculates viscosity from given average mantle temperature and average
% mantle water content

% etalawin defines a viscosity law by case
% eta0in is the calibration viscosity (Pas)

% Kiran Chotalia 7th Nov 2019

%%
function eta = eta_calc(Xm,T,etalawin,eta0in, E)

Rg = 8.314; % ideal gas constant (J/mol.K)

switch etalawin

% ********************  1e23 0ppm Calibration *********************
% Viscosity laws representative of experimental data (Fei et al., 2013, Nature)

    case 100 % no water influence
        eta = eta0in .* exp(E./(Rg.*T));
    case 121 % power law O(1)
        eta = eta0in .* (Xm./1).^-0.3 .* exp(E./(Rg.*T));
    case 123 % power law O(3)
        eta = eta0in .* (Xm./1).^-1.0 .* exp(E./(Rg.*T));

% ********************  1e23 500ppm Calibration *********************
% Viscosity laws representative of model implementation (e.g. )

    case 2350
        eta = eta0in .* exp(E./(Rg.*T));
    case 2351
        eta = 7.53e15 .* (Xm./500).^-0.3 .* exp(E./(Rg.*T));
    case 2353
        eta = 7.53e15 .* (Xm./500).^-1 .* exp(E./(Rg.*T));

    otherwise
        error(['Unknown etalaw: ' etalawin])

end
```

A.8 par_solver.m

File for constant parameters.

```
%% par_solver.m
% constant parameters

yr_s=365.25*24*60*60; %s in a year
t_pd = 4.6e9*yr_s;

% Water Content
M_oc = 1.39e21; % surface ocean mass
Xp = 2.056e3; % average water content of subducting package

% Planet Size
r_p = 6371e3; %m radius of planet
d = 2880e3;      %m depth of mantle
r_c = r_p-d; %m^3 radius of planet core
V = (4*pi/3)*(r_p^3-r_c^3);   %m^3 mantle volume

% Viscosity - Mei and Kohlstedt (2000a,b)
E = 300e3;       %J/mol activation energy
Rg = 8.314;       %J/mol.K ideal gas constant

% Rayleigh Number
alpha_ra = 2.5e-5; %1/K thermal expansion coefficient
g = 10;        %m/s^2 gravitational acceleration
rho = 3500;      %kg/m^3 density

% Plate Velocity
L = 2*d; %m average plate length/ average convection cell length

% Depth of Melting - Hirschmann et al. (2009)
% constants
z1 = 286;     %m/K
z2 = 164;     %m/ppm
z3 = -3.266e5;    %m

% Qs - Total Surface Heatflow
S = 0.71*4*pi*r_p^2; %m^2 planet surface area
Kc = 3;     %W/m.K thermal conductivity
Cp = 1000;  %J/kg.K specific heat
k = Kc/(Cp*rho);      %m2/s thermal diffusivity

% Element vectors containing concentration (kg/kg), heating rate (W/kg) and
% half life (s) respectively
%        C            H            tau
h1 = [30.8e-9;   9.46e-5;     4.47e9*yr_s      ]; %U238
h2 = [0.22e-9;   5.69e-4;     0.704e9*yr_s     ];  %U235
h3 = [124e-9;    2.64e-5;     14e9*yr_s        ];     %Th
h4 = [36.9e-9;   2.92e-5;     1.25e9*yr_s      ]; %K
h_El = [h1,h2,h3,h4];
```

B Ocean Mass - Sea Level Code

Generates dataset for ocean mass sea level relationship (Section 2.4).

```
%% Korenaga et al., (2017) Variable Ocean Mass/Volume
% Philosphical Transactions, Royal Society

% Calculaute the volume of an ocean from a calculated hypsometry
% curve following this paper's procedure

% Varying the ocean mass and trying to find teh corresponding sea
% level. Test different sea levels and see what the ocean volume is

% 22nd April 2019
% Last updated 1st Mar 2020
% Kiran Chotalia

clear all; close all

%% Sea Levels

sea_level_array = linspace(1.5*6866,0,101);
sea_level_array = sea_level_array(1:end-1);
sea_level_pd = 6866;

Aex_big = NaN(2,2,length(sea_level_array));

%% HIPYSOMETRY
%% Present Day Continental Topography
for p=1:length(sea_level_array)
    % Constants
    x1 = 0.575; x2 = 0.657; x3 = 0.725;
    a1 = -18.18; a2 = 27.36; a3 = -2.127; a4 = 2.932; a5 = -2.642; a6 = 3.642; a7 = 4.5; a8 =
        52.03;

    % Variables
    x = [0:1e-3:1]; % cumulative fraction of surface area
    zc = NaN(size(x)); % height (km)

    % Continental topography is divided into three parts:
    for i=1:length(x)

        % (1) continental shelf
        if x(i)>=x1 && x(i)<x2
            zc(i) = a1 + (a2*x(i));

        % (2) continental slope
        elseif x(i)>=x2 && x(i)<x3
            zc(i) = a3 + (a4*x(i));

        % (3) subaerial crust
        elseif x(i)>=x3 && x(i)<1 % x3 <= x <= 1
            zc(i) = a5 + a6*x(i) + a7*exp(a8*(x(i)-1));

        end

    end

%     figure(1)
%     plot(x,zc,'k')
%     hold on
%     plot([0 1], [ 0 0 ])
```

```
%
%     xlabel('Cumalative Fraction of Surface Area')
%     ylabel('Height (km)')

    %% BATHYMETRY
    % Surface Area of Oceanic Crust
    G0 = 3.45; % km2/yr plate creation rate

    Ae = 510.1e6; % km2 surface area of Earth
    Ac0 = (1-0.575); % surface area of continetal crust today
    Ao0 = Ae*(1 - Ac0); % surface area of oceanic crust today

    % Area-Age Distribution of Sea Floor
    tau_max0 = 2*Ao0/G0; % yr maximum plate age
    tau0 = linspace(0, tau_max0, 1e3);
    dAo_dtau = G0.*(1-(tau0./tau_max0));

%     figure(2)
%     plot(tau0, dAo_dtau)
%     xlabel('Oceanic Crust Age (a)')
%     ylabel('dA_o/dt (km^2/yr)')

    % Integral under the line of area-age distribution
    cumulative_Ao0 = cumtrapz(tau0,dAo_dtau); % Ao_fin = max(tau0)*max(dAo_dt)/2;
    cumulative_Ao0_fraction = cumulative_Ao0./Ae;

    % Present Day Bathymetry
    % (0) bathymetric crust

    b0 = 323; %m/Ma^0.5
    do0 = 2654; %m depth of mid-ocean ridge today
    d0 = do0 + b0.*(tau0./1e6).^0.5;

%     figure(3)
%     hold on
%     plot(cumulative_Ao0_fraction, -d0/1e3)

    total_cumulative_area = [cumulative_Ao0_fraction,x];
    total_height = [-d0/1e3,zc];

    remove_nans = ~isnan(total_height);
    total_height = total_height(remove_nans);
    total_cumulative_area = total_cumulative_area(remove_nans);

%     figure(4)
%     plot([0 1], [0 0],'linewidth',4)
%     hold on
%     plot(total_cumulative_area,total_height,'k','linewidth',4)
%     xlabel('Cumulative Surface Area Fraction')
%     ylabel('Height (km)')

    %% OCEAN VOLUME: Trapezoid Method

    A = total_cumulative_area.*Ae.*(1e3).^2;
    z = total_height*1e3;

    % 'absolute' sea level i.e. sea level NOT zero, lowest point in hypsometry is zero
    sea_level_m = [0 max(A); sea_level_array(p) sea_level_array(p) ];

    % absolute hypsometry i.e. sea level NOT zero, lowest point in hypsometry is zero
    hypsometry_m = [A;z+abs(min(z))];

    % Find intersection between hypsometric curve and sea level
    %   This is to limit the integration to no more than sea level

    % intersection between the two curves gives the point where land is exposed

    Aex = InterX(sea_level_m, hypsometry_m);
    Aex_size = size(Aex);

    % save intersections to larger, 3D array for later analysis
    if Aex_size(1,2)<2
        Aex_big(:,1,p) = Aex;
    else
        Aex_big(:,:,p) = Aex;
```

```
    end

    % To work out the ocean volume, only want the integral between the sea
    % level and hypsometry under water
    Ao = hypsometry_m(1,:);
    ho = hypsometry_m(2,:);

    if Aex_size(2)>1
        Ao = Ao(Ao>Aex(1,1) & Ao<Aex(1,2));
        ho = ho(ho<Aex(2,1));

        % Check if Ao and ho are the same length
        Ao_size = size(Ao);
        ho_size = size(ho);

        if Ao_size(1,2)<ho_size(1,2)
            Ao(1,end+1) = 2.933e14;
        end

        % integrate between the limited hysometry and sea level
        V_oc = sum(trapz(Ao,ho)); % volume of oceanic crust below sea level
        V_oandb = (Aex(1,2)-Aex(1,1)) * Aex(2,1); % volume of ocean and basin

    else
        Ao = Ao(Ao<Aex(1,1));
        ho = ho(ho<Aex(2,1));

        % integrate between the new hysometry and sea level
        V_oc = sum(trapz(Ao,ho)); % volume of oceanic crust
        V_oandb = sea_level_m(2,1)*Aex(1,1); % volume of ocean and basin

    end

        Vo(p) = V_oandb - V_oc;
        % same as Korenaga et al., (2017) their value for half space cooling: 1.496e18
        % Too high i.e. 1.49e18 instead of 1.39e18

        % Calculate mass of ocean from volume of hypsometry
        M(p) = Vo(p) * 1000; %kg, rho = 1000 kg/m3
        Rp = 6371e3; d = 2880e3; Rc = Rp - d; V = 4*pi/3 * (Rp^3 - Rc^3);
        Mm = V .* 3500;
        M_ppm(p) = M(p)./Mm .* 1e6;

    %%%% Check
    figure(5)
    plot(sea_level_m(1,:),sea_level_m(2,:),'linewidth',4)
    hold on
    plot(hypsometry_m(1,:),hypsometry_m(2,:),'k','linewidth',4)
    scatter(Aex(1,:),Aex(2,:),100)
    xlabel('Surface Area (m^2)')
    ylabel('Height (m)')
    xlim([ 0 max(sea_level_m(1,:)) ])
    %%%%

end
%% Plot Ocean Mass vs. Sea Level
% Want to find a relationship between sea level and ocean mass

figure(6)
plot( M_ppm./439,(sea_level_array-6866)./1e3,'linewidth',4)
ylabel('Relative Sea Level (km)')
xlabel('Ocean Mass (ppm)')
```

C Further Mixing Tests

Mixing Time (Gyrs)	H_{sf}	
	constant mixing	variable mixing
0.4	1.711	1.722
0.6	1.715	1.706
0.8	1.708	1.724
1	1.737	1.724
1.5	1.760	1.724
2	1.704	1.724
2.5	1.667	1.737
3	1.602	1.741
3.5	1,475	1.752
4	1.281	1.763
4.5	1.202	1.782
5-9	1.706	1.796

Table C.1: H_{sf} values to constrain to $\sim$46 TW for $O(1)$ constant mixing and variable mixing.

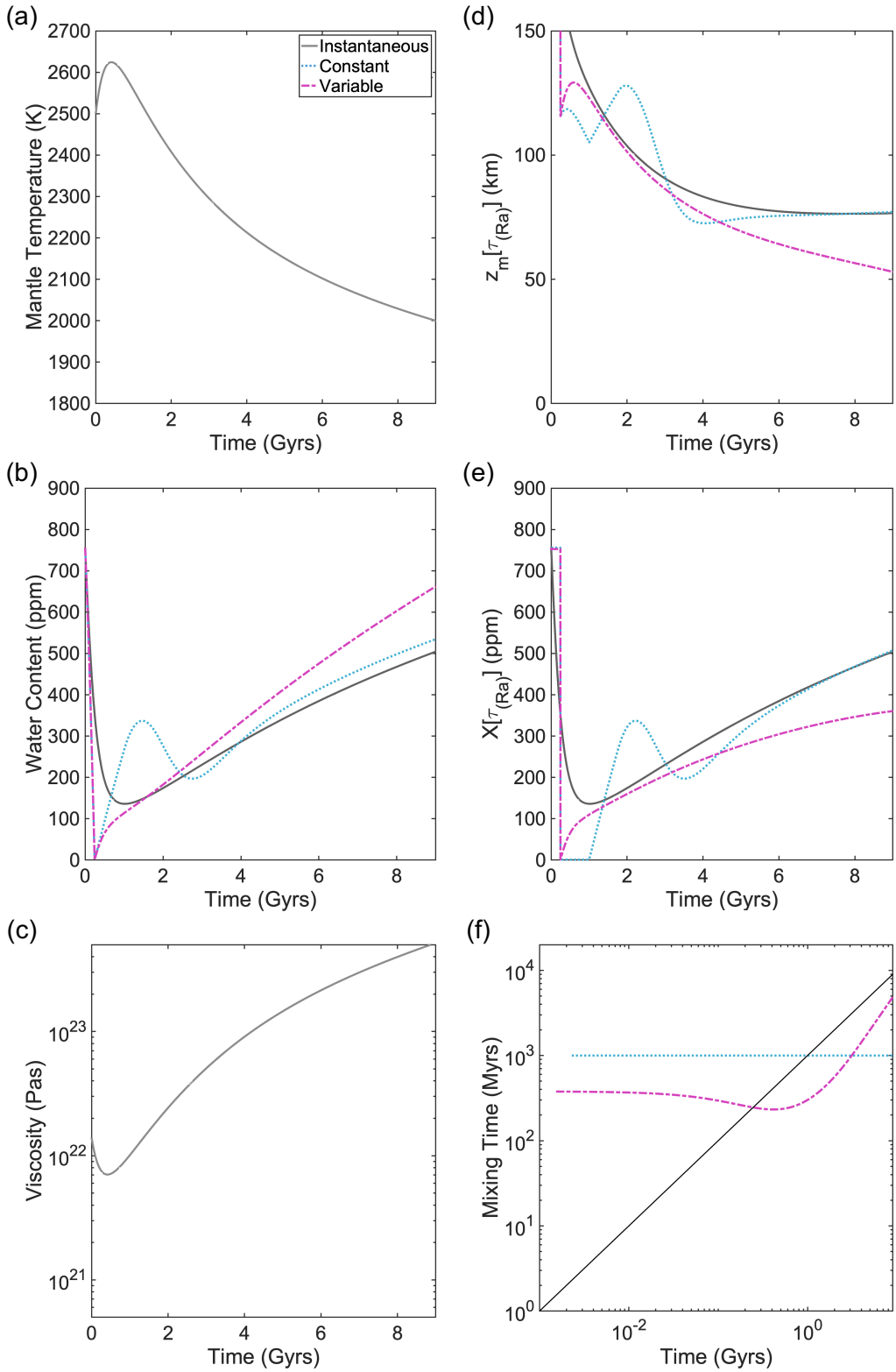

Figure C.1: The evolution of (a) temperature, (b) MOR water content, (c) viscosity, (d) melting depth, (e) MOR water content and (f) mixing time for $O(0)$ with mixing. The evolution begins with the MOR processing hydrous material with 895 ppm in the melt region i.e. the starting mantle water content. The high water content at the ridge promotes efficient degassing, such that the mantle is dried out rapidly. After this, the system operates as in Section 4.3.2.

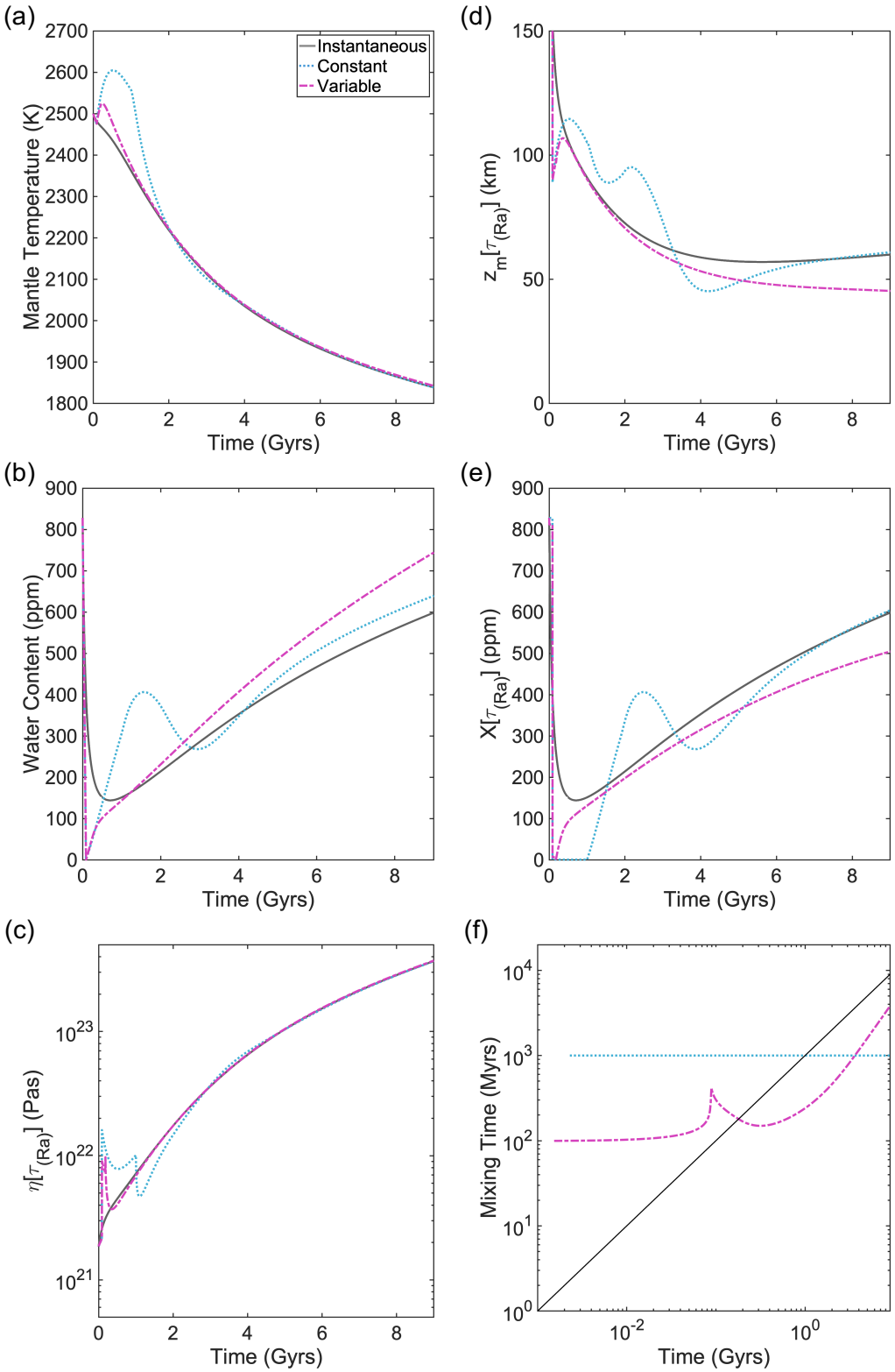

Figure C.2: The evolution of (a) temperature, (b) MOR water content, (c) viscosity, (d) melting depth, (e) MOR water content and (f) mixing time for $O(1)$ with mixing. As in Figure C.1, there is a period of rapid degassing before the evolution proceeds. With $O(1)$, there is also a feedback to the temperature evolution similar to results starting directly with a dry mantle.

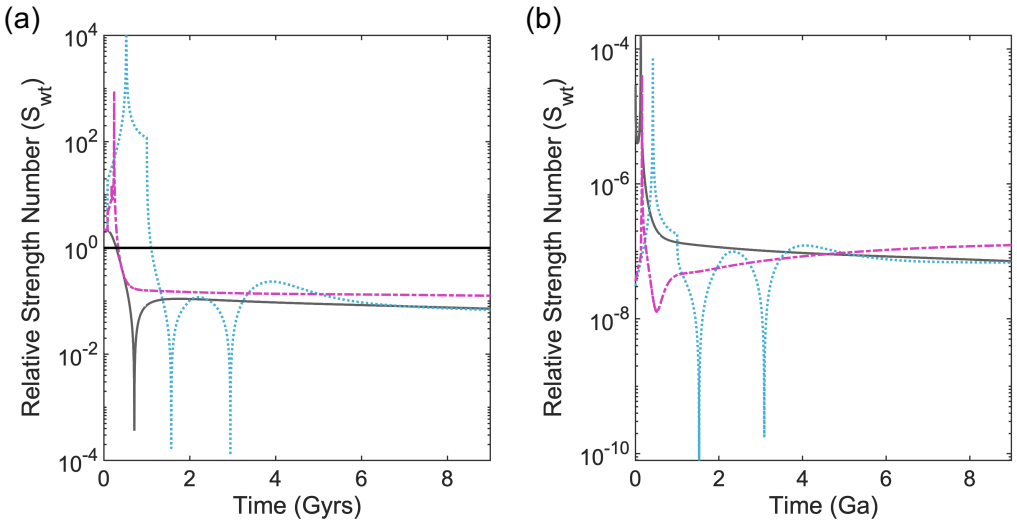

Figure C.3: S_{wt} calculated with the scheme in (a) Crowley et al. (2011) and (b) Nakagawa and Nakakuki (2019) for cases shown in Figure 4.3. Both ways of calculating show the same evolution. Crowley et al. (2011) calculate S_{wt} with $R - D$ in kg/yr whereas Nakagawa and Nakakuki (2019) calculate $R - D$ in kg/s. This causes a shift in the axes by ~10^7 i.e. how many seconds there are in one year. The peak corresponds to $H = Q_s$and $S_{wt} = \infty$ indicating a transition in the temperature evolution from heating to cooling. Troughs correspond to when $R = D$ and $S_{wt} = 0$ and indicate a switch from net regassing to net degassing, or vice versa. The two troughs correspond to the start and end of net degassing. For both, the evolution spends the majority of (if not all) it's time with temperature as the main control. (a) The first part in the evolution when $t < \tau_{(Ra)}$ is controlled by the water cycle where $S_{wt} > 1$. When $t > \tau_{(Ra)}$, $S_{wt} < 1$ and temperature is the main control on the system. In contrast, (b) is shifted downwards into the region where temperature is the main control on the evolution as S_{wt} is always much less than zero. This suggests that the system is primarily controlled by the temperature evolution.

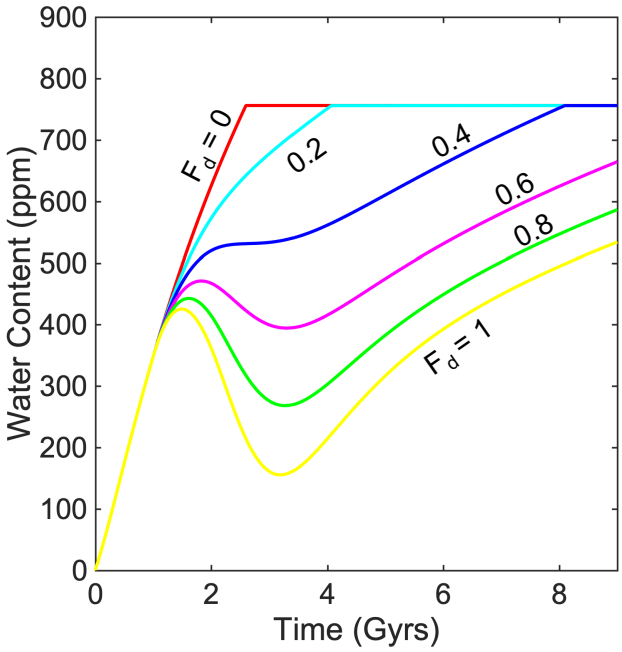

Figure C.4: Degassing efficiency also effects the net degassing period. As F_d decreases, the amplitude of net degassing reduces until $F_d < 0.4$, where net degassing no longer occurs, with timings changing little.

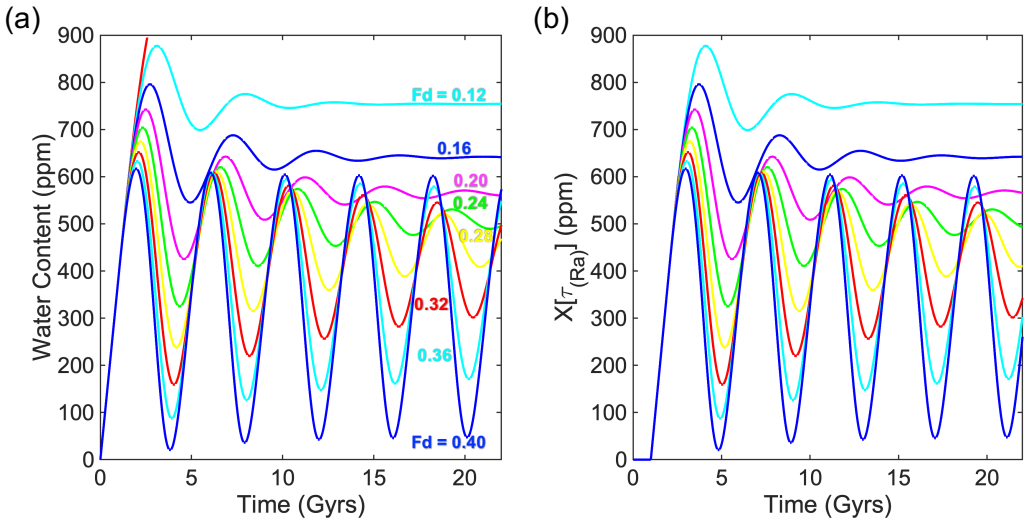

Figure C.5: Cases were run for $0.12 < F_d < 0.4$ but unlike the tests presented in Figure C.4, only evolution in the water cycle is solved. Temperature is constant throughout at 2200K, and hence plate velocity and and surface heat flow are also constant, 40 cm/yr and 135 TW. Oscillations are evident suggesting that the reason we only see one period of net degassing in Chapter 4 is due to the negative feedback, damping effect of a cooling system. As with Figure C.4, higher values of Fd result in more extreme degassing, however it also results in more periods of net degassing.

D Further Initial Water Tests

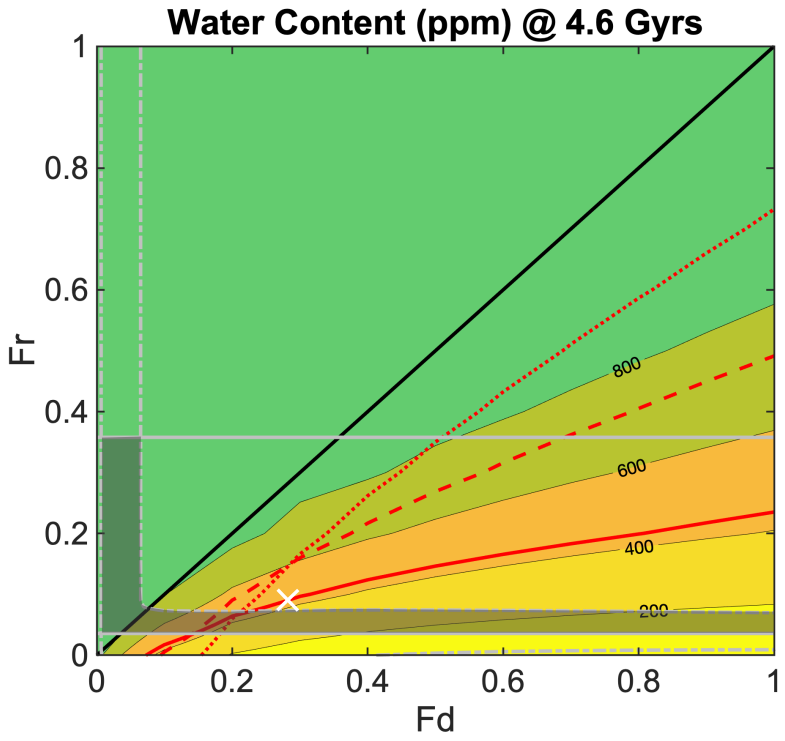

Figure D.1: F_d and F_r parameter search for 2 oceans starting in the mantle.

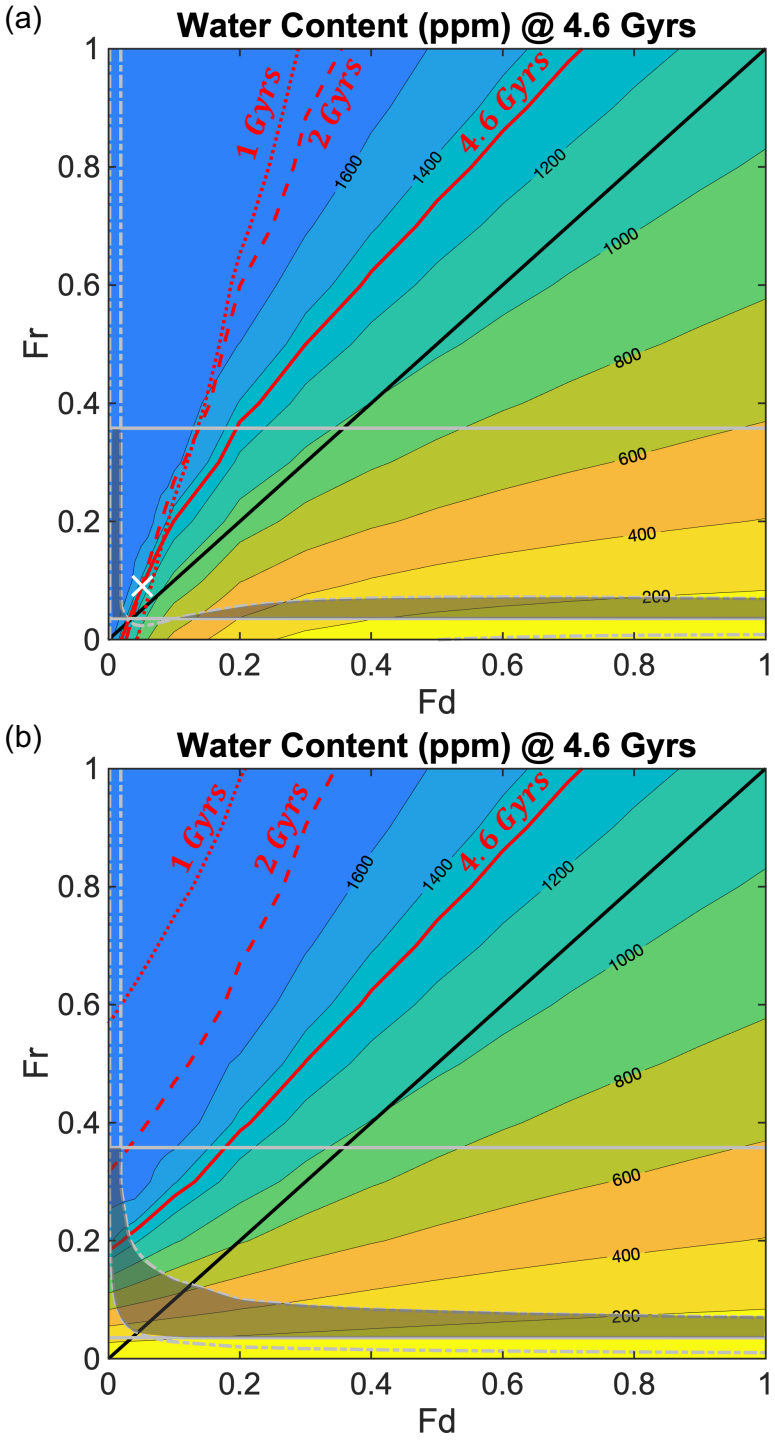

Figure D.2: F_d and F_r parameter search for 4 oceans in total beginning (a) in the mantle and (b) at the surface.

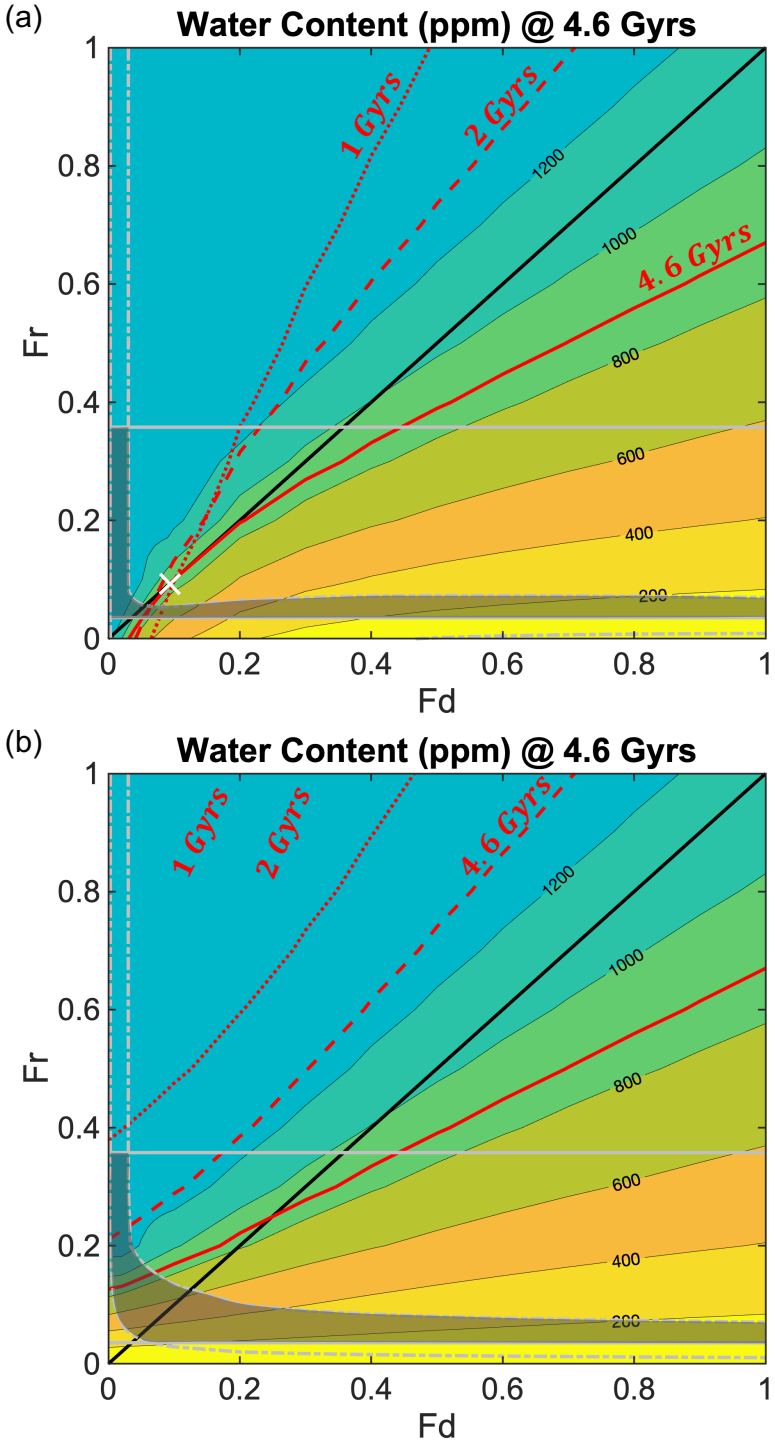

Figure D.3: F_d and F_r parameter search for 3 oceans in total beginning (a) in the mantle and (b) at the surface.

Bibliography

Amante, C., Eakins, B. W., 2009. ETOPO1 1 Arc-Minute Global Relief Model: Procedures, Data Sources and Analysis. NOAA Technical Memorandum NESDIS NGDC-24, 1–19.

Ammann, M., Brodholt, J., Dobson, D., 2010. Simulating Diffusion. Reviews in Mineralogy and Geochemistry 71 (1), 201–224.

Asimow, P. D., Dixon, J. E., Langmuir, C. H., 2004. A hydrous melting and fractionation model for mid-ocean ridge basalts: Application to the Mid-Atlantic Ridge near the Azores. Geochemistry, Geophysics, Geosystems 5 (1), 1–24.

Bell, D. R., Rossman, G. R., Maldener, J., Endisch, D., Rauch, F., 2003. Hydroxide in olivine: A quantitative determination of the absolute amount and calibration of the IR spectrum. Journal of Geophysical Research: Solid Earth 108 (B2).

Bindeman, I. N., Zakharov, D. O., Palandri, J., Greber, N. D., Dauphas, N., Retallack, G. J., Hofmann, A., Lackey, J. S., Bekker, A., 2018. Rapid emergence of subaerial landmasses and onset of a modern hydrologic cycle 2.5 billion years ago. Nature 557 (7706), 545–548.

Bolfan-Casanova, N., Keppler, H., Rubie, D. C., 2000. Water partitioning between nominally anhydrous minerals in the MgO-SiO2-H2O system up to 24 GPa: Implications for the distribution of water in the Earth's mantle. Earth and Planetary Science Letters 182 (3-4), 209–221.

Breuer, D., 2011. Primordial Heat. In: Encyclopedia of Astrobiology. Springer Berlin Heidelberg, Berlin, Heidelberg, pp. 1333–1333.

Buchen, J., Marquardt, H., Speziale, S., Kawazoe, T., Boffa Ballaran, T., Kurnosov, A., 2018. High-pressure single-crystal elasticity of wadsleyite and the seismic signature of water in the shallow transition zone. Earth and Planetary Science Letters 498, 77–87.

Callender, A., Hartree, D. R., Porter, A., 1936. Time-Lag in a Control System. Philosophical Transactions of the Royal Society A: Mathematical, Physical and Engineering Sciences 235 (756), 415–444.

Chopra, P. N., Paterson, M. S., 1984. The role of water in the deformation of dunite. Journal of Geophysical Research 89 (B9), 7861–7876.

Christensen, U. R., 1985. Thermal evolution models for the Earth. Journal of Geophysical Research: Solid Earth 90 (5), 2995–3007.

Cogné, J.-P., Humler, E., 2004. Temporal variation of oceanic spreading and crustal production rates during the last 180 My. Earth and Planetary Science Letters 227 (3-4), 427–439.

Condie, K. C., Aster, R. C., van Hunen, J., 2016. A great thermal divergence in the mantle beginning 2.5 Ga: Geochemical constraints from greenstone basalts and komatiites. Geoscience Frontiers 7 (4), 543–553.

Crowley, J. W., Gérault, M., O'Connell, R. J., 2011. On the relative influence of heat and water transport on planetary dynamics. Earth and Planetary Science Letters 310 (3-4), 380–388.

Daly, R. T., Schultz, P. H., 2018. The delivery of water by impacts from planetary accretion to present. Science Advances 4 (4), eaar2632.

Davies, G. F., 1998. Plates, Plumes, Mantle Convection, and Mantle Evolution. Cambridge University Press.

Davis, E., Lister, C., 1974. Fundamentals of ridge crest topography. Earth and Planetary Science Letters 21 (4), 405–413.

DiMarco, M. J., Lowe, D. R., 1989. Shallow-water volcaniclastic deposition in the Early Archean Panorama Formation, Warrawoona Group, eastern Pilbara Block, Western Australia. Sedimentary Geology 64 (1-3), 43–63.

Dixon, J. E., Stolper, E. M., 1995. An Experimental Study of Water and Carbon Dioxide Solubilities in Mid-Ocean Ridge Basaltic Liquids. Part II: Applications to Degassing. Journal of Petrology 36 (6), 1633–1646.

Doyne Farmer, J., 1982. Chaotic attractors of an infinite-dimensional dynamical system. Physica D: Nonlinear Phenomena 4 (3), 366–393.

Dziewonski, A. M., Anderson, D. L., 1981. Preliminary reference Earth model. Physics of the Earth and Planetary Interiors 25 (4), 297–356.

Elkins-Tanton, L. T., 2011. Formation of early water oceans on rocky planets. Astrophysics and Space Science 332 (2), 359–364.

Faccenda, M., 2014. Water in the slab: A trilogy. Tectonophysics 614, 1–30.

Fei, H., Wiedenbeck, M., Yamazaki, D., Katsura, T., 2013. Small effect of water on upper-mantle rheology based on silicon self-diffusion coefficients. Nature 498 (7453), 213–215.

Fei, H., Yamazaki, D., Sakurai, M., Miyajima, N., Ohfuji, H., Katsura, T., Yamamoto, T., 2017. A nearly water-saturated mantle transition zone inferred from mineral viscosity. Science Advances 3 (6), e1603024.

Flament, N., Coltice, N., Rey, P. F., 2008. A case for late-Archaean continental emergence from thermal evolution models and hypsometry. Earth and Planetary Science Letters 275 (3-4), 326–336.

Flament, N., Rey, P. F., Coltice, N., Dromart, G., Olivier, N., 2011. Lower crustal flow kept Archean continental flood basalts at sea level. Geology 39 (12), 1159–1162.

Franck, S., Bounama, C., 1995. Effects of water-dependent creep rate on the volatile exchange between mantle and surface reservoirs. Physics of the Earth and Planetary Interiors 92 (1-2), 57–65.

Franck, S., Bounama, C., 2001. Global water cycle and Earth's thermal evolution. Journal of Geodynamics 32 (1-2), 231–246.

Goes, S., Agrusta, R., van Hunen, J., Garel, F., 2017. Subduction-transition zone interaction: A review. Geosphere 13 (3), 644–664.

Gonnermann, H. M., Mukhopadhyay, S., 2009. Preserving noble gases in a convecting mantle. Nature 459 (7246), 560–563.

Gordon, R. G., Cox, A., Harter, C. E., 1978. Absolute motion of an individual plate estimated from its ridge and trench boundaries. Nature 274 (5673), 752–755.

Grove, T., Parman, S., 2004. Thermal evolution of the Earth as recorded by komatiites. Earth and Planetary Science Letters 219 (3-4), 173–187.

Gurnis, M., Davies, G. F., 1986. The effect of depth-dependent viscosity on convective mixing in the mantle and the possible survival of primitive mantle. Geophysical Research Letters 13 (6), 541–544.

Hager, B. H., Clayton, R. W., Richards, M. A., Comer, R. P., Dziewonski, A. M., 1985. Lower mantle heterogeneity, dynamic topography and the geoid. Nature 313 (6003), 541–545.

Hallis, L. J., 2017. D/H ratios of the inner Solar System. Philosophical Transactions of the Royal Society A: Mathematical, Physical and Engineering Sciences 375 (2094), 20150390.

Hallis, L. J., Huss, G. R., Nagashima, K., Taylor, G. J., Halldórsson, S. A., Hilton, D. R., Mottl, M. J., Meech, K. J., 2015. Evidence for primordial water in Earth's deep mantle. Science 350 (6262), 795–797.

Hartogh, P., Lis, D. C., Bockelée-Morvan, D., De Val-Borro, M., Biver, N., Küppers, M., Emprechtinger, M., Bergin, E. A., Crovisier, J., Rengel, M., Moreno, R., Szutowicz, S., Blake, G. A., 2011. Ocean-like water in the Jupiter-family comet 103P/Hartley 2. Nature 478 (7368), 218–220.

Hernández, E., Alfè, D., Brodholt, J., 2013. The incorporation of water into lower-mantle perovskites: A first-principles study. Earth and Planetary Science Letters 364, 37–43.

Hilairet, N., Reynard, B., 2009. Stability and dynamics of serpentinite layer in subduction zone. Tectonophysics 465 (1-4), 24–29.

Hirschmann, M., Kohlstedt, D., 2012. Water in Earth's mantle. Physics Today 65 (3), 40–45.

Hirschmann, M. M., 2000. Mantle solidus: Experimental constraints and the effects of peridotite composition. Geochemistry, Geophysics, Geosystems 1 (10).

Hirschmann, M. M., 2006. Water, melting, and the deep earth H2O cycle. Annual Review of Earth and Planetary Sciences 34 (1), 629–653.

Hirschmann, M. M., Tenner, T., Aubaud, C., Withers, A. C., 2009. Dehydration melting of nominally anhydrous mantle: The primacy of partitioning. Physics of the Earth and Planetary Interiors 176 (1-2), 54–68.

Höning, D., Hansen-Goos, H., Airo, A., Spohn, T., 2014. Biotic vs. abiotic Earth: A model for mantle hydration and continental coverage. Planetary and Space Science 98, 5–13.

Höning, D., Spohn, T., 2016. Continental growth and mantle hydration as intertwined feedback cycles in the thermal evolution of Earth. Physics of the Earth and Planetary Interiors 255, 27–49.

Houser, C., 2016. Global seismic data reveal little water in the mantle transition zone. Earth and Planetary Science Letters 448, 94–101.

Hsieh, W. P., Deschamps, F., Okuchi, T., Lin, J. F., 2017. Reduced lattice thermal conductivity of Fe-bearing bridgmanite in Earth's deep mantle. Journal of Geophysical Research: Solid Earth 122 (7), 4900–4917.

Ida, S., Yamamura, T., Okuzumi, S., 2019. Water delivery by pebble accretion to rocky planets in habitable zones in evolving disks. Astronomy & Astrophysics 624, A28.

Iwamori, H., 2004. Phase relations of peridotites under H2O-saturated conditions and ability of subducting plates for transportation of H2O. Earth and Planetary Science Letters 227 (1-2), 57–71.

Jackson, M. J., Pollack, H. N., 1987. Mantle devolatilization and convection: Implications for the thermal history of the Earth. Geophysical Research Letters 14 (7), 737–740.

Jaupart, C., Labrosse, S., Lucazeau, F., Mareschal, J. C., 2015. Temperatures, Heat, and Energy in the Mantle of the Earth. Vol. 7. Elsevier B.V.

Jung, H., Karato, S.-I., 2001. Water-Induced Fabric Transitions in Olivine. Science 293 (5534), 1460–1463.

Junges, L., Gallas, J. A., 2012. Intricate routes to chaos in the MackeyâGlass delayed feedback system. Physics Letters A 376 (30-31), 2109–2116.

Karato, S.-i., 2010. Rheology of the deep upper mantle and its implications for the preservation of the continental roots: A review. Tectonophysics 481 (1-4), 82–98.

Karato, S.-I., Paterson, M. S., FitzGerald, J. D., 1986. Rheology of synthetic olivine aggregates: Influence of grain size and water. Journal of Geophysical Research 91 (B8), 8151.

Karato, S.-i., Wu, P., 1993. Rheology of the Upper Mantle: A Synthesis. Science 260 (5109), 771–778.

Karlsen, K. S., Conrad, C. P., Magni, V., 2019. Deep Water Cycling and Sea Level Change Since the Breakup of Pangea. Geochemistry, Geophysics, Geosystems, 2019GC008232.

Kellogg, L. H., Stewart, C. a., 1991. Mixing by chaotic convection in an infinite Prandtl number fluid and implications for mantle convection. Physics of Fluids A: Fluid Dynamics 3 (5), 1374.

Kohlstedt, D. L., Keppler, H., Rubie, D. C., 1996. Solubility of water in the α, β and γ phases of (Mg,Fe)2SiO4. Contributions to Mineralogy and Petrology 123 (4), 345–357.

Komacek, T. D., Abbot, D. S., 2016. Effect of Surface-Mantle Water Exchange Parameterizations on Exoplanet Ocean Depths. The Astrophysical Journal 832 (1), 54.

Korenaga, J., 2011. Thermal evolution with a hydrating mantle and the initiation of plate tectonics in the early Earth. Journal of Geophysical Research 116 (B12), B12403.

Korenaga, J., Planavsky, N. J., Evans, D. A. D., 2017. Global water cycle and the coevolution of the Earth's interior and surface environment. Philosophical Transactions of the Royal Society A: Mathematical, Physical and Engineering Sciences 375 (2094), 20150393.

Labrosse, S., Hernlund, J. W., Coltice, N., 2007. A crystallizing dense magma ocean at the base of the Earth's mantle. Nature 450 (7171), 866–869.

Larson, K. M., Freymueller, J. T., Philipsen, S., 1997. Global plate velocities from the Global Positioning System. Journal of Geophysical Research: Solid Earth 102 (B5), 9961–9981.

Lay, T., Hernlund, J., Buffett, B. A., 2008. Coreâmantle boundary heat flow. Nature Geoscience 1 (1), 25–32.

Li, Z. X. A., Lee, C. T. A., Peslier, A. H., Lenardic, A., Mackwell, S. J., 2008. Water contents in mantle xenoliths from the Colorado Plateau and vicinity: Implications for the mantle rheology and hydration-induced thinning of continental lithosphere. Journal of Geophysical Research: Solid Earth 113 (9).

Litasov, K., Ohtani, E., 2003. Stability of various hydrous phases in CMAS pyrolite-H2O system up to 25 GPa. Physics and Chemistry of Minerals 30 (3), 147–156.

Lourenço, D. L., Rozel, A. B., Gerya, T., Tackley, P. J., 2018. Efficient cooling of rocky planets by intrusive magmatism. Nature Geoscience 11 (5), 322–327.

Mackey, M., Glass, L., 1977. Oscillation and chaos in physiological control systems. Science 197 (4300), 287–289.

Magni, V., Bouilhol, P., van Hunen, J., 2014. Deep water recycling through time. Geochemistry Geophysics Geosystems 15, 4203–4216.

Manga, M., 1996. Mixing of heterogeneities in the mantle: Effect of viscosity differences. Geophysical Research Letters 23 (4), 403–406.

Mao, Z., Lin, J.-F., Jacobsen, S. D., Duffy, T. S., Chang, Y.-Y., Smyth, J. R., Frost, D. J., Hauri, E. H., Prakapenka, V. B., 2012. Sound velocities of hydrous ringwoodite to 16GPa and 673K. Earth and Planetary Science Letters 331-332, 112–119.

Marty, B., 2012a. The origins and concentrations of water, carbon, nitrogen and noble gases on Earth. Earth and Planetary Science Letters 313-314, 56–66.

Marty, B., 2012b. The origins and concentrations of water, carbon, nitrogen and noble gases on Earth. Earth and Planetary Science Letters 313-314 (1), 56–66.

Marty, B., Avice, G., Sano, Y., Altwegg, K., Balsiger, H., Hässig, M., Morbidelli, A., Mousis, O., Rubin, M., 2016. Origins of volatile elements (H, C, N, noble gases) on Earth and Mars in light of recent results from the ROSETTA cometary mission. Earth and Planetary Science Letters 441, 91–102.

May, R. M., 1980. NONLINEAR PHENOMENA IN ECOLOGY AND EPIDEMIOLOGY*. Annals of the New York Academy of Sciences 357 (1), 267–281.

McGovern, P. J., Schubert, G., 1989. Thermal evolution of the Earth: effects of volatile exchange between atmosphere and interior. Earth and Planetary Science Letters 96 (1-2), 27–37.

Mckenzie, D., Bickle, M. J., 1988. The volume and composition of melt generated by extension of the lithosphere. Journal of Petrology 29 (3), 625–679.

Mei, S., Kohlstedt, D. L., 2000a. Influence of water on plastic deformation of olivine aggregates: 1. Diffusion creep regime. Journal of Geophysical Research 105, 21457.

Mei, S., Kohlstedt, D. L., 2000b. Influence of water on plastic deformation of olivine aggregates: 2. Dislocation creep regime. Journal of Geophysical Research 105 (B9), 21471.

Mitrovica, J., Forte, A., 2004. A new inference of mantle viscosity based upon joint inversion of convection and glacial isostatic adjustment data. Earth and Planetary Science Letters 225 (1-2), 177–189.

Moore, W. B., Webb, A. A. G., 2013. Heat-pipe earth. Nature 501 (7468), 501–505.

Muir, J. M., Brodholt, J. P., 2018. Water distribution in the lower mantle: Implications for hydrolytic weakening. Earth and Planetary Science Letters 484, 363–369.

Murakami, M., Hirose, K., Yurimoto, H., Nakashima, S., Takafuji, N., 2002. Water in Earth's lower mantle. Science 295 (5561), 1885–1887.

Nakagawa, T., 2017. On the numerical modeling of the deep mantle water cycle in global-scale mantle dynamics: The effects of the water solubility limit of lower mantle minerals. Journal of Earth Science 28 (4), 1–15.

Nakagawa, T., Iwamori, H., 2017. Long-Term Stability of Plate-Like Behavior Caused by Hydrous Mantle Convection and Water Absorption in the Deep Mantle. Journal of Geophysical Research: Solid Earth, 1–15.

Nakagawa, T., Nakakuki, T., 2019. Dynamics in the Uppermost Lower Mantle: Insights into the Deep Mantle Water Cycle Based on the Numerical Modeling of Subducted Slabs and Global-Scale Mantle Dynamics. Annual Review of Earth and Planetary Sciences 47 (1), 41–66.

Nakagawa, T., Nakakuki, T., Iwamori, H., 2015. Water circulation and global mantle dynamics: Insight from numerical modeling. Geochemistry, Geophysics, Geosystems 16 (5), 1449–1464.

Nakagawa, T., Spiegelman, M. W., 2017. Global-scale water circulation in the Earth's mantle: Implications for the mantle water budget in the early Earth. Earth and Planetary Science Letters 464, 189–199.

Nakao, A., Iwamori, H., Nakakuki, T., 2016. Effects of water transportation on subduction dynamics: Roles of viscosity and density reduction. Earth and Planetary Science Letters 454, 178–191.

Nestola, F., Smyth, J. R., 2015. Diamonds and water in the deep Earth: a new scenario. International Geology Review 6814 (June), 1–14.

Niculescu, S.-I., Verriest, E. I., Dugard, L., Dion, J.-M., 1998. Stability and robust stability of time-delay systems: A guided tour. In: Stability and Control of Time-delay Systems. Springer-Verlag, London, pp. 1–71.

Ohtani, E., 2005. Water in the Mantle. Elements 1, 22–30.

Ohtani, E., Mizobata, H., Yurimoto, H., 2000. Stability of dense hydrous magnesium silicate phases in the systems Mg2SiO4-H2O and MgSiO3-H2O at pressures up to 27 GPa. Physics and Chemistry of Minerals 27 (8), 533–544.

Okuda, Y., Ohta, K., Sinmyo, R., Hirose, K., Yagi, T., Ohishi, Y., 2019. Effect of spin transition of iron on the thermal conductivity of (Fe, Al)-bearing bridgmanite. Earth and Planetary Science Letters 520, 188–198.

Olson, P., Sharp, Z. D., 2018. Hydrogen and helium ingassing during terrestrial planet accretion. Earth and Planetary Science Letters 498, 418–426.

O'Neill, C., Debaille, V., Griffin, W., 2013. Deep earth recycling in the Hadean and constraints on surface tectonics. American Journal of Science 313 (9), 912–932.

Panero, W. R., Pigott, J. S., Reaman, D. M., Kabbes, J. E., Liu, Z., 2015. Dry (Mg,Fe)SiO 3 perovskite in the Earth's lower mantle. Journal of Geophysical Research: Solid Earth 120 (2), 894–908.

Parai, R., Mukhopadhyay, S., 2018. Xenon isotopic constraints on the history of volatile recycling into the mantle. Nature 560 (7717), 223–227.

Pearson, D. G., Brenker, F. E., Nestola, F., McNeill, J., Nasdala, L., Hutchison, M. T., Matveev, S., Mather, K., Silversmit, G., Schmitz, S., Vekemans, B., Vincze, L., 2014. Hydrous mantle transition zone indicated by ringwoodite included within diamond. Nature 507 (7491), 221–224.

Price, M. G., Davies, J. H., Panton, J., 2019. Controls on the Deep-Water Cycle Within Three-Dimensional Mantle Convection Models. Geochemistry, Geophysics, Geosystems, 2018GC008158.

Ringwood, A. E., 1962. A model for the upper mantle. Journal of Geophysical Research 67 (11), 4473–4478.

Rudolph, M. L., Lekic, V., Lithgow-Bertelloni, C., 2015. Viscosity jump in Earths mid-mantle. Science 350 (6266), 1349–1352.

Rupke, L., Morgan, J. P., Hort, M., Connolly, J. A. D., 2004. Serpentine and the subduction zone water cycle. Earth and Planetary Science Letters 223 (1-2), 17–34.

Rüpke, L., Phipps Morgan, J., Eaby Dixon, J., 2013. Implications of Subduction Rehydration for Earth's Deep Water Cycle. In: EOS, Transactions, American Geophysical Union. Vol. 87. pp. 263–276.

Samuel, H., Aleksandrov, V., Deo, B., 2011. The effect of continents on mantle convective stirring. Geophysical Research Letters 38 (4), 1–5.

Sandu, C., Lenardic, A., McGovern, P., 2011. The effects of deep water cycling on planetary thermal evolution. Journal of Geophysical Research: Solid Earth 116 (12), 1–16.

Schaefer, L., Sasselov, D., 2015. THE PERSISTENCE OF OCEANS ON EARTH-LIKE PLANETS: INSIGHTS FROM THE DEEP-WATER CYCLE. The Astrophysical Journal 801 (1), 40.

Schmidt, M. W., Poli, S., 1998. Experimentally based water budgets for dehydrating slabs and consequences for arc magma generation. Earth and Planetary Science Letters 163 (1-4), 361–379.

Schubert, G., Cassen, P., Young, R. E., 1979. Subsolidus convective cooling histories of terrestrial planets. Icarus 38 (2), 192–211.

Schubert, G., Stevenson, D., Cassen, P., 1980. Whole planet cooling and the radiogenic heat source contents of the Earth and Moon. Journal of Geophysical Research 85 (B5), 2531.

Schubert, G., Turcotte, D. L., Olson, P., 2001. Mantle Convection in the Earth and Planets. Cambridge University Press, Cambridge.

Sharpe, H. N., Peltier, W. R., 1978. Parameterized mantle convection and the Earth's thermal history. Geophysical Research Letters 5 (9), 737–740.

Sleep, N. H., Zahnle, K. J., Lupu, R. E., 2014. Terrestrial aftermath of the Moon-forming impact. Philosophical Transactions of the Royal Society A: Mathematical, Physical and Engineering Sciences 372 (2024), 20130172.

Smyth, J. R., Jacobsen, S. D., 2013. Nominally Anhydrous Minerals and Earth's Deep Water Cycle. In: Earth's Deep Water Cycle. pp. 1–11.

Solomatov, V., 2001. Grain size-dependent viscosity convection and the thermal evolution of the Earth. Earth and Planetary Science Letters 191 (3-4), 203–212.

Stixrude, L., Lithgow-Bertelloni, C., 2012. Geophysics of Chemical Heterogeneity in the Mantle. Annual Review of Earth and Planetary Sciences 40 (1), 569–595.

Tackley, P., 2015. Mantle Geochemical Geodynamics. In: Treatise on Geophysics. Vol. 7. Elsevier, pp. 521–585.

Tikoo, S. M., Elkins-Tanton, L. T., 2017. The fate of water within Earth and super-Earths and implications for plate tectonics. Philosophical Transactions of the Royal Society A: Mathematical, Physical and Engineering Sciences 375 (2094), 20150394.

Townsend, J. P., Tsuchiya, J., Bina, C. R., Jacobsen, S. D., 2015. First-principles investigation of hydrous post-perovskite. Physics of the Earth and Planetary Interiors 244, 42–48.

Tozer, D. C., 1965. Heat transfer and convection currents. Philosophical Transactions of the Royal Society of London. Series A, Mathematical and Physical Sciences 258 (1088), 252–271.

Trail, D., Boehnke, P., Savage, P. S., Liu, M.-C., Miller, M. L., Bindeman, I., 2018. Origin and significance of Si and O isotope heterogeneities in Phanerozoic, Archean, and Hadean zircon. Proceedings of the National Academy of Sciences 115 (41), 10287–10292.

Tschauner, O., Huang, S., Greenberg, E., Prakapenka, V. B., Rossman, G. R., Shen, A. H., Zhang, D., Newville, M., Lanzirotti, A., Tait, K., 2018. Ice-VII inclusions in diamonds: Evidence for aqueous fluid in Earth ' s deep mantle 1139 (March), 1136–1139.

Tucker, J. M., Mukhopadhyay, S., 2014. Evidence for multiple magma ocean outgassing and atmospheric loss episodes from mantle noble gases. Earth and Planetary Science Letters 393, 254–265.

Turcotte, D. L., Oxburgh, E. R., 1967. Finite amplitude convective cells and continental drift. Journal of Fluid Mechanics 28 (01), 29–42.

van Hunen, J., Moyen, J.-F., 2012. Archean Subduction: Fact or Fiction? Annual Review of Earth and Planetary Sciences 40 (1), 195–219.

van Keken, P. E., Hacker, B. R., Syracuse, E. M., Abers, G. A., 2011. Subduction factory: 4. Depth-dependent flux of H 2 O from subducting slabs worldwide. Journal of Geophysical Research 116 (B1), B01401.

Wang, Y., Hilairet, N., Nishiyama, N., Yahata, N., Tsuchiya, T., Morard, G., Fiquet, G., 2013. High-pressure, high-temperature deformation of CaGeO3 (perovskite) and MgO aggregates: Implications for multiphase rheology of the lower mantle. Geochemistry, Geophysics, Geosystems 14 (9), 3389–3408.

Wang, Y., Pavlis, G. L., Li, M., 2019. Heterogeneous distribution of water in the mantle transition zone inferred from wavefield imaging. Earth and Planetary Science Letters 505, 42–50.

Watson, C. S., White, N. J., Church, J. A., King, M. A., Burgette, R. J., Legresy, B., 2015. Unabated global mean sea-level rise over the satellite altimeter era. Nature Climate Change 5 (6), 565–568.

Williams, D. R., Pan, V., 1992. Internally heated mantle convection and the thermal and degassing history of the Earth. Journal of Geophysical Research 97 (B6), 8937.

Wise, D. U., 1974. Continental Margins, Freeboard and the Volumes of Continents and Oceans Through Time. In: The Geology of Continental Margins. Springer Berlin Heidelberg, Berlin, Heidelberg, pp. 45–58.

Wolf, A. S., Jackson, J. M., Dera, P., Prakapenka, V. B., 2015. The thermal equation of state of (Mg, Fe)SiO3 bridgmanite (perovskite) and implications for lower mantle structures. Journal of Geophysical Research: Solid Earth 120 (11), 7460–7489.

Xu, J., Yamazaki, D., Katsura, T., Wu, X., Remmert, P., Yurimoto, H., Chakraborty, S., 2011. Silicon and magnesium diffusion in a single crystal of MgSiO 3 perovskite. Journal of Geophysical Research 116 (B12), B12205.

Yang, J., Zhao, L., Kaus, B. J., Lu, G., Wang, K., Zhu, R., 2018. Slab-triggered wet upwellings produce large volumes of melt: Insights into the destruction of the North China Craton. Tectonophysics 746, 266–279.

Zerr, A., Diegeler, A., Boehler, R., 1998. Solidus of Earth's Deep Mantle. Science 281 (5374), 243–246.